FINITE ELEMENT MODELING OF CONCRETE STRUCTURES STRENGTHENED WITH FRP LAMINATES

Final Report

SPR 316

by

Damian Kachlakev, PhD
Civil and Environmental Engineering Department,
California Polytechnic State University, San Luis Obispo, CA 93407
and
Thomas Miller, PhD, PE; Solomon Yim, PhD, PE;
Kasidit Chansawat; Tanarat Potisuk
Civil, Construction and Environmental Engineering Department,
Oregon State University, Corvallis, OR 97331

for

Oregon Department of Transportation
Research Group
200 Hawthorne SE, Suite B-240
Salem, OR 97301-5192

and

Federal Highway Administration
400 Seventh Street SW
Washington, DC 20590

May 2001

Technical Report Documentation Page

1. Report No. FHWA-OR-RD-01-17	2. Government Accession No.	3. Recipient's Catalog No.

4. Title and Subtitle

Finite Element Modeling of Concrete Structures Strengthened with FRP Laminates – Final Report

5. Report Date

May 2001

6. Performing Organization Code

7. Author(s)

Damian Kachlakev, PhD, Civil and Environmental Engineering Department,
California Polytechnic State University, San Luis Obispo, CA 93407
and
Thomas Miller, PhD, PE; Solomon Yim, PhD, PE; Kasidit Chansawat; Tanarat Potisuk, Civil, Construction and Environmental Engineering Department,
Oregon State University, Corvallis, OR 97331

8. Performing Organization Report No.

9. Performing Organization Name and Address

Oregon Department of Transportation
Research Group
200 Hawthorne Ave. SE, Suite B-240
Salem, OR 97301-5192

10. Work Unit No. (TRAIS)

11. Contract or Grant No.

SPR 316

12. Sponsoring Agency Name and Address

Oregon Department of Transportation
Research Group
200 Hawthorne Ave. SE, Suite B-240
Salem, OR 97301-5192

and

Federal Highway Administration
400 Seventh Street SW
Washington, DC 20590

13. Type of Report and Period Covered

Final Report

14. Sponsoring Agency Code

15. Supplementary Notes

16. Abstract

Linear and non-linear finite element method models were developed for a reinforced concrete bridge that had been strengthened with fiber reinforced polymer (FRP) composites. ANSYS and SAP2000 modeling software were used; however, most of the development effort used ANSYS. The model results agreed well with measurements from full-size laboratory beams and the actual bridge. As expected, a comparison using model results showed that the structural behavior of the bridge before and after strengthening was nearly the same for legal loads. Guidelines for developing finite element models for reinforced concrete bridges were discussed.

17. Key Words

finite element method, FEM, model, ANSYS, SAP2000, bridge, reinforced concrete, fiber reinforced, FRP, composite, strengthening, strain

18. Distribution Statement

Available from NTIS

19. Security Classification (of this report) Unclassified	20. Security Classification (of this page) Unclassified	21. No. of Pages 111 + appendices	22. Price

Technical Report Form DOT F 1700.7 (8-72) Reproduction of completed page authorized ♻ Printed on recycled paper

SI* (MODERN METRIC) CONVERSION FACTORS

APPROXIMATE CONVERSIONS TO SI UNITS

Symbol	When You Know	Multiply By	To Find	Symbol
		LENGTH		
in	inches	25.4	millimeters	mm
ft	feet	0.305	meters	m
yd	yards	0.914	meters	m
mi	miles	1.61	kilometers	km
		AREA		
in^2	square inches	645.2	millimeters squared	mm^2
ft^2	square feet	0.093	meters squared	m^2
yd^2	square yards	0.836	meters squared	m^2
ac	acres	0.405	hectares	ha
mi^2	square miles	2.59	kilometers squared	km^2
		VOLUME		
fl oz	fluid ounces	29.57	milliliters	mL
gal	gallons	3.785	liters	L
ft^3	cubic feet	0.028	meters cubed	m^3
yd^3	cubic yards	0.765	meters cubed	m^3
NOTE: Volumes greater than 1000 L shall be shown in m^3.				
		MASS		
oz	ounces	28.35	grams	g
lb	pounds	0.454	kilograms	kg
T	short tons (2000 lb)	0.907	megagrams	Mg
		TEMPERATURE (exact)		
°F	Fahrenheit temperature	5(F-32)/9	Celsius temperature	°C

APPROXIMATE CONVERSIONS FROM SI UNITS

Symbol	When You Know	Multiply By	To Find	Symbol
		LENGTH		
mm	millimeters	0.039	inches	in
m	meters	3.28	feet	ft
m	meters	1.09	yards	yd
km	kilometers	0.621	miles	mi
		AREA		
mm^2	millimeters squared	0.0016	square inches	in^2
m^2	meters squared	10.764	square feet	ft^2
ha	hectares	2.47	acres	ac
km^2	kilometers squared	0.386	square miles	mi^2
		VOLUME		
mL	milliliters	0.034	fluid ounces	fl oz
L	liters	0.264	gallons	gal
m^3	meters cubed	35.315	cubic feet	ft^3
m^3	meters cubed	1.308	cubic yards	yd^3
		MASS		
g	grams	0.035	ounces	oz
kg	kilograms	2.205	pounds	lb
Mg	megagrams	1.102	short tons (2000 lb)	T
		TEMPERATURE (exact)		
°C	Celsius temperature	1.8 + 32	Fahrenheit	°F

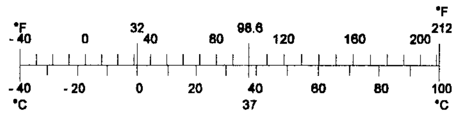

* SI is the symbol for the International System of Measurement

(4-7-94 jbp)

ACKNOWLEDGEMENTS

The authors would like to thank Mr. Steven Soltesz, Project Manager, Mr. Alan Kirk, Research Analyst, and Dr. Barnie Jones, Research Manager, of the ODOT Research Group for their valuable suggestions and many contributions to this project.

DISCLAIMER

This document is disseminated under the sponsorship of the Oregon Department of Transportation and the United States Department of Transportation in the interest of information exchange. The State of Oregon and the United States Government assume no liability of its contents or use thereof.

The contents of this report reflect the views of the author(s) who are solely responsible for the facts and accuracy of the data presented herein. The contents do not necessarily reflect the official policies of the Oregon Department of Transportation or the United States Department of Transportation.

The State of Oregon and the United States Government do not endorse products of manufacturers. Trademarks or manufacturers' names appear herein only because they are considered essential to the object of this document.

This report does not constitute a standard, specification, or regulation.

FINITE ELEMENT MODELING
OF REINFORCED CONCRETE STRUCTURES
STRENGTHENED WITH FRP LAMINATES

TABLE OF CONTENTS

1.0 INTRODUCTION 1
- 1.1 IMPORTANCE OF FRP RETROFIT FOR REINFORCED CONCRETE STRUCTURES 1
- 1.2 OBJECTIVES 2
- 1.3 SCOPE 2
- 1.4 COMPUTER MODELING OF FRP-STRENGTHENED STRUCTURES 2

2.0 MODELING FULL-SIZE REINFORCED CONCRETE BEAMS 5
- 2.1 FULL-SIZE BEAMS 5
- 2.2 ELEMENT TYPES 6
  - 2.2.1 Reinforced Concrete 6
  - 2.2.2 FRP Composites 7
  - 2.2.3 Steel Plates 7
- 2.3 MATERIAL PROPERTIES 8
  - 2.3.1 Concrete 8
  - 2.3.2 Steel Reinforcement and Steel Plates 14
  - 2.3.3 FRP Composites 15
- 2.4 GEOMETRY 17
- 2.5 FINITE ELEMENT DISCRETIZATION 25
- 2.6 LOADING AND BOUNDARY CONDITIONS 29
- NONLINEAR SOLUTION 31
  - 2.7.1 Load Stepping and Failure Definition for FE Models 32
- 2.8 COMPUTATION RESOURCES 34

3.0 RESULTS FROM FINITE ELEMENT ANALYSIS OF FULL-SIZE BEAMS 35
- 3.1 LOAD-STRAIN PLOTS 35
  - 3.1.1 Tensile Strain in Main Steel Reinforcing 35
  - 3.1.2 Tensile Strain in FRP Composites 41
  - 3.1.3 Compressive Strain in Concrete 43
- 3.2 LOAD-DEFLECTION PLOTS 46
- 3.3 FIRST CRACKING LOADS 51
- 3.4 EVOLUTION OF CRACK PATTERNS 51
- 3.5 LOADS AT FAILURE 57
- 3.6 CRACK PATTERNS AT FAILURE 59
- 3.7 MAXIMUM STRESSES IN FRP COMPOSITES 62
  - 3.7.1 Comparisons to Parallel Research 63

Preceding Page Blank

4.0 ANALYSIS OF HORSETAIL CREEK BRIDGE 65
4.1 INTRODUCTION 65
4.2 BRIDGE DESCRIPTION AND FIELD DATA 65
4.2.1 Horsetail Creek Bridge 65
4.2.2 Loading conditions 65
4.2.3 Field data 67
4.3 FEM MODEL 68
4.3.1 Materials properties 68
4.3.2 Bridge modeling and analysis assumptions 69
4.3.3 Finite element discretization 70
4.4 COMPARISONS OF ANSYS AND SAP 2000 PREDICTIONS WITH FIELD DATA 76
4.4.1 Analysis of responses to empty truck load 87
4.4.2 Analysis of responses to full truck load 87
4.4.3 Analysis of responses in general 88
4.5 ANALYSIS OF THE UNSTRENGTHENED HORSETAIL CREEK BRIDGE 89
5.0 CONCLUSIONS AND RECOMMENDATIONS 91
5.1 SUMMARY AND CONCLUSIONS 91
5.1.1 Conclusions for finite element models of the full-scale beams 91
5.1.2 Conclusions for finite element models of the Horsetail Creek Bridge 91
5.2 RECOMMENDATIONS 92
5.2.1 Recommended FE modeling and analysis procedure 92
5.2.2 Recommended FE modeling procedure for reinforced concrete beams 93
5.2.3 Recommended FE modeling procedure for the reinforced concrete bridge 94
6.0 REFERENCES 95

APPENDICES

APPENDIX A: STRUCTURAL DETAILS OF THE HORSETAIL CREEK BRIDGE
APPENDIX B: CONFIGURATION OF DUMP TRUCK FOR STATIC TESTS ON THE HORSETAIL CREEK BRIDGE
APPENDIX C: LOCATIONS OF FIBER OPTIC SENSORS ON THE HORSETAIL CREEK BRIDGE

LIST OF FIGURES

Figure 2.1: Solid65 – 3-D reinforced concrete solid (*ANSYS 1998*) 6
Figure 2.2: Link8 – 3-D spar (*ANSYS 1998*) 7
Figure 2.3: Solid46 – 3-D layered structural solid (*ANSYS 1998*) 7
Figure 2.4: Solid45 – 3-D solid (*ANSYS 1998*) 8
Figure 2.5: Typical uniaxial compressive and tensile stress-strain curve for concrete (*Bangash 1989*) 9
Figure 2.6: Simplified compressive uniaxial stress-strain curve for concrete 12
Figure 2.7: 3-D failure surface for concrete (*ANSYS 1998*) 13
Figure 2.8: Stress-strain curve for steel reinforcement 14
Figure 2.9: Schematic of FRP composites (*Gibson 1994, Kaw 1997*) 15
Figure 2.10: Stress-strain curves for the FRP composites in the direction of the fibers 16
Figure 2.11: Typical beam dimensions (not to scale) 18

Figure 2.12: Use of a quarter beam model (not to scale) 18
Figure 2.13: Typical steel reinforcement locations (not to scale) (*McCurry and Kachlakev 2000*) 19
Figure 2.14: Typical steel reinforcement for a quarter beam model. Reinforcement at the common faces was entered into the model as half the actual diameter. (not to scale) 20
Figure 2.15: Element connectivity: (a) concrete solid and link elements; (b) concrete solid and FRP layered solid elements 21
Figure 2.16: FRP reinforcing schemes (not to scale): (a) Flexure Beam; (b) Shear Beam; (c) Flexure/Shear Beam (*McCurry and Kachlakev 2000*) 22
Figure 2.17: Modified dimensions of FRP reinforcing for strengthened beam models (not to scale): (a) Flexure Beam; (b) Shear Beam; (c) Flexure/Shear Beam 24
Figure 2.18: Convergence study on plain concrete beams: (a), (b), (c), and (d) show the comparisons between ANSYS and SAP2000 for the tensile and compressive stresses; and strain and deflection at center midspan of the beams, respectively. 26
Figure 2.19: Results from convergence study: (a) deflection at midspan; (b) compressive stress in concrete; (c) tensile stress in main steel reinforcement 27
Figure 2.20: FEM discretization for a quarter of Control Beam 28
Figure 2.21: Loading and support locations (not to scale) (*McCurry and Kachlakev 2000*) 29
Figure 2.22: Steel plate with line support 30
Figure 2.23: Loading and boundary conditions (not to scale) 30
Figure 2.24: Displacements of model: (a) without rotation of steel plate (b) with rotation of steel plate 31
Figure 2.25: Newton-Raphson iterative solution (2 load increments) (*ANSYS 1998*) 32
Figure 2.26: Reinforced concrete behavior in Flexure/Shear Beam 33
Figure 3.1: Selected strain gauge locations (not to scale) 35
Figure 3.2: Load-tensile strain plot for #7 steel rebar in Control Beam 36
Figure 3.3: Load-tensile strain plot for #7 steel rebar in Flexure Beam 37
Figure 3.4: Load-tensile strain plot for #7 steel rebar in Shear Beam 37
Figure 3.5: Load-tensile strain plot for #6 steel rebar in Flexure/Shear Beam (Beam did not fail during actual loading.) 38
Figure 3.6: Variation of tensile force in steel for reinforced Concrete Beam: (a) typical cracking; (b) cracked concrete section; (c) bond stresses acting on reinforcing bar; (d) variation of tensile force in steel (*Nilson 1997*) 39
Figure 3.7: Development of tensile force in the steel for finite element models: (a) typical smeared cracking; (b) cracked concrete and steel rebar elements; (c) profile of tensile force in steel elements 40
Figure 3.8: Load versus tensile strain in the CFRP for the Flexure Beam 41
Figure 3.9: Load versus tensile strain in the GFRP for the Shear Beam 42
Figure 3.10: Load versus tensile strain in the CFRP for the Flexure/Shear Beam (Actual beam did not fail) 42
Figure 3.11: Load-compressive strain plot for concrete in Control Beam 43
Figure 3.12: Load-compressive strain plot for concrete in Flexure Beam 44
Figure 3.13: Load-compressive strain plot for concrete in Shear Beam 45
Figure 3.14: Load-compressive strain plot for concrete in Flexure/Shear Beam (Actual beam did not fail.) 45
Figure 3.15: Load-deflection plot for Control Beam 46
Figure 3.16: Load-deflection plot for Flexure Beam 47
Figure 3.17: Load-deflection plot for Shear Beam 48
Figure 3.18: Load-deflection plot for Flexure/Shear Beam (Actual beam did not fail) 49
Figure 3.19: Load-deflection plots for the four beams based on measurements (Beam No.4 did not fail) (*Kachlakev and McCurry 2000*) 50
Figure 3.20: Load-deflection plots for the four beams based on ANSYS finite element models 50
Figure 3.21: Integration points in concrete solid element (*ANSYS 1998*) 52
Figure 3.22: Cracking sign (*ANSYS 1998*) 52
Figure 3.23: Coordinate system for finite element models 52
Figure 3.24: Typical cracking signs occurring in finite element models: (a) flexural cracks; (b) compressive cracks; (c) diagonal tensile cracks 53
Figure 3.25: Evolution of crack patterns: (a) Control Beam; (b) Flexure Beam 55
Figure 3.26: Evolution of crack patterns (Continued): (a) Shear Beam; (b) Flexure/Shear Beam 56
Figure 3.27: Toughening mechanisms: (a) aggregate bridging; (b) crack-face friction (*Shah, et al. 1995*) 57

Figure 3.27 (continued): Toughening mechanisms: (c) crack tip blunted by void; (d) crack branching (*Shah, et al. 1995*) 58
Figure 3.28: Stress-strain curve for reinforcing steel: (a) as determined by tension test; (b) idealized (*Spiegel and Limbrunner 1998*) 58
Figure 3.29: Crack patterns at failure: (a) Control Beam; (b) Flexure Beam 60
Figure 3.30: Crack patterns at failure: (a) Shear Beam; (b) Flexure/Shear Beam 61
Figure 3.31: Locations of maximum stresses in FRP composites: (a) Flexure Beam; (b) Shear Beam 62
Figure 3.31 (continued): Locations of maximum stresses in FRP composites: (c) Flexure/Shear Beam 63
Figure 4.1: Locations of truck on the Horsetail Creek Bridge 66
Figure 4.1 (continued): Locations of truck on the Horsetail Creek Bridge 67
Figure 4.2: Locations of the monitored beams on the Horsetail Creek Bridge 68
Figure 4.3: Truck load simplification: (a) and (b) show configurations of the dump truck and the simplified truck, respectively 69
Figure 4.4: Linear truck load distribution 70
Figure 4.5: Steel reinforcement details: (a) and (b) show typical reinforcement in the transverse and longitudinal beams at the middle and at the end of the bridge, respectively 71
Figure 4.5 (continued): Steel reinforcement details: (c) and (d) show typical reinforcement in the bridge deck at both ends of the bridge 72
Figure 4.5 (continued): Steel reinforcement details: (e) shows typical reinforcement in the columns 73
Figure 4.6: FE bridge model with FRP laminates: (a), (b), and (c) show the FRP strengthening in different views 74
Figure 4.7: Boundary conditions for the bridge 75
Figure 4.8: Fiber optic sensor (plan view) 77
Figure 4.9: Comparison of strains from Field Tests 1 and 2, ANSYS, and SAP2000 for the empty truck at the seven Locations: (a) - (d) show the strains on the transverse beam 79
Figure 4.9 (continued): Comparison of strains from Field Tests 1 and 2, ANSYS, and SAP2000 for the empty truck at the seven Locations: (e)-(h) show the strains on the longitudinal beam. 80
Figure 4.10: Comparison of strains from Field Tests 1 and 2, ANSYS, and SAP2000 for the empty truck at the seven locations: (a) - (d) show the strains on the transverse beam 81
Figure 4.10 (continued): Comparison of strains from Field Tests 1 and 2, ANSYS, and SAP2000 for the empty truck at the seven locations: (e)-(h) show the strains on the longitudinal beam. 82
Figure 4.11: Comparison of strain versus distance of the single axle from the end of the bridge deck for Field Tests 1 and 2, ANSYS, and SAP2000 based on an empty truck: (a) - (d) show the strains on the transverse beam 83
Figure 4.11 (continued): Comparison of strain versus distance of the single axle from the end of the bridge deck for Field Tests 1 and 2, ANSYS, and SAP2000 based on an empty truck: (e)-(h) show the strains on the longitudinal beam 84
Figure 4.12: Comparison of strain versus distance of the single axle from the end of the bridge deck for Field Tests 1 and 2, ANSYS, and SAP2000 based on a full truck: (a) - (d) show the strains on the transverse beam 85
Figure 4.12 (continued): Comparison of strain versus distance of the single axle from the end of the bridge deck for Field Tests 1 and 2, ANSYS, and SAP2000 based on a full truck: (e)-(h) show the strains on the longitudinal beam 86

LIST OF TABLES

Table 2.1: Summary of material properties for concrete 10
Table 2.2: Summary of material properties for FRP composites (*Kachlakev and McCurry 2000*) 17
Table 2.3: Numbers of elements used for finite element models 28
Table 2.4: Summary of load step sizes for Flexure/Shear Beam model 33
Table 3.1: Comparisons between experimental and ANSYS first cracking loads 51
Table 3.2: Comparisons between experimental ultimate loads and ANSYS final loads 57
Table 3.3: Maximum stresses developed in the FRP composites and the corresponding ultimate tensile strengths 62
Table 4.1: Material properties (*Kachlakev and McCurry 2000; Fyfe Corp. 1998*) 68
Table 4.2: Summary of the number of elements used in the bridge model 70
Table 4.3: Differences between ANSYS and SAP2000 bridge models 76
Table 4.4: Comparison of strains on the transverse beam between FE bridge models with and without FRP strengthening 89
Table 4.5: Comparison of strains on the longitudinal beam between FE bridge models with and without FRP strengthening 89

1.0 INTRODUCTION

1.1 IMPORTANCE OF FRP RETROFIT FOR REINFORCED CONCRETE STRUCTURES

A large number of reinforced concrete bridges in the U.S. are structurally deficient by today's standards. The main contributing factors are changes in their use, an increase in load requirements, or corrosion deterioration due to exposure to an aggressive environment. In order to preserve those bridges, rehabilitation is often considered essential to maintain their capability and to increase public safety (*Seible, et al. 1995; Kachlakev 1998*).

In the last decade, fiber reinforced polymer (FRP) composites have been used for strengthening structural members of reinforced concrete bridges. Many researchers have found that FRP composite strengthening is an efficient, reliable, and cost-effective means of rehabilitation (*Marshall and Busel 1996; Steiner 1996; Tedesco, et al. 1996; Kachlakev 1998*). Currently in the U.S., the American Concrete Institute Committee 440 is working to establish design recommendations for FRP application to reinforced concrete (*ACI 440 2000*).

The Horsetail Creek Bridge is an example of a bridge classified as structurally deficient (*Transportation Research Board 1999; Kachlakev 1998*). This historic Bridge, built in 1914, is in use on the Historic Columbia River Highway east of Portland, Oregon. It was not designed to carry the traffic loads that are common today. Load rating showed that the bridge had only 6% of the required shear capacity for the transverse beams, 34% of the required shear capacity for the longitudinal beams, and approximately 50% of the required flexural capacity for the transverse beams (*CH2M Hill 1997*). There were no shear stirrups in any of the beams. Some exposed, corroded reinforcing steel was found during an on-site inspection; otherwise, the overall condition of the structure was generally very good. In 1998, the Oregon Department of Transportation (ODOT) resolved to use FRP composites to reinforce the beams. Strengthening the beams with FRP composites was considered advantageous due to the historic nature of the bridge, limited funding, and time restrictions.

The load-carrying capacity of the bridge was increased by applying FRP sheets to the transverse and longitudinal beams. In the case of the transverse beams, both shear and flexural strengthening were required, while only shear strengthening was needed for the longitudinal beams. For flexural strengthening, carbon FRP (CFRP) composite was attached to the bottom of the beam with the fibers oriented along the length of the beam. For shear strengthening, glass FRP (GFRP) composite was wrapped from the bottom of the deck down the side of the beam around the bottom and up the other side to the deck. The fibers were oriented perpendicular to the length of the beam.

1.2 OBJECTIVES

After construction, ODOT initiated research projects to verify the FRP strengthening concept used on Horsetail Creek Bridge. Four full-size beams constructed as similarly as possible to the transverse beams of the Horsetail Creek Bridge were tested with different FRP configurations. The project discussed in this report – development of computer models to predict the behavior of the Bridge – used the data from the beam tests for validation. The objectives of the computer modeling were to:

- Examine the structural behavior of Horsetail Creek Bridge, with and without FRP laminates; and
- Establish a methodology for applying computer modeling to reinforced concrete beams and bridges strengthened with FRP laminates.

1.3 SCOPE

Finite element method (FEM) models were developed to simulate the behavior of four full-size beams from linear through nonlinear response and up to failure, using the ANSYS program (*ANSYS 1998*). Comparisons were made for load-strain plots at selected locations on the beams; load-deflection plots at midspan; first cracking loads; loads at failure; and crack patterns at failure. The models were subsequently expanded to encompass the linear behavior of the Horsetail Creek Bridge. Modeling simplifications and assumptions developed during this research are presented. The study compared strains from the FEM analysis with measured strains from load tests. Conclusions from the current research efforts and recommendations for future studies are included.

1.4 COMPUTER MODELING OF FRP-STRENGTHENED STRUCTURES

Typically, the behavior of reinforced concrete beams is studied by full-scale experimental investigations. The results are compared to theoretical calculations that estimate deflections and internal stress/strain distributions within the beams. Finite element analysis can also be used to model the behavior numerically to confirm these calculations, as well as to provide a valuable supplement to the laboratory investigations, particularly in parametric studies. Finite element analysis, as used in structural engineering, determines the overall behavior of a structure by dividing it into a number of simple elements, each of which has well-defined mechanical and physical properties.

Modeling the complex behavior of reinforced concrete, which is both nonhomogeneous and anisotropic, is a difficult challenge in the finite element analysis of civil engineering structures. Most early finite element models of reinforced concrete included the effects of cracking based on a pre-defined crack pattern (*Ngo and Scordelis 1967; Nilson 1968*). With this approach, changes in the topology of the models were required as the load increased; therefore, the ease and speed of the analysis were limited.

A smeared cracking approach was introduced using isoparametric formulations to represent the cracked concrete as an orthotropic material (*Rashid 1968*). In the smeared cracking approach, cracking of the concrete occurs when the principal tensile stress exceeds the ultimate tensile strength. The elastic modulus of the material is then assumed to be zero in the direction parallel to the principal tensile stress direction (*Suidan and Schnobrich 1973*).

Only recently have researchers attempted to simulate the behavior of reinforced concrete strengthened with FRP composites using the finite element method. A number of reinforced concrete beams strengthened with FRP plates were tested in the laboratory. Finite element analysis with the smeared cracking approach was used to simulate the behavior and failure mechanisms of those experimental beams (*Arduini, et al. 1997*). Comparisons between the experimental data and the results from finite element models showed good agreement, and the different failure mechanisms, from ductile to brittle, could be simulated. The FRP plates were modeled with two-dimensional plate elements in that study, however, and the crack patterns of those beams were not predicted by the finite element analysis. The two-dimensional plate elements are surface-like elements, which have no actual thickness. Therefore, stress and strain results at the actual surfaces of the FRP plates were estimated by theoretical calculations.

In addition, an entire FRP-strengthened reinforced concrete bridge was modeled by finite element analysis (*Tedesco, et al. 1999*). In that study truss elements were used to model the FRP composites. The results of the finite element analysis correlated well with the field test data and indicated that the external bonding of FRP laminates to the bridge girders reduced the average maximum deflections at midspan and reinforcing steel stresses by 9% and 11%, respectively.

2.0 MODELING FULL-SIZE REINFORCED CONCRETE BEAMS

2.1 FULL-SIZE BEAMS

Four full-size reinforced concrete beams, similar to the transverse beams of the Horsetail Creek Bridge, were fabricated and tested at Oregon State University (*Kachlakev and McCurry 2000*). Each beam had a different strengthening scheme as described below:

- A Control Beam with no FRP strengthening.
- A beam with unidirectional CFRP laminates attached to the bottom of the beam. The fibers were oriented along the length of the beam. This beam was referred to as the Flexure Beam.
- A beam with unidirectional GFRP laminates wrapped around the sides and the bottom of the beam. The direction of the fibers was perpendicular to the length of the beam. This beam was referred to as the Shear Beam.
- A beam with both CFRP and GFRP laminates as in the flexure and Shear Beams. This type of FRP strengthening was used on the transverse beams of the Horsetail Creek Bridge. The beam was referred to as the Flexure/Shear Beam.

Strain gauges were attached throughout the beams to record the structural behavior under load: at the top and bottom fibers of the concrete at the middle of the span; on the sides of the beams in the high shear region; on the reinforcing bars; and on the FRP laminates. Midspan deflection was measured throughout the loading.

The current study presents results from the finite element analysis of the four full-scale beams. The finite element model uses a smeared cracking approach and three-dimensional layered elements to model FRP composites. Comparisons between finite element results and those from the experimental beams are shown. Crack patterns obtained from the finite element analysis are compared to those observed for the experimental beams.

The ANSYS finite element program (*ANSYS 1998*), operating on a UNIX system, was used in this study to simulate the behavior of the four experimental beams. In general, the conclusions and methods would be very similar using other nonlinear FEA programs. Each program, however, has its own nomenclature and specialized elements and analysis procedures that need to be used properly. The designer/analyst must be thoroughly familiar with the finite element tools being used, and must progress from simpler to more complex problems to gain confidence in the use of new techniques.

This chapter discusses model development for the full-size beams. Element types used in the models are covered in Section 2.2 and the constitutive equations, assumptions, and parameters for the various materials are discussed in Section 2.3. Geometry of the models is presented in Section 2.4, and Section 2.5 discusses a preliminary convergence study for the beam models. Loading and boundary conditions are discussed in Section 2.6. Nonlinear analysis procedures and convergence criteria are in explained in Section 2.7. The reader can refer to a wide variety of finite element analysis textbooks for a more formal and complete introduction to basic concepts if needed.

2.2 ELEMENT TYPES

2.2.1 Reinforced Concrete

An eight-node solid element, Solid65, was used to model the concrete. The solid element has eight nodes with three degrees of freedom at each node – translations in the nodal x, y, and z directions. The element is capable of plastic deformation, cracking in three orthogonal directions, and crushing. The geometry and node locations for this element type are shown in Figure 2.1.

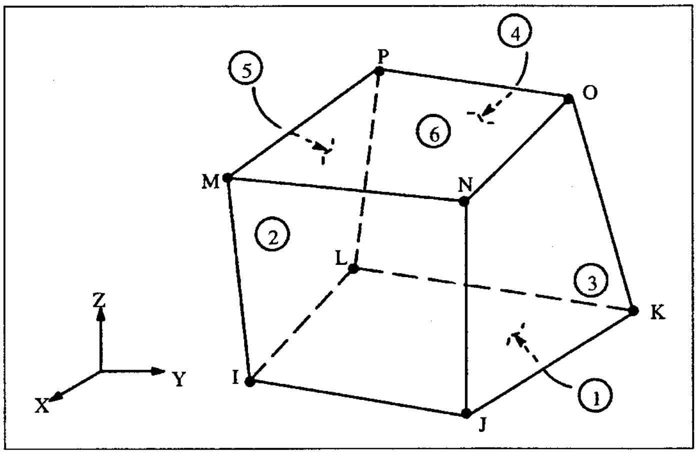

Figure 2.1: Solid65 – 3-D reinforced concrete solid (*ANSYS 1998*)

A Link8 element was used to model the steel reinforcement. Two nodes are required for this element. Each node has three degrees of freedom, – translations in the nodal x, y, and z directions. The element is also capable of plastic deformation. The geometry and node locations for this element type are shown in Figure 2.2.

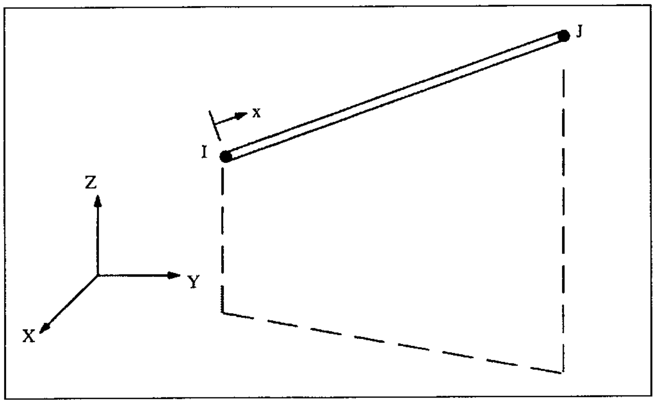

Figure 2.2: Link8 – 3-D spar (*ANSYS 1998*)

2.2.2 FRP Composites

A layered solid element, Solid46, was used to model the FRP composites. The element allows for up to 100 different material layers with different orientations and orthotropic material properties in each layer. The element has three degrees of freedom at each node and translations in the nodal x, y, and z directions. The geometry, node locations, and the coordinate system are shown in Figure 2.3.

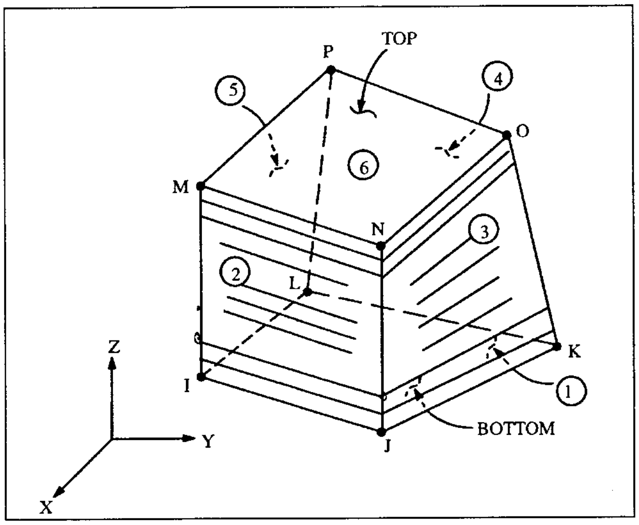

Figure 2.3: Solid46 – 3-D layered structural solid (*ANSYS 1998*)

2.2.3 Steel Plates

An eight-node solid element, Solid45, was used for the steel plates at the supports in the beam models. The element is defined with eight nodes having three degrees of freedom at each node –

translations in the nodal x, y, and z directions. The geometry and node locations for this element type are shown in Figure 2.4.

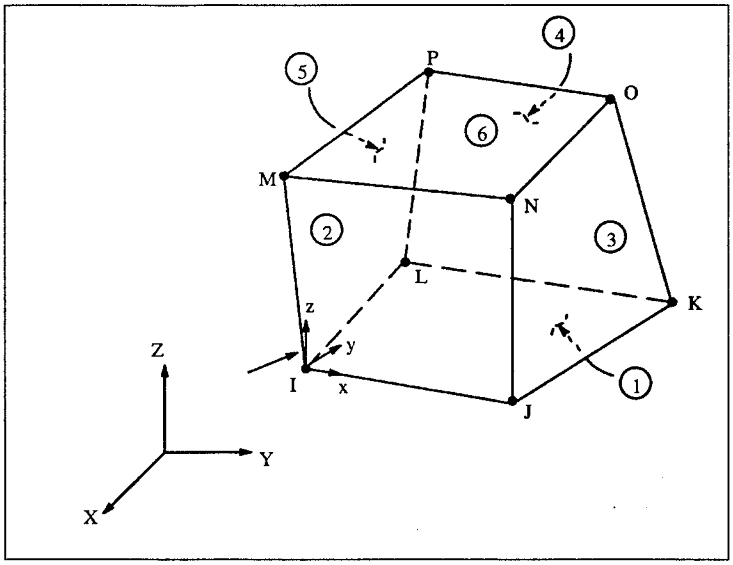

Figure 2.4: Solid45 – 3-D solid (*ANSYS 1998*)

2.3 MATERIAL PROPERTIES

2.3.1 Concrete

Development of a model for the behavior of concrete is a challenging task. Concrete is a quasi-brittle material and has different behavior in compression and tension. The tensile strength of concrete is typically 8-15% of the compressive strength (*Shah, et al. 1995*). Figure 2.5 shows a typical stress-strain curve for normal weight concrete (*Bangash 1989*).

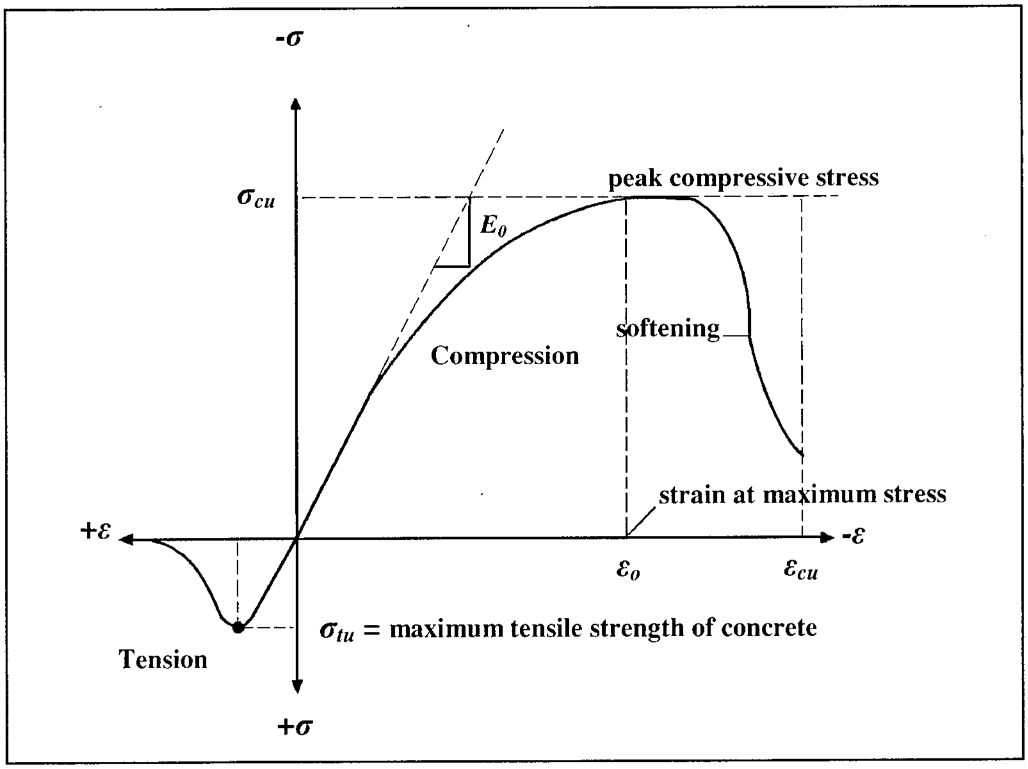

Figure 2.5: Typical uniaxial compressive and tensile stress-strain curve for concrete (*Bangash 1989*)

In compression, the stress-strain curve for concrete is linearly elastic up to about 30 percent of the maximum compressive strength. Above this point, the stress increases gradually up to the maximum compressive strength. After it reaches the maximum compressive strength σ_{cu}, the curve descends into a softening region, and eventually crushing failure occurs at an ultimate strain ε_{cu}. In tension, the stress-strain curve for concrete is approximately linearly elastic up to the maximum tensile strength. After this point, the concrete cracks and the strength decreases gradually to zero (*Bangash 1989*).

2.3.1.1 FEM Input Data

For concrete, ANSYS requires input data for material properties as follows:

Elastic modulus (E_c).
Ultimate uniaxial compressive strength (f'_c).
Ultimate uniaxial tensile strength (modulus of rupture, f_r).
Poisson's ratio (ν).
Shear transfer coefficient (β_t).
Compressive uniaxial stress-strain relationship for concrete.

For the full-scale beam tests (*Kachlakev and McCurry 2000*), an effort was made to accurately estimate the actual elastic modulus of the beams using the ultrasonic pulse velocity method (*ASTM 1983, ASTM 1994*). A correlation was made between pulse velocity and compressive elastic modulus following the ASTM standard methods. From this work, it was noted that each experimental beam had a slightly different elastic modulus; therefore, these values were used in the finite element modeling.

From the elastic modulus obtained by the pulse velocity method, the ultimate concrete compressive and tensile strengths for each beam model were calculated by Equations 2-1, and 2-2, respectively (*ACI 318, 1999*).

$$f_c' = \left(\frac{E_c}{57000}\right)^2 \quad \textbf{(2-1)}$$

$$f_r = 7.5\sqrt{f_c'} \quad \textbf{(2-2)}$$

where: E_c, f_c' and f_r are in psi.

Poisson's ratio for concrete was assumed to be 0.2 (*Bangash 1989*) for all four beams.

The shear transfer coefficient, β_t, represents conditions of the crack face. The value of β_t ranges from 0.0 to 1.0, with 0.0 representing a smooth crack (complete loss of shear transfer) and 1.0 representing a rough crack (no loss of shear transfer) (*ANSYS 1998*). The value of β_t used in many studies of reinforced concrete structures, however, varied between 0.05 and 0.25 (*Bangash 1989; Huyse, et al. 1994; Hemmaty 1998*). A number of preliminary analyses were attempted in this study with various values for the shear transfer coefficient within this range, but convergence problems were encountered at low loads with β_t less than 0.2. Therefore, the shear transfer coefficient used in this study was equal to 0.2. A summary of the concrete properties used in this finite element modeling study is shown in Table 2.1.

Table 2.1: Summary of material properties for concrete

Beam	**E_c MPa (ksi)***	**f_c' MPa (psi)**	**f_r MPa (psi)**	**v**	**β_t**
Control beam	19,350 (2,806)	16.71 (2,423)	2.546 (369.2)	0.2	0.2
Flexure beam	17,550 (2,545)	13.75 (1,994)	2.309 (334.9)	0.2	0.2
Shear beam	18,160 (2,634)	14.73 (2,136)	2.390 (346.6)	0.2	0.2
Flexure/Shear beam	17,080 (2,477)	13.02 (1,889)	2.247 (325.9)	0.2	0.2

*From pulse velocity measurements (*Kachlakev and McCurry 2000*)

2.3.1.2 Compressive Uniaxial Stress-Strain Relationship for Concrete

The ANSYS program requires the uniaxial stress-strain relationship for concrete in compression. Numerical expressions (*Desayi and Krishnan 1964*), Equations 2-3 and 2-4, were used along with Equation 2-5 (*Gere and Timoshenko 1997*) to construct the uniaxial compressive stress-strain curve for concrete in this study.

$$f = \frac{E_c \varepsilon}{1 + \left(\frac{\varepsilon}{\varepsilon_0} \right)^2} \tag{2-3}$$

$$\varepsilon_0 = \frac{2 f'_c}{E_c} \tag{2-4}$$

$$E_c = \frac{f}{\varepsilon} \tag{2-5}$$

where:

f = stress at any strain ε, psi
ε = strain at stress f
ε_0 = strain at the ultimate compressive strength f_c'

Figure 2.6 shows the simplified compressive uniaxial stress-strain relationship that was used in this study.

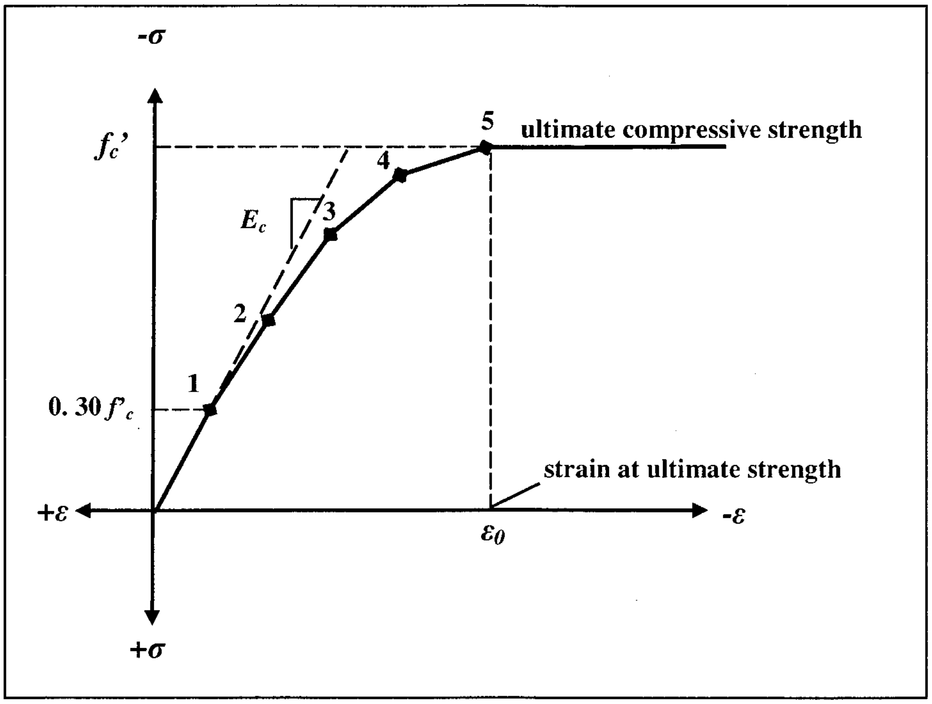

Figure 2.6: Simplified compressive uniaxial stress-strain curve for concrete

The simplified stress-strain curve for each beam model is constructed from six points connected by straight lines. The curve starts at zero stress and strain. Point No. 1, at 0.30 f'_c, is calculated for the stress-strain relationship of the concrete in the linear range (Equation 2-5). Point Nos. 2, 3, and 4 are obtained from Equation 2-3, in which ε_0 is calculated from Equation 2-4. Point No. 5 is at ε_0 and f'_c. In this study, an assumption was made of perfectly plastic behavior after Point No. 5.

An example is included here to demonstrate a calculation of the five points (1-5) on the curve using the Control Beam model. The model has a concrete elastic modulus of 2,806,000 psi. The value of f'_c calculated by Equation 2-1 is equal to 2423 psi. For Point No. 1, strain at a stress of 727 psi (0.3 f'_c) is obtained for a linear stress-strain relationship for concrete (Equation 2-5), and is 0.00026 in./in. Strain at the ultimate compressive strength, ε_0, is calculated by Equation 2-4, and equals 0.00173 in./in. Point Nos. 2, 3, and 4 are calculated from Equation 2-3, which gives strains of 0.00060, 0.00095 and 0.00130 in./in., corresponding to stresses of 1502, 2046 and 2328 psi, respectively. Finally, Point No. 5 is at the ultimate strength, f'_c of 2423 psi and ε_0 of 0.00173 in./in.

2.3.1.3 Failure Criteria for Concrete

The model is capable of predicting failure for concrete materials. Both cracking and crushing failure modes are accounted for. The two input strength parameters – i.e., ultimate uniaxial tensile and compressive strengths – are needed to define a failure surface for the concrete. Consequently, a criterion for failure of the concrete due to a multiaxial stress state can be calculated (*William and Warnke 1975*).

A three-dimensional failure surface for concrete is shown in Figure 2.7. The most significant nonzero principal stresses are in the x and y directions, represented by σ_{xp} and σ_{yp}, respectively. Three failure surfaces are shown as projections on the σ_{xp}-σ_{yp} plane. The mode of failure is a function of the sign of σ_{zp} (principal stress in the z direction). For example, if σ_{xp} and σ_{yp} are both negative (compressive) and σ_{zp} is slightly positive (tensile), cracking would be predicted in a direction perpendicular to σ_{zp}. However, if σ_{zp} is zero or slightly negative, the material is assumed to crush (*ANSYS 1998*).

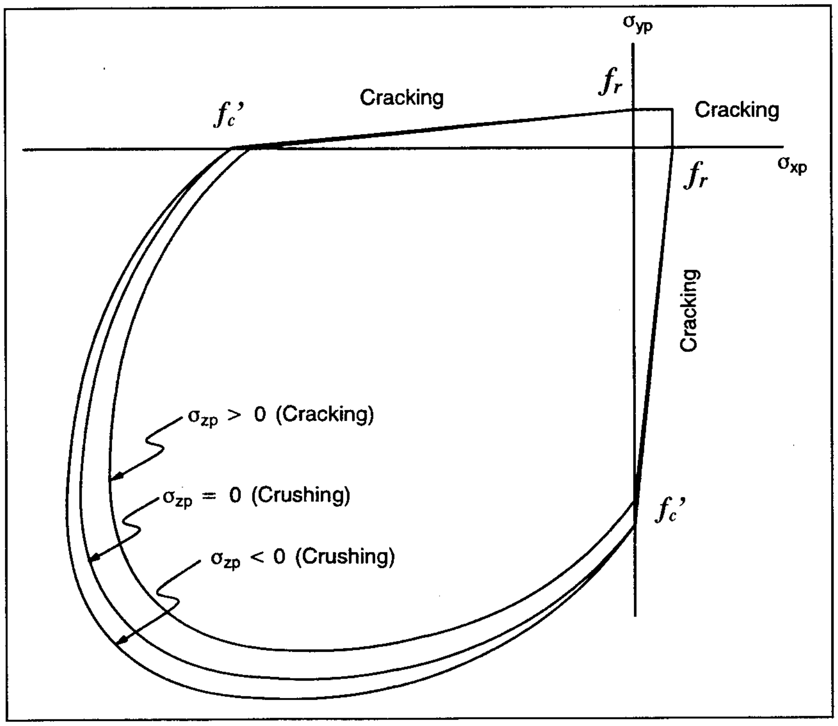

Figure 2.7: 3-D failure surface for concrete (*ANSYS 1998*)

In a concrete element, cracking occurs when the principal tensile stress in any direction lies outside the failure surface. After cracking, the elastic modulus of the concrete element is set to zero in the direction parallel to the principal tensile stress direction. Crushing occurs when all principal stresses are compressive and lie outside the failure surface; subsequently, the elastic modulus is set to zero in all directions (*ANSYS 1998*), and the element effectively disappears.

During this study, it was found that if the crushing capability of the concrete is turned on, the finite element beam models fail prematurely. Crushing of the concrete started to develop in elements located directly under the loads. Subsequently, adjacent concrete elements crushed within several load steps as well, significantly reducing the local stiffness. Finally, the model showed a large displacement, and the solution diverged.

A pure "compression" failure of concrete is unlikely. In a compression test, the specimen is subjected to a uniaxial compressive load. Secondary tensile strains induced by Poisson's effect occur perpendicular to the load. Because concrete is relatively weak in tension, these actually cause cracking and the eventual failure (*Mindess and Young 1981; Shah, et al. 1995*). Therefore, in this study, the crushing capability was turned off and cracking of the concrete controlled the failure of the finite element models.

2.3.2 Steel Reinforcement and Steel Plates

Steel reinforcement in the experimental beams was constructed with typical Grade 60 steel reinforcing bars. Properties, i.e., elastic modulus and yield stress, for the steel reinforcement used in this FEM study follow the design material properties used for the experimental investigation (*Kachlakev and McCurry 2000*). The steel for the finite element models was assumed to be an elastic-perfectly plastic material and identical in tension and compression. Poisson's ratio of 0.3 was used for the steel reinforcement in this study (*Gere and Timoshenko 1997*). Figure 2.8 shows the stress-strain relationship used in this study. Material properties for the steel reinforcement for all four models are as follows:

Elastic modulus, E_s = 200,000 MPa (29,000 ksi)
Yield stress, f_y = 410 MPa (60,000 psi)
Poisson's ratio, ν = 0.3

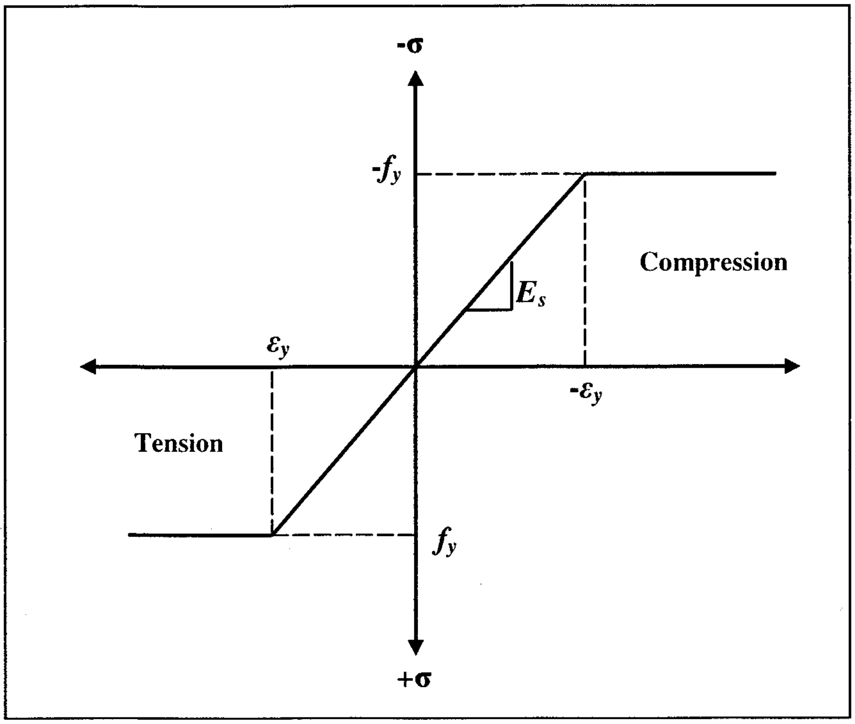

Figure 2.8: Stress-strain curve for steel reinforcement

Steel plates were added at support locations in the finite element models (as in the actual beams) to provide a more even stress distribution over the support areas. An elastic modulus equal to 200,000 MPa (29,000 ksi) and Poisson's ratio of 0.3 were used for the plates. The steel plates were assumed to be linear elastic materials.

2.3.3 FRP Composites

FRP composites are materials that consist of two constituents. The constituents are combined at a macroscopic level and are not soluble in each other. One constituent is the reinforcement, which is embedded in the second constituent, a continuous polymer called the matrix (*Kaw 1997*). The reinforcing material is in the form of fibers, i.e., carbon and glass, which are typically stiffer and stronger than the matrix. The FRP composites are anisotropic materials; that is, their properties are not the same in all directions. Figure 2.9 shows a schematic of FRP composites.

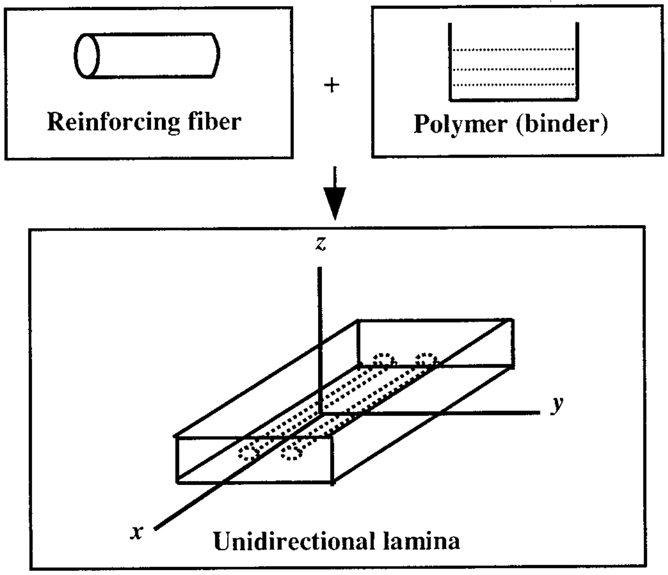

Figure 2.9: Schematic of FRP composites (*Gibson 1994, Kaw 1997*)

As shown in Figure 2.9, the unidirectional lamina has three mutually orthogonal planes of material properties (i.e., xy, xz, and yz planes). The xyz coordinate axes are referred to as the principal material coordinates where the x direction is the same as the fiber direction, and the y and z directions are perpendicular to the x direction. It is a so-called specially orthotropic material (*Gibson 1994, Kaw 1997*). In this study, the specially orthotropic material is also transversely isotropic, where the properties of the FRP composites are nearly the same in any direction perpendicular to the fibers. Thus, the properties in the y direction are the same as those in the z direction.

Glass fiber reinforced polymer was used for shear reinforcement on the Horsetail Falls Bridge because of its superior strain at failure. Carbon fiber reinforced polymer was used for flexural reinforcement because of its high tensile strength. Linear elastic properties of the FRP composites were assumed throughout this study. Figure 2.10 shows the stress-strain curves used in this study for the FRP composites in the direction of the fiber.

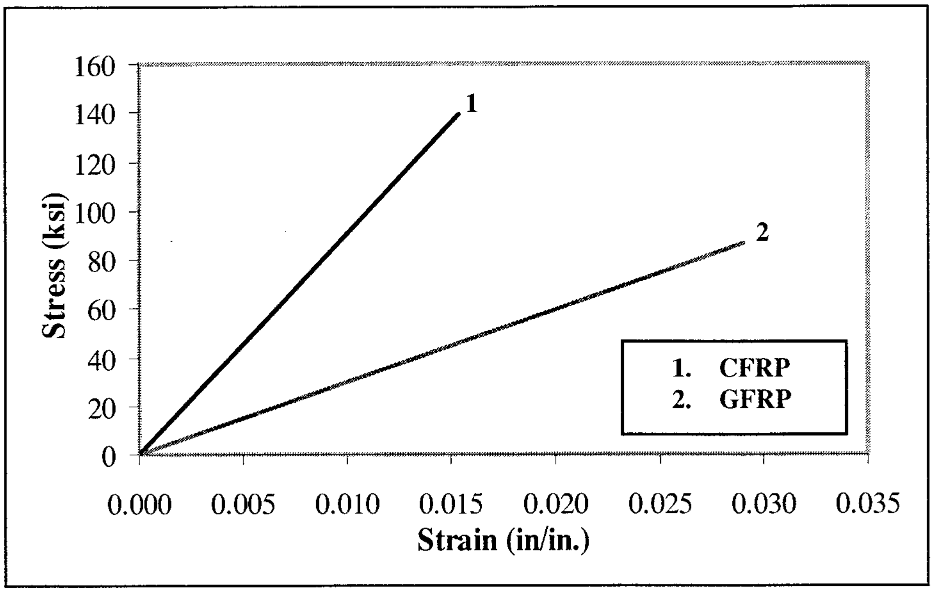

Figure 2.10: Stress-strain curves for the FRP composites in the direction of the fibers

Input data needed for the FRP composites in the finite element models are as follows:

- Number of layers.
- Thickness of each layer.
- Orientation of the fiber direction for each layer.
- Elastic modulus of the FRP composite in three directions (E_x, E_y and E_z).
- Shear modulus of the FRP composite for three planes (G_{xy}, G_{yz} and G_{xz}).
- Major Poisson's ratio for three planes (ν_{xy}, ν_{yz} and ν_{xz}).

Note that a local coordinate system for the FRP layered solid elements is defined where the x direction is the same as the fiber direction, while the y and z directions are perpendicular to the x direction.

The properties of isotropic materials, such as elastic modulus and Poisson's ratio, are identical in all directions; therefore no subscripts are required. This is not the case with specially orthotropic materials. Subscripts are needed to define properties in the various directions. For example, $E_x \neq E_y$ and $\nu_{xy} \neq \nu_{yx}$. E_x is the elastic modulus in the fiber direction, and E_y is the elastic modulus in the y direction perpendicular to the fiber direction. The use of Poisson's ratios for the orthotropic materials causes confusion; therefore, the orthotropic material data are supplied in the ν_{xy} or major Poisson's ratio format for the ANSYS program. The major Poisson's ratio is the ratio of strain in the y direction to strain in the perpendicular x direction when the applied stress is in the x direction. The quantity ν_{yx} is called a minor Poisson's ratio and is smaller than ν_{xy}, whereas E_x is larger than E_y. Equation 2-6 shows the relationship between ν_{xy} and ν_{yx} (*Kaw 1997*).

$$\nu_{yx} = \frac{E_y}{E_x}\nu_{xy} \tag{2-6}$$

where:

ν_{yx} = Minor Poisson's ratio

E_x = Elastic modulus in the x direction (fiber direction)

E_y = Elastic modulus in the y direction

ν_{xy} = Major Poisson's ratio

A summary of material properties used for the modeling of all four beams is shown in Table 2.2.

Table 2.2: Summary of material properties for FRP composites (*Kachlakev and McCurry 2000*)

FRP composite	Elastic modulus MPa (ksi)	Major Poisson's ratio	Tensile strength MPa (ksi)	Shear modulus MPa (ksi)	Thickness of laminate mm (in.)
CFRP	E_x = 62,000 (9000) E_y = 4800 (700)* E_z = 4800 (700)*	ν_{xy} = 0.22 ν_{xz} = 0.22 ν_{yz} = 0.30*	958 (139)	G_{xy} = 3270 (474)* G_{xz} = 3270 (474)* G_{yz} = 1860 (270)**	1.0 (0.040)
GFRP	E_x = 21,000 (3000) E_y = 7000 (1000)* E_z = 7000 (1000)*	ν_{xy} = 0.26 ν_{xz} = 0.26 ν_{yz} = 0.30*	600 (87)	G_{xy} = 1520 (220) G_{xz} = 1520 (220) G_{yz} = 2650 (385)**	1.3 (0.050)

*(*Kachlakev 1998*)

** $G_{yz} = \frac{E_{y\ or\ z}}{2(1+\nu_{yz})}$

2.4 GEOMETRY

The dimensions of the full-size beams were 305.0 mm x 6096 mm x 768.4 mm (12.00 in x 240.0 in x 30.25 in). The span between the two supports was 5486 mm (216.0 in). Figure 2.11 illustrates typical dimensions for all four beams before FRP reinforcing. By taking advantage of the symmetry of the beams, a quarter of the full beam was used for modeling. This approach reduced computational time and computer disk space requirements significantly. The quarter of the entire model is shown in Figure 2.12.

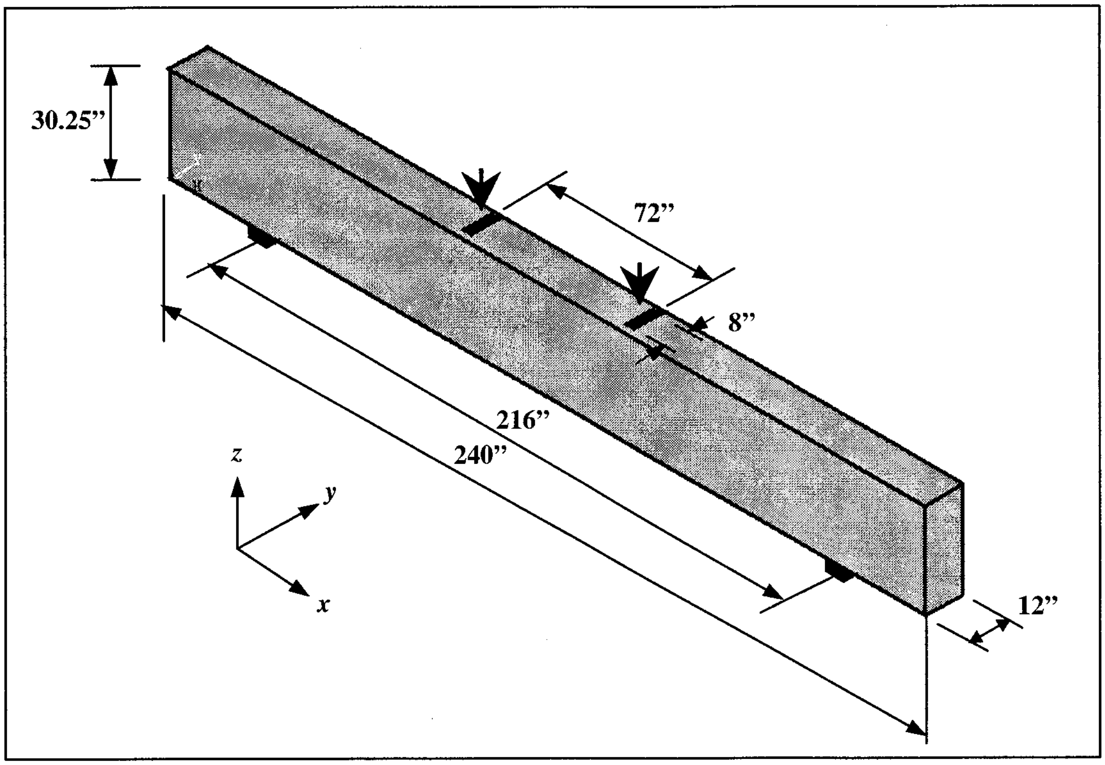

Figure 2.11: Typical beam dimensions (not to scale)

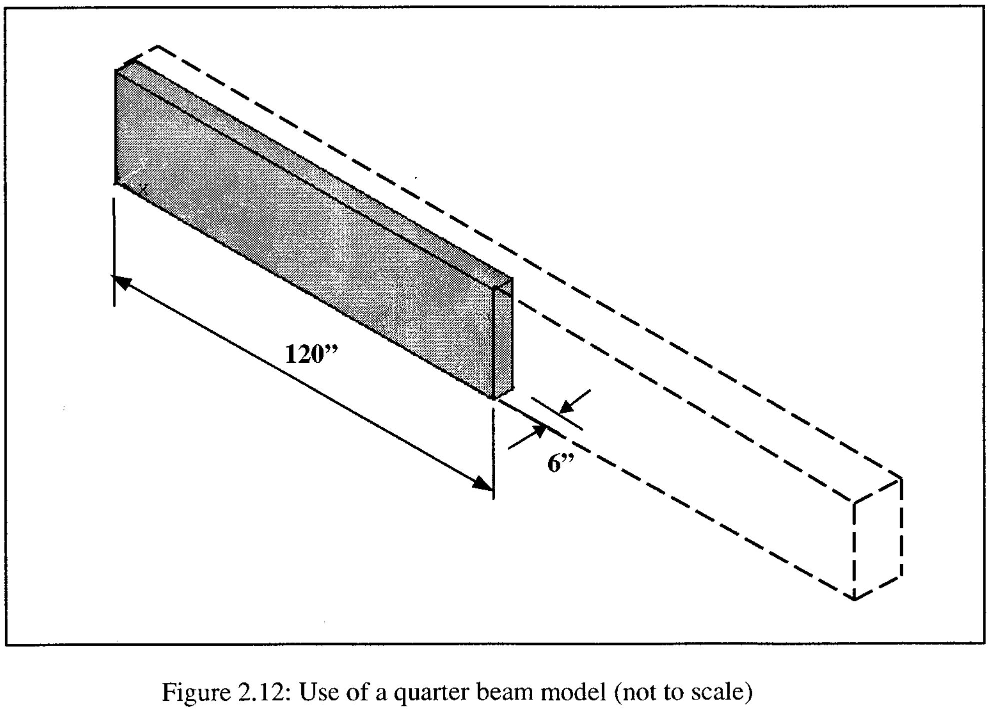

Figure 2.12: Use of a quarter beam model (not to scale)

Figure 2.13 shows typical steel reinforcement locations for the full-size beams. In the finite element models, 3-D spar elements, Link8, were employed to represent the steel reinforcement, referred to here as link elements. The steel reinforcement was simplified in the model by ignoring the inclined portions of the steel bars present in the test beams. Figure 2.14 shows typical steel reinforcement for a quarter beam model.

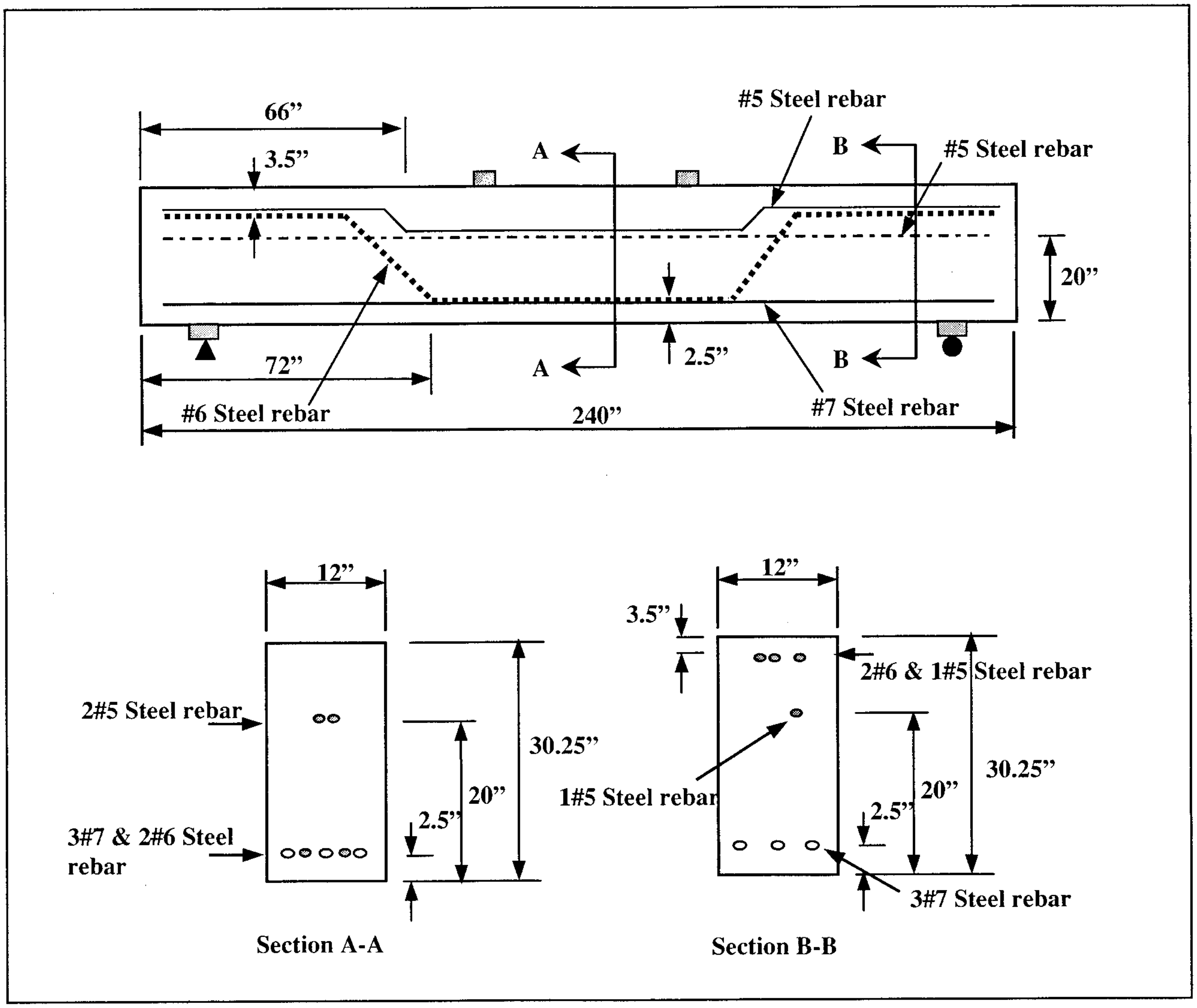

Figure 2.13: Typical steel reinforcement locations (not to scale) (*McCurry and Kachlakev 2000*)

Ideally, the bond strength between the concrete and steel reinforcement should be considered. However, in this study, perfect bond between materials was assumed. To provide the perfect bond, the link element for the steel reinforcing was connected between nodes of each adjacent concrete solid element, so the two materials shared the same nodes. The same approach was adopted for FRP composites. The high strength of the epoxy used to attach FRP sheets to the experimental beams supported the perfect bond assumption.

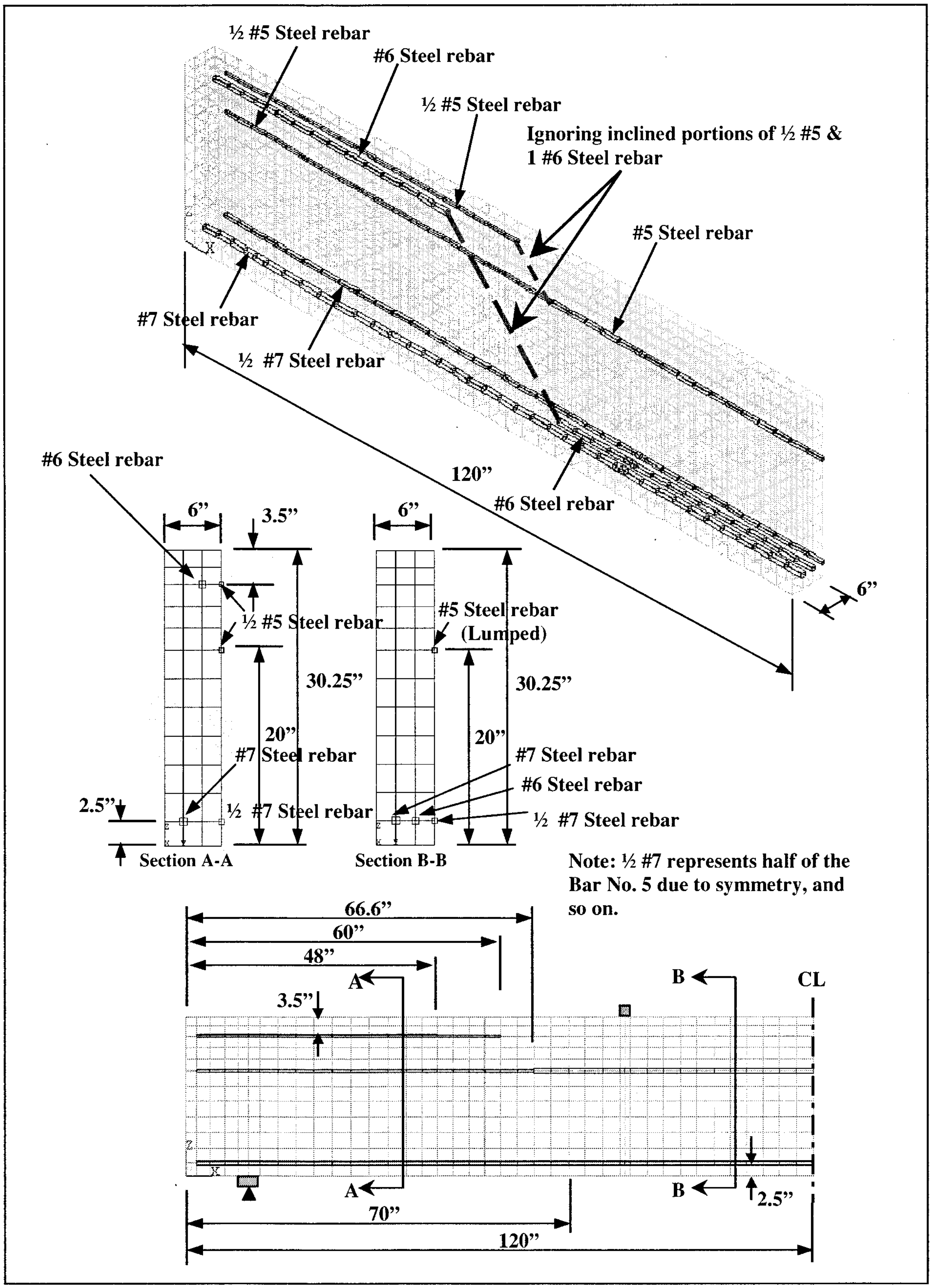

Figure 2.14: Typical steel reinforcement for a quarter beam model. Reinforcement at the common faces was entered into the model as half the actual diameter. (not to scale)

In the finite element models, layered solid elements, Solid46, were used to model the FRP composites. Nodes of the FRP layered solid elements were connected to those of adjacent concrete solid elements in order to satisfy the perfect bond assumption. Figure 2.15 illustrates the element connectivity.

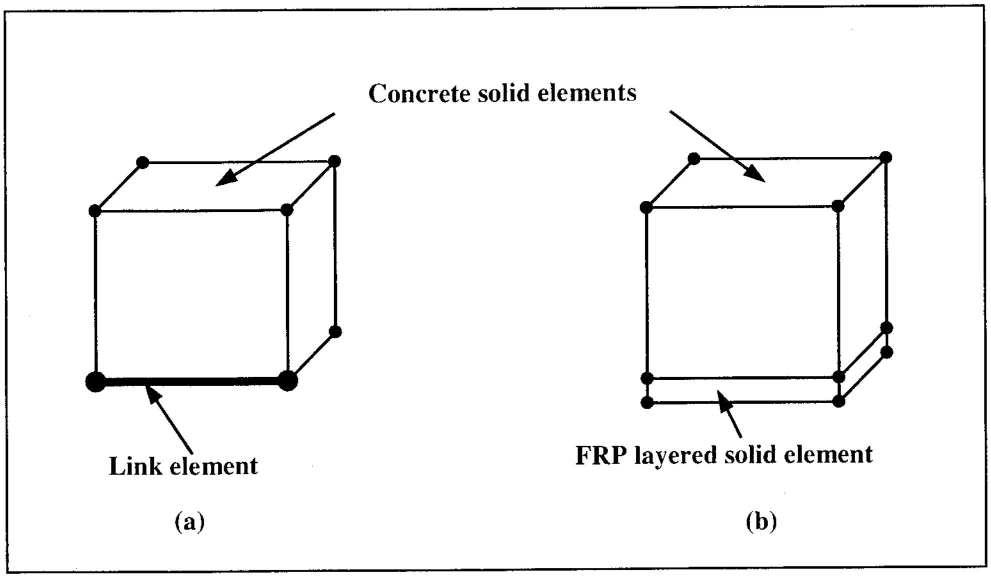

Figure 2.15: Element connectivity: (a) concrete solid and link elements; (b) concrete solid and FRP layered solid elements

Reinforcing schemes for the full-size beams are shown in Figure 2.16. The GFRP and CFRP composites had various thicknesses, depending upon the capacities needed at various locations on the beams.

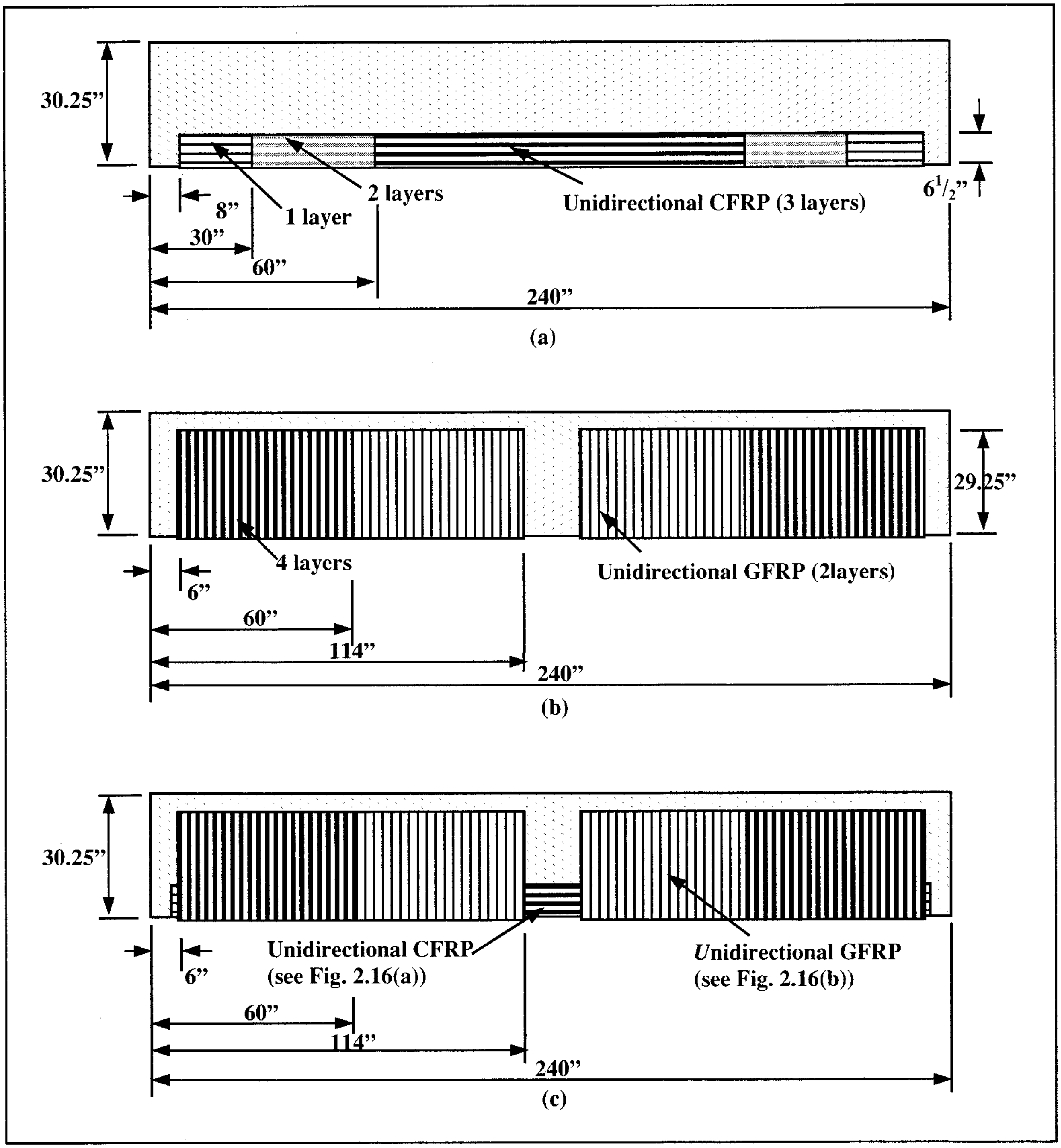

Figure 2.16: FRP reinforcing schemes (not to scale): (a) Flexure Beam; (b) Shear Beam; (c) Flexure/Shear Beam (*McCurry and Kachlakev 2000*)

The various thicknesses of the FRP composites create discontinuities, which are not desirable for the finite element analysis. These may develop high stress concentrations at local areas on the models; consequently, when the model is run, the solution may have difficulties in convergence. Therefore, a consistent overall thickness of FRP composite was used in the models to avoid discontinuities. The equivalent overall stiffness of the FRP materials was maintained by making compensating changes in the elastic and shear moduli assigned to each FRP layer. For example, if the thickness of an FRP laminate was artificially doubled to maintain a constant overall thickness, the elastic and shear moduli in that material were reduced by 50% to compensate. Note that the relationship between elastic and shear moduli is linear. Equation 2-7 shows the relationship between elastic and shear moduli (*ANSYS 1998*).

$$G_{xy} = \frac{E_x E_y}{E_x + E_y + 2\nu_{xy} E_x} \qquad \textbf{(2-7)}$$

where:

G_{xy} = Shear modulus in the *xy* plane
E_x = Elastic modulus in the x direction
E_y = Elastic modulus in the y direction
ν_{xy} = Major Poisson's ratio

For this study, minor modification of dimensions for the FRP reinforcing was made due to geometric constraints from the other elements in the models, i.e., meshing of concrete elements, steel rebar locations and required output locations. Figure 2.17 shows the modified dimensions of the FRP reinforcing schemes for the quarter beam models.

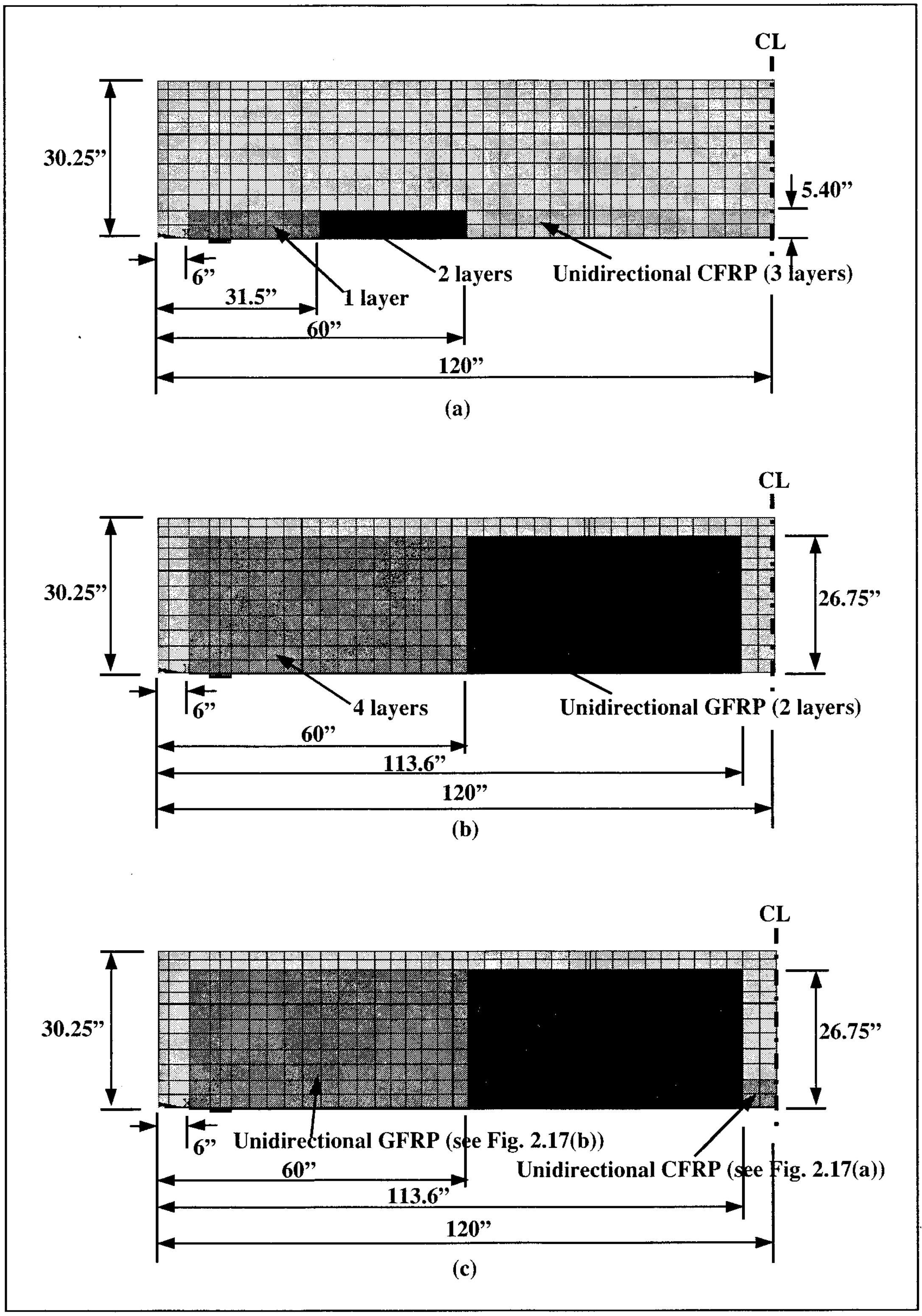

Figure 2.17: Modified dimensions of FRP reinforcing for strengthened beam models (not to scale): (a) Flexure Beam; (b) Shear Beam; (c) Flexure/Shear Beam

2.5 FINITE ELEMENT DISCRETIZATION

As an initial step, a finite element analysis requires meshing of the model. In other words, the model is divided into a number of small elements, and after loading, stress and strain are calculated at integration points of these small elements (*Bathe 1996*). An important step in finite element modeling is the selection of the mesh density. A convergence of results is obtained when an adequate number of elements is used in a model. This is practically achieved when an increase in the mesh density has a negligible effect on the results (*Adams and Askenazi 1998*). Therefore, in this finite element modeling study a convergence study was carried out to determine an appropriate mesh density.

Initially a convergence study was performed using plain concrete beams in a linear analysis. SAP2000, another general-purpose finite element analysis program, was also used to verify the ANSYS results in the linear analysis study (*OSU 2000*). The finite element models dimensionally replicated the full-scale transverse beams. That is, five 305.0 mm x 6096 mm x 768.4 mm (12.00 in x 240.0 in x 30.25 in) plain concrete beams with the same material properties were modeled in both ANSYS and SAP2000 with an increasing number of elements: 1536, 3072, 6144, 8192, and 12160 elements, respectively. Note that at this stage the advantage of geometrical symmetry was not utilized in these models. In other words, complete full-size beams were modeled. A number of response parameters was compared, including tensile stress, strain, deflection at the center bottom fiber of the beam, and compressive stress at the center top fiber of the beam. The four parameters were determined at the midspan of the beam. Comparisons of the results from ANSYS and SAP2000 were made, and the convergence of four response parameters is shown in Figure 2.18 for a plain concrete beam (not the reinforced concrete Control Beam) used in these preliminary convergence studies.

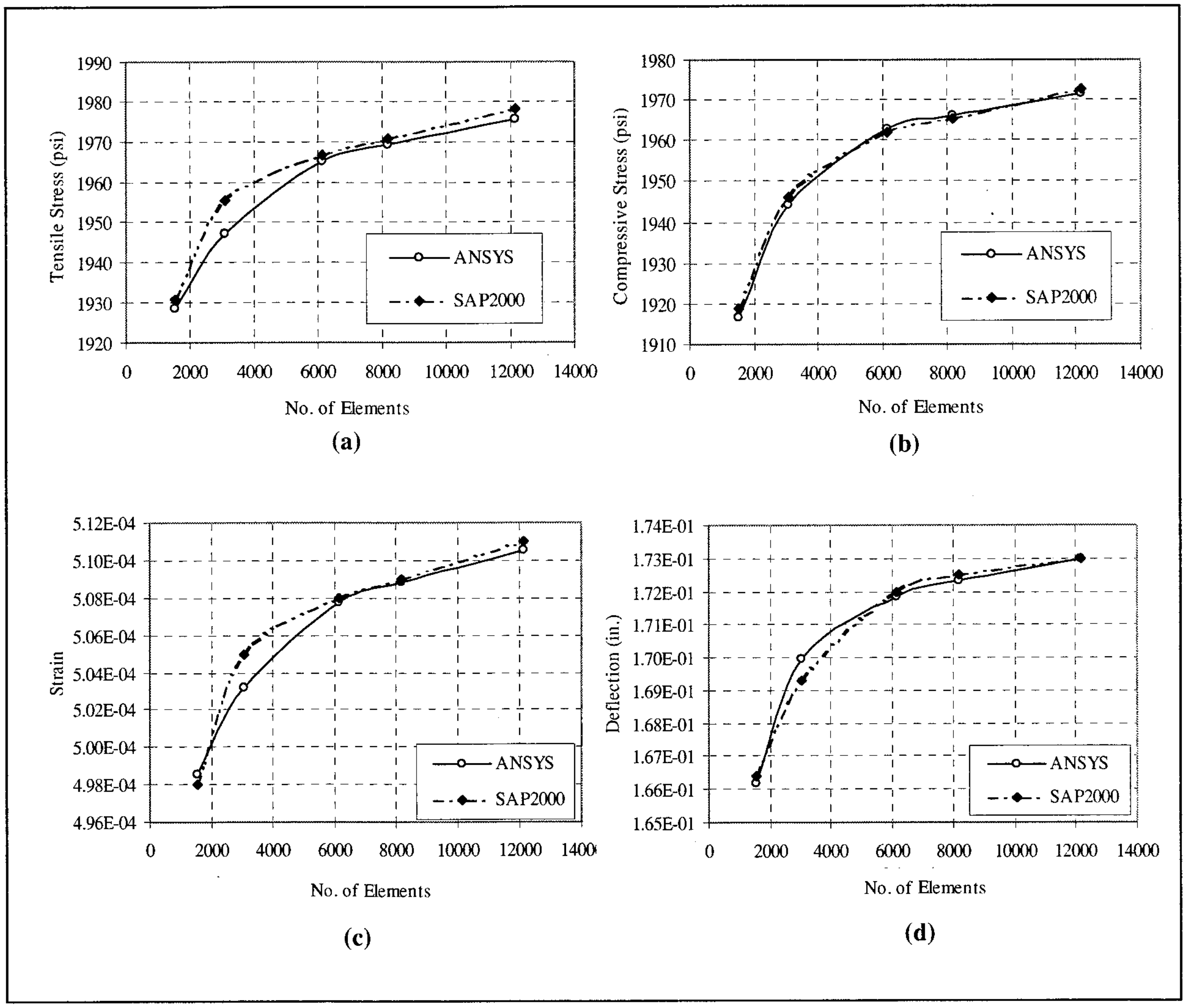

Figure 2.18: Convergence study on plain concrete beams: (a), (b), (c), and (d) show the comparisons between ANSYS and SAP2000 for the tensile and compressive stresses; and strain and deflection at center midspan of the beams, respectively.

As shown in Figure 2.18, both programs gave very similar results. The results started to converge with a model having 6144 elements. Although the plain concrete models were not a good representation of the large-scale beams, due to lack of steel reinforcement, they suggested that the number of concrete elements for the entire reinforced beam should be at least 6000.

Later, another convergence study was made using ANSYS. FEM beam models were developed based on the reinforced concrete Control Beam. Only quarters of the beams were modeled, taking advantage of symmetry. Four different numbers of elements – 896, 1136, 1580 and 2264 – were used to examine the convergence of the results. Three parameters at different locations were observed to see if the results converged. The outputs were collected at the same applied load as follows: deflection at midspan; compressive stress in concrete at midspan at the center of the top face of the beam models; and tensile stress in the main steel reinforcement at midspan. Figure 2.19 shows the results from the convergence study.

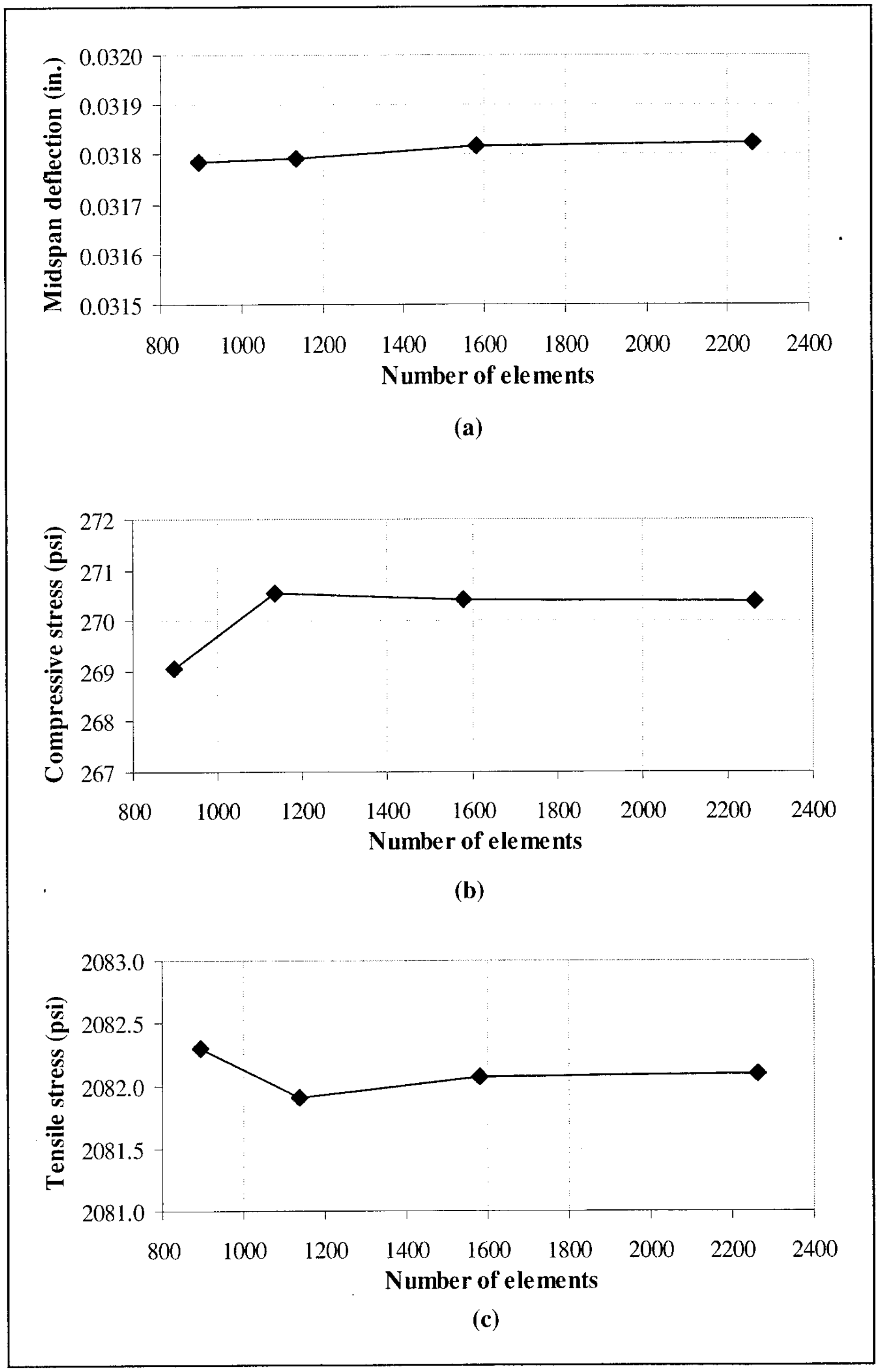

Figure 2.19: Results from convergence study: (a) deflection at midspan; (b) compressive stress in concrete; (c) tensile stress in main steel reinforcement

Figure 2.19 shows that the differences in the results were negligible when the number of elements increased from 1580 to 2264. Therefore, the 1580 element model, which was equivalent to 6320 elements in the full-beam model, was selected for the Control Beam model and used as the basis of the other three FRP-strengthened beam models as well. It can thus be seen that regardless of steel reinforcement, the results started to converge with a model having approximately 6000 elements for the entire beam.

Figure 2.20 shows meshing for the Control Beam model. A finer mesh near the loading location is required in order to avoid problems of stress concentration.

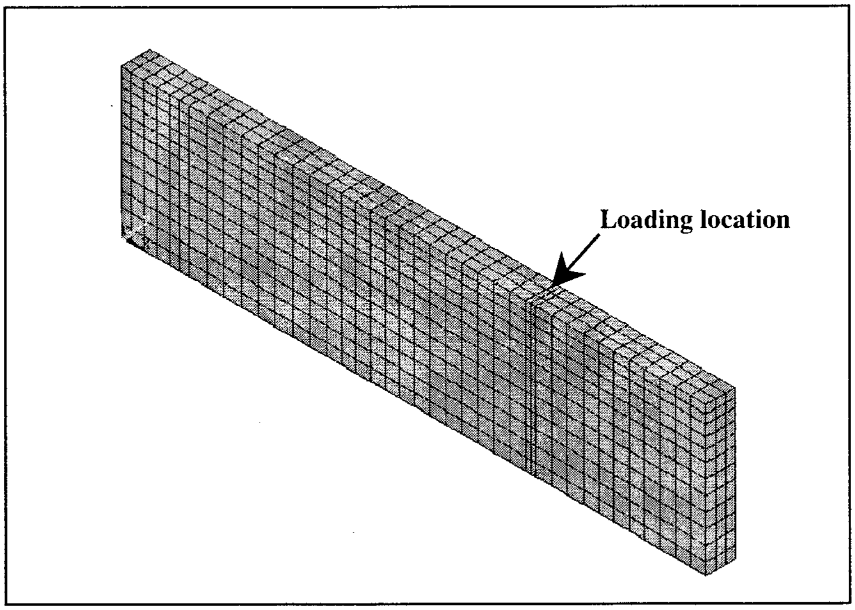

Figure 2.20: FEM discretization for a quarter of Control Beam

FRP layered solid elements are connected to the surfaces of the concrete solid elements of the Control Beam as shown in Figure 2.15(b). The dimensions for the FRP reinforcing schemes are shown in Figure 2.17. Numbers of elements used in this study are summarized in Table 2.3.

Table 2.3: Numbers of elements used for finite element models

Model	**Number of elements**				
	Concrete	**Steel reinforcement**	**FRP composites**	**Steel plate**	**Total**
Control Beam	1404	164	-	12	1580
Flexure Beam	1404	164	222	12	1802
Shear Beam	1404	164	490	12	2070
Flexure/Shear Beam	1404	164	1062	12	2642

2.6 LOADING AND BOUNDARY CONDITIONS

The four full-size beams were tested in third point bending, as shown in Figure 2.21. The finite element models were loaded at the same locations as the full-size beams. In the experiment, the loading and support dimensions were approximately 51 mm x 203 mm x 305 mm (2 in x 8 in x 12 in) and 102 mm x 305 mm (4 in x 12 in), respectively. A one-inch thick steel plate, modeled using Solid45 elements, was added at the support location in order to avoid stress concentration problems. This provided a more even stress distribution over the support area. Moreover, a single line support was placed under the centerline of the steel plate to allow rotation of the plate. Figure 2.22 illustrates the steel plate at the support.

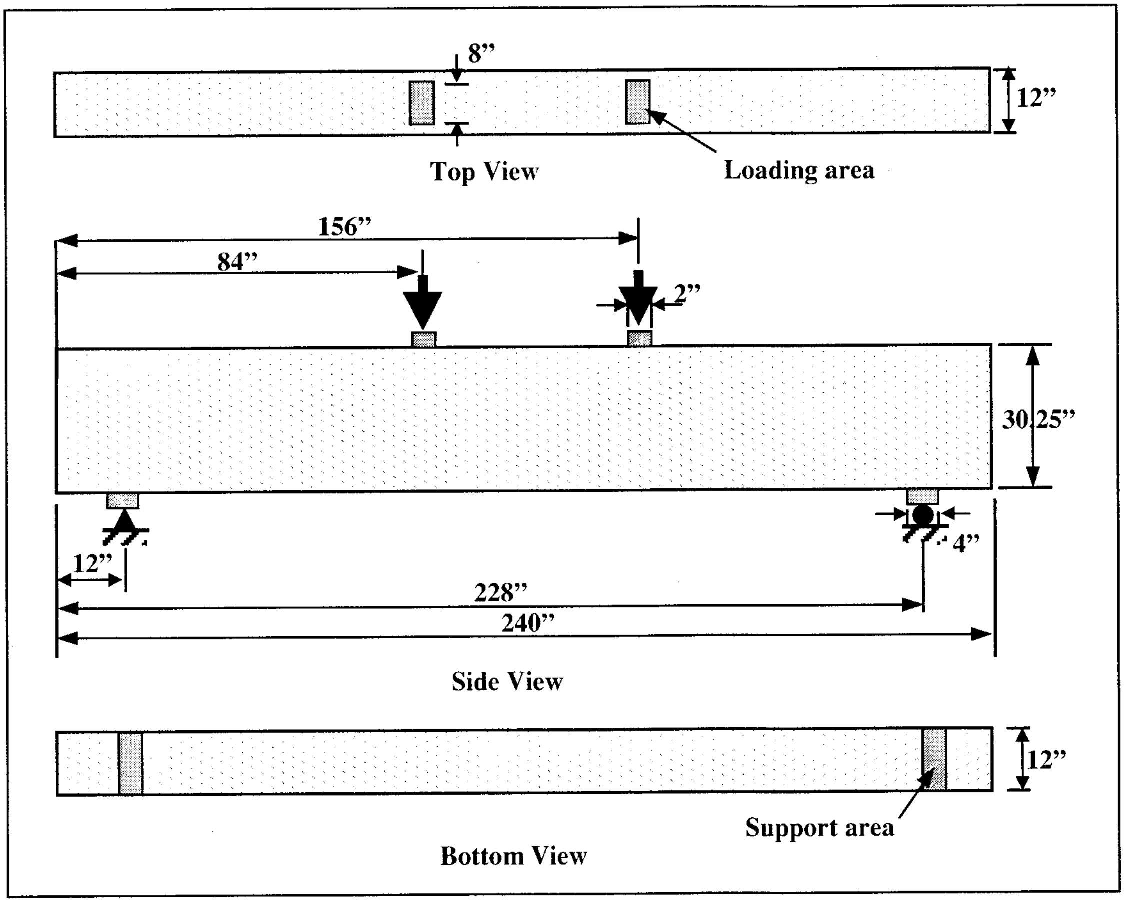

Figure 2.21: Loading and support locations (not to scale) (*McCurry and Kachlakev 2000*)

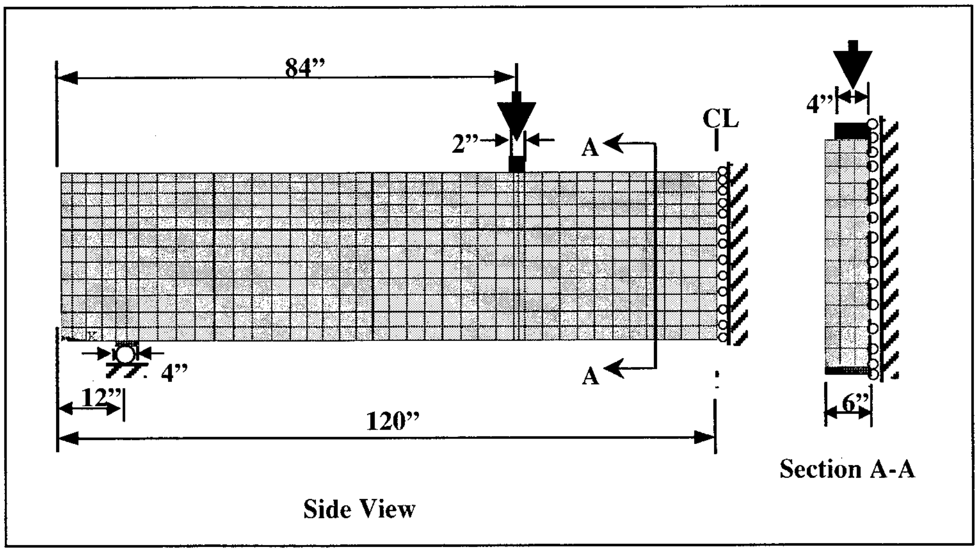

Figure 2.22: Steel plate with line support

Because a quarter of the entire beam was used for the model, planes of symmetry were required at the internal faces. At a plane of symmetry, the displacement in the direction perpendicular to the plane was held at zero. Figure 2.23 shows loading and boundary conditions for a typical finite element model. Rollers were used to show the symmetry condition at the internal faces.

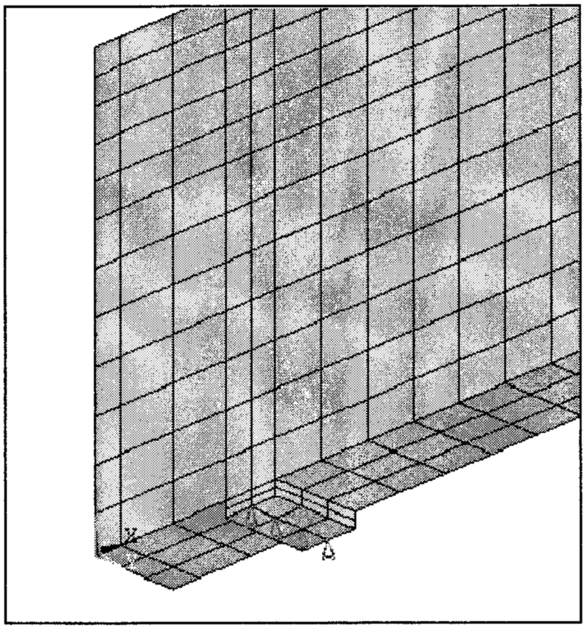

Figure 2.23: Loading and boundary conditions (not to scale)

When the loaded beam starts to displace downward, rotation of the plate should be permitted. Excessive cracking of the concrete elements above the steel plate was found to develop if rotation of the steel plate was not permitted, as shown in Figure 2.24(a).

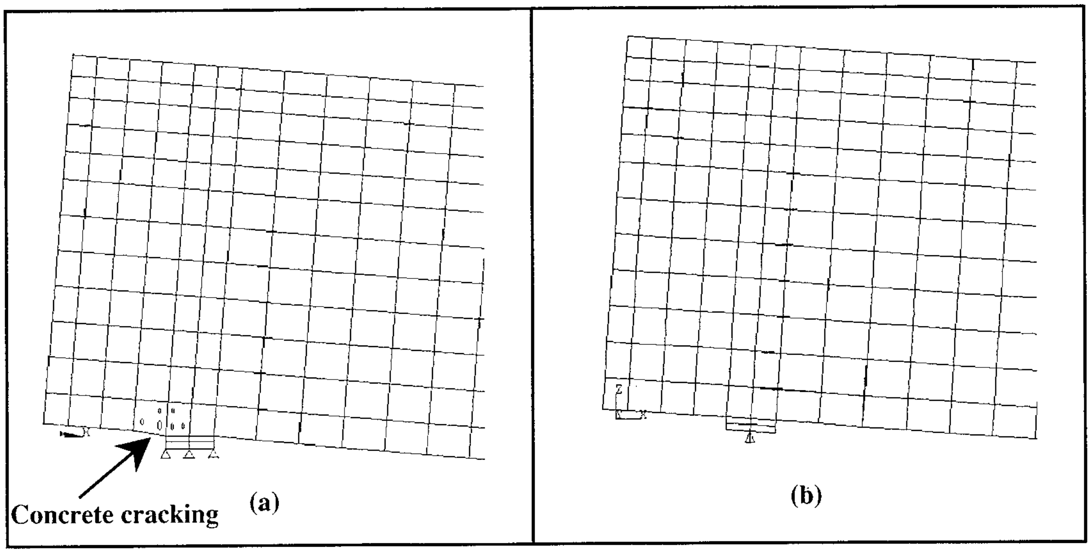

Figure 2.24: Displacements of model: (a) without rotation of steel plate (b) with rotation of steel plate

2.7 NONLINEAR SOLUTION

In nonlinear analysis, the total load applied to a finite element model is divided into a series of load increments called load steps. At the completion of each incremental solution, the stiffness matrix of the model is adjusted to reflect nonlinear changes in structural stiffness before proceeding to the next load increment. The ANSYS program (*ANSYS 1998*) uses Newton-Raphson equilibrium iterations for updating the model stiffness.

Newton-Raphson equilibrium iterations provide convergence at the end of each load increment within tolerance limits. Figure 2.25 shows the use of the Newton-Raphson approach in a single degree of freedom nonlinear analysis.

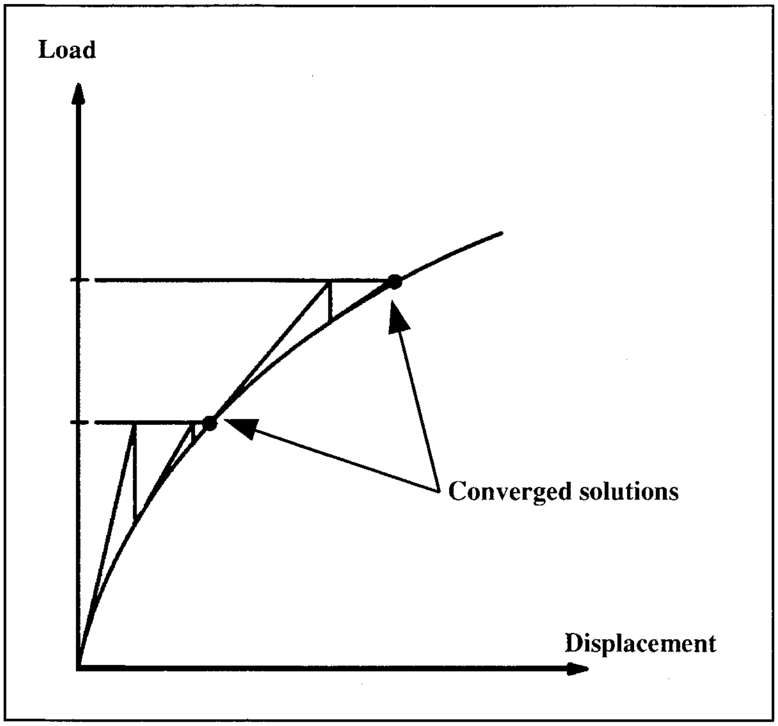

Figure 2.25: Newton-Raphson iterative solution (2 load increments) (*ANSYS 1998*)

Prior to each solution, the Newton-Raphson approach assesses the out-of-balance load vector, which is the difference between the restoring forces (the loads corresponding to the element stresses) and the applied loads. Subsequently, the program carries out a linear solution, using the out-of-balance loads, and checks for convergence. If convergence criteria are not satisfied, the out-of-balance load vector is re-evaluated, the stiffness matrix is updated, and a new solution is attained. This iterative procedure continues until the problem converges (*ANSYS 1998*).

In this study, for the reinforced concrete solid elements, convergence criteria were based on force and displacement, and the convergence tolerance limits were initially selected by the ANSYS program. It was found that convergence of solutions for the models was difficult to achieve due to the nonlinear behavior of reinforced concrete. Therefore, the convergence tolerance limits were increased to a maximum of 5 times the default tolerance limits (0.5% for force checking and 5% for displacement checking) in order to obtain convergence of the solutions.

2.7.1 Load Stepping and Failure Definition for FE Models

For the nonlinear analysis, automatic time stepping in the ANSYS program predicts and controls load step sizes. Based on the previous solution history and the physics of the models, if the convergence behavior is smooth, automatic time stepping will increase the load increment up to a selected maximum load step size. If the convergence behavior is abrupt, automatic time stepping will bisect the load increment until it is equal to a selected minimum load step size. The maximum and minimum load step sizes are required for the automatic time stepping.

In this study, the convergence behavior of the models depended on behavior of the reinforced concrete. The Flexure/Shear Beam model is used here as an example to demonstrate the load stepping. Figure 2.26 shows the load-deflection plot of the beam with four identified regions exhibiting different reinforced concrete behavior. The load step sizes were adjusted, depending upon the reinforced concrete behavior occurring in the model as shown in Table 2.4.

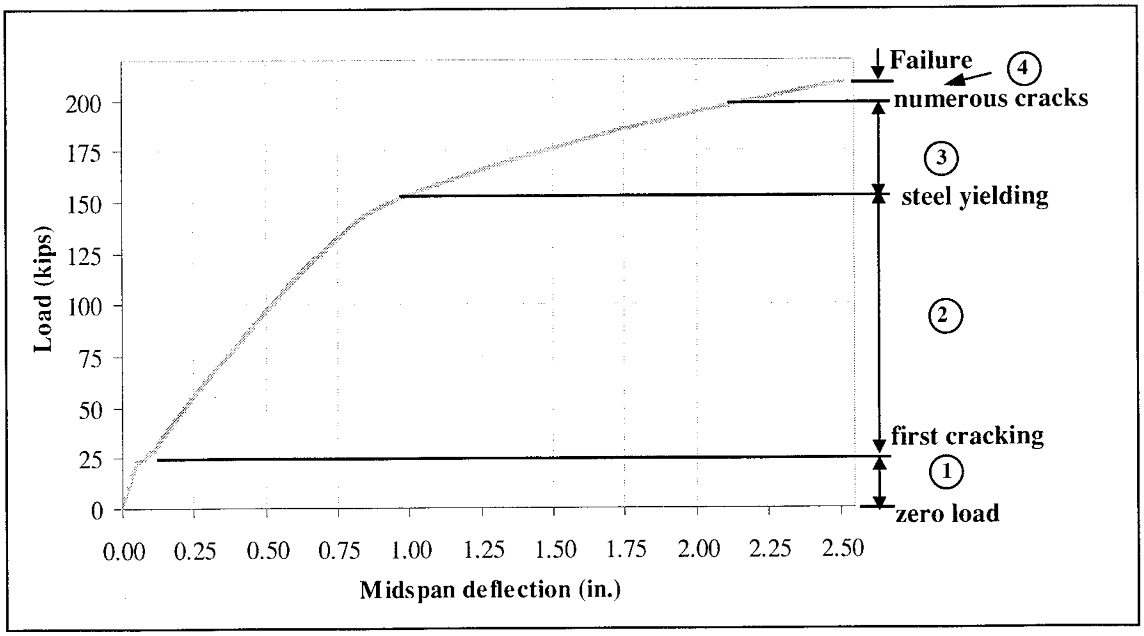

Figure 2.26: Reinforced concrete behavior in Flexure/Shear Beam

Table 2.4: Summary of load step sizes for Flexure/Shear Beam model

Reinforced concrete behavior	Load step sizes (lb)	
	Minimum	Maximum
1 Zero load – First cracking	1000	5000
2 First cracking – Steel yielding	2	75
3 Steel yielding – Numerous cracks	1	25
4 Numerous cracks – Failure	1	5

As shown in the table, the load step sizes do not need to be small in the linear range (Region **1**). At the beginning of Region **2**, cracking of the concrete starts to occur, so the loads are applied gradually with small load increments. A minimum load step size of 0.91 kg (2 lb) is defined for the automatic time stepping within this region. As first cracking occurs, the solution becomes difficult to converge. If a load applied on the model is not small enough, the automatic time stepping will bisect the load until it is equal to the minimum load step size. After the first cracking load, the solution becomes easier to converge. Therefore the automatic time stepping increases the load increment up to the defined maximum load step size, which is 34.05 kg (75 lb) for this region. If the load step size is too large, the solution either needs a large number of iterations to converge, which increases computational time considerably, or it diverges. In Region **3**, the solution becomes more difficult to converge due to yielding of the steel. Therefore, the maximum load step size is reduced to 11.35 kg (25 lb). A minimum load step size of 0.45 kg (1 lb) is defined to ensure that the solution will converge, even if a major crack occurs within this region. Lastly, for Region **4**, a large number of cracks occur as the applied load increases. The maximum load step size is defined to be 2.27 kg (5 lb), and a 0.45 kg (1 lb) load increment is specified for the minimum load step size for this region. For this study, a load step size of 0.45 kg (1 lb) is generally small enough to obtain converged solutions for the models.

Failure for each of the models is defined when the solution for a 0.45 kg (1 lb) load increment still does not converge. The program then gives a message specifying that the models have a significantly large deflection, exceeding the displacement limitation of the ANSYS program.

2.8 COMPUTATION RESOURCES

In this study, HP 735/125 workstations with a HP PA-7100 processor and 144MB of RAM were used. A disk-space up to 1 GB was required for the analysis of each full-scale beam. Computation time required up to 120 hours.

3.0 RESULTS FROM FINITE ELEMENT ANALYSIS OF FULL-SIZE BEAMS

This chapter compares the results from the ANSYS finite element analyses with the experimental data for the four full-size beams (*McCurry and Kachlakev 2000*). The following comparisons are made: load-strain plots at selected locations; load-deflection plots at midspan; first cracking loads; loads at failure; and crack patterns at failure. Also discussed are the development of crack patterns for each beam and summaries of the maximum stresses occurring in the FRP composites for the finite element models. The data from the finite element analyses were collected at the same locations as the load tests for the full-size beams.

3.1 LOAD-STRAIN PLOTS

Conventional 60 mm (2.36 in) long resistive strain gauges were placed throughout the full-size beams on concrete surfaces, FRP surfaces, and inside the beams on the main steel reinforcing bars at midspan. The locations of selected strain gauges used to compare with the finite element results are shown in Figure 3.1.

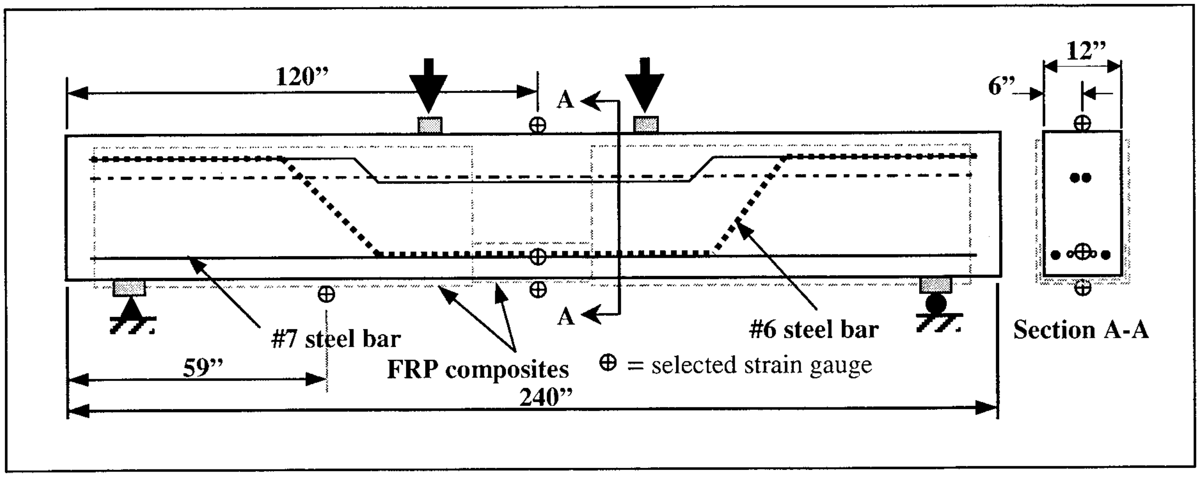

Figure 3.1: Selected strain gauge locations (not to scale)

3.1.1 Tensile Strain in Main Steel Reinforcing

For the Control, Flexure, and Shear Beams, experimental strain data were collected from strain gauges on the No.7 steel rebar at the midspan. For the Flexure/Shear Beam, strain data were collected from a strain gauge on the No.6 steel rebar at midspan. Locations of the strain gauges are shown in Figure 3.1. Comparisons of the load-tensile strain plots from the finite element analyses with the experimental data for the main steel reinforcing at midspan for each beam are shown in Figures 3.2 - 3.5. Note that the vertical axis shown in the figures represents the total load on the beams.

Figure 3.2 shows that before the strain reverses in the Control Beam, the trends of the finite element and the experimental results are similar. Especially in the linear range the strains from the finite element analysis correlate well with those from the experimental data. The finite element model then has lower strains than the experimental beam at the same load. The reversing strain in the experimental beam is possibly due to a local effect caused by the major cracks, which take place close to the midspan. This behavior does not occur in the finite element model with a smeared cracking approach. Finally, the steel at midspan in the finite element model and the actual beam does not yield prior to failure.

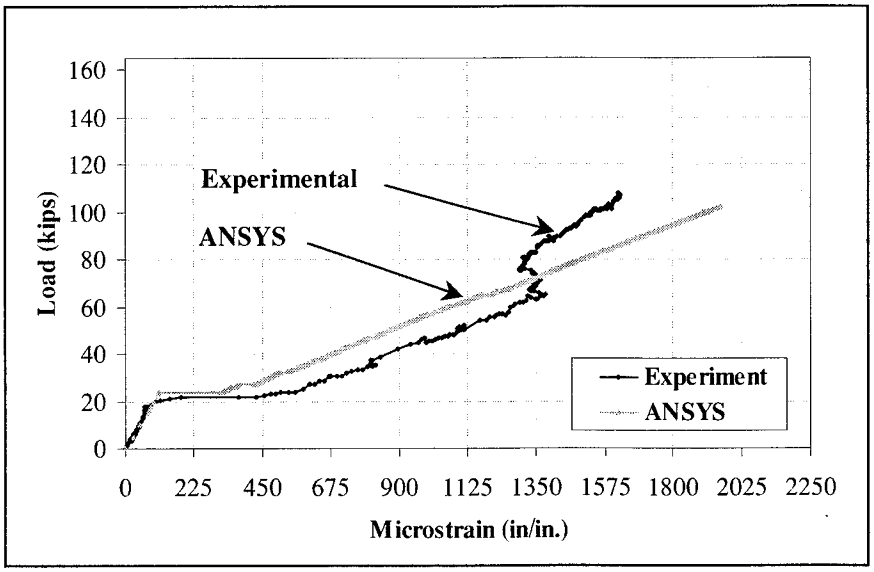

Figure 3.2: Load-tensile strain plot for #7 steel rebar in Control Beam

Figure 3.3 shows good agreement for the strains from the finite element analysis and the experimental results for the Flexure Beam up to 489 kN (110 kips). The finite element model for the Flexure Beam then has higher strains than the experimental results at the same load. At 489 kN (110 kips), the strain in the beam reverses. The steel yields at an applied load of 614 kN (138 kips) for the model, whereas the steel in the experimental beam has not yielded at failure of the beam.

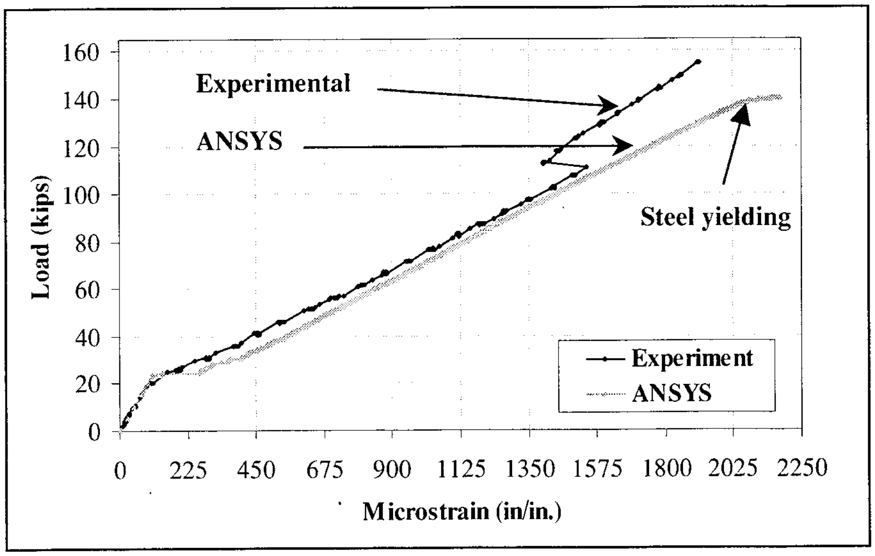

Figure 3.3: Load-tensile strain plot for #7 steel rebar in Flexure Beam

Figure 3.4 shows that the strain data from the finite element analysis and the experimental data for the Shear Beam have similar trends. Similar to the plots of strains in the steel for the Flexure Beam, the finite element model for the Shear Beam has higher strains than the experimental results at the same load. The steel in the finite element model yields at an applied load of 480 kN (108 kips), whereas the steel in the actual beam yields at approximately 560 kN (126 kips), a difference of 14%.

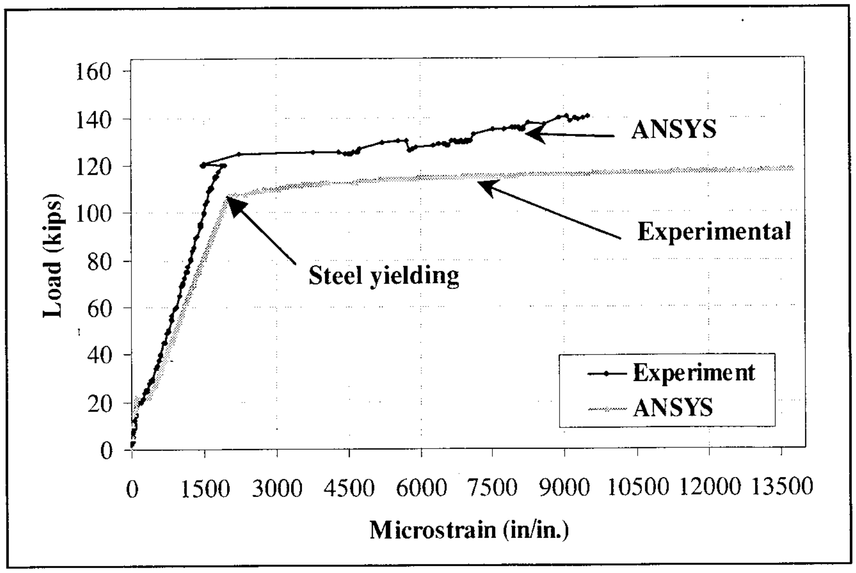

Figure 3.4: Load-tensile strain plot for #7 steel rebar in Shear Beam

Figure 3.5 shows that the strains calculated by ANSYS agree well with those from the experimental results for the Flexure/Shear Beam. Similar to the Control, Flexure and Shear Beams, the strains for the Flexure/Shear Beam from the finite element analysis correlate well with those from the experimental data in the linear range. Loading of the beam stopped at 712 kN (160 kips) due to limitations in the capacity of the testing machine. Based on the model, the steel in the beam yields before failure, which supports calculations reported for the testing (*McCurry and Kachlakev 2000*).

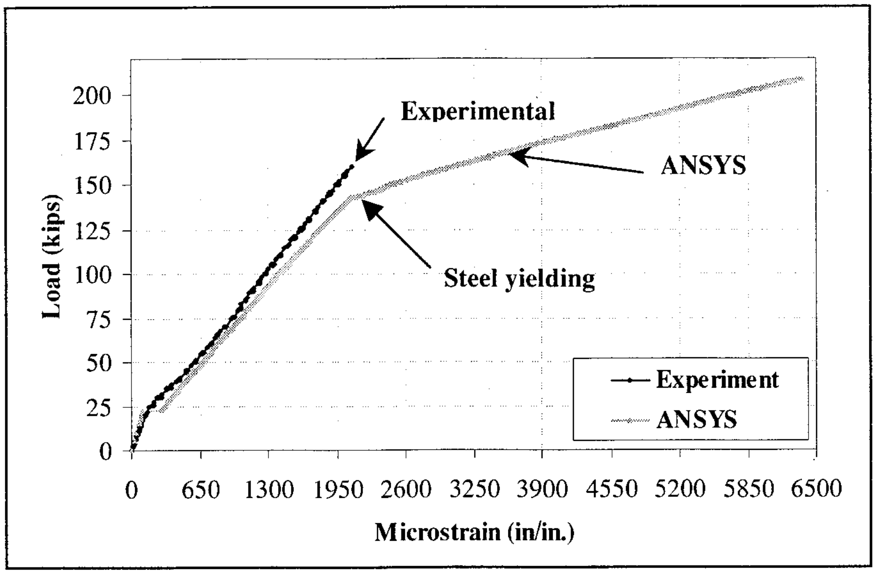

Figure 3.5: Load-tensile strain plot for #6 steel rebar in Flexure/Shear Beam
(Beam did not fail during actual loading.)

In general, the plots of load versus tensile strains in the main steel reinforcing from the finite element analyses have similar trends to those from the experimental results. In the linear range, the strains calculated by the finite element program are nearly the same as those measured in the actual beams. However, after cracking of the concrete, an inconsistency occurs in the results of the finite element analyses and the experimental data. For the Control Beam, ANSYS predicts that the strains occurring in the steel are lower than those in the actual beam, while the predicted strains for the other three models are higher than those in the actual beams.

In a reinforced concrete beam at a sufficiently high load, the concrete fails to resist tensile stresses only where the cracks are located as shown in Figure 3.6(a). Between the cracks, the concrete resists moderate amounts of tension introduced by bond stresses acting along the interface in the direction shown in Figure 3.6(b). This reduces the tensile force in the steel, as illustrated by Figure 3.6(d) (*Nilson 1997*).

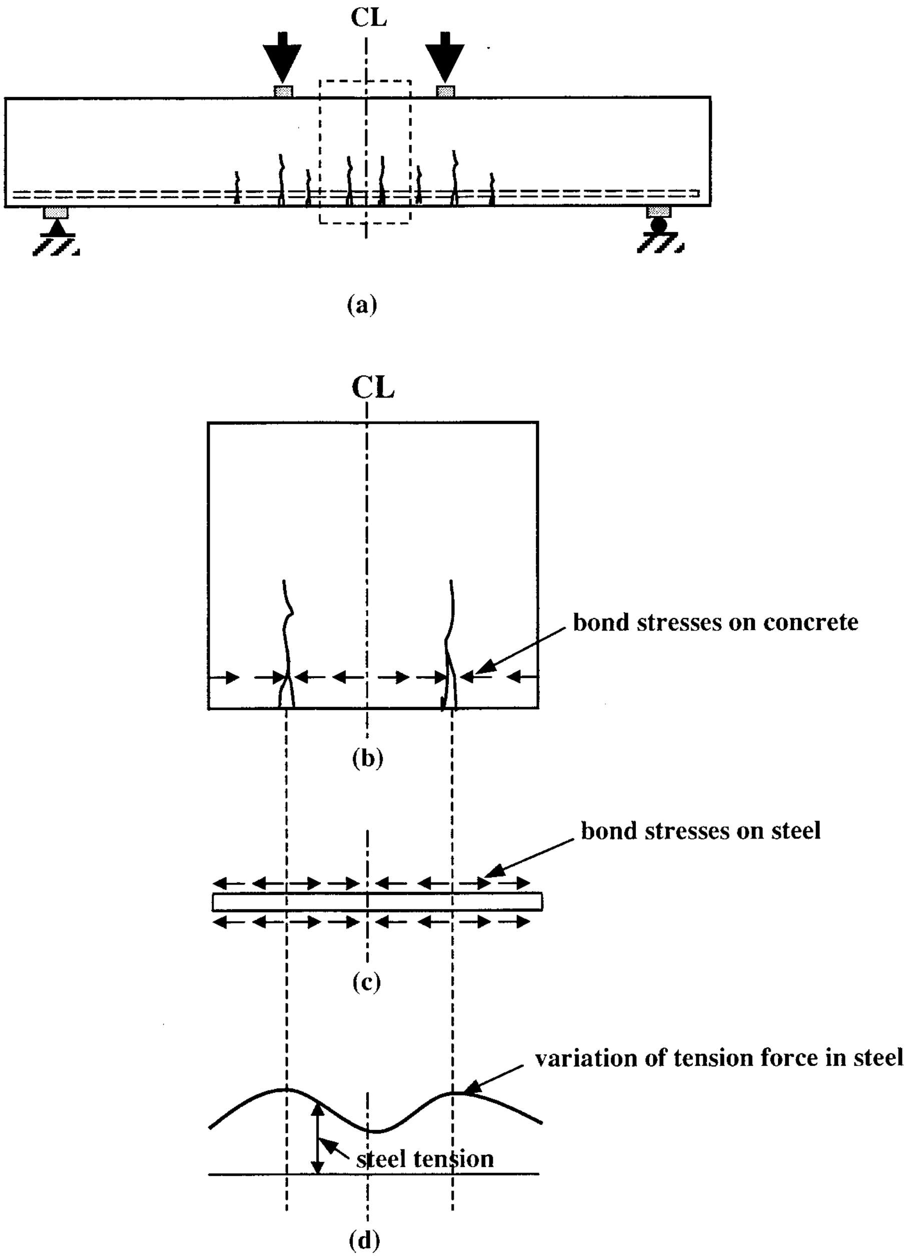

Figure 3.6: Variation of tensile force in steel for reinforced Concrete Beam: (a) typical cracking; (b) cracked concrete section; (c) bond stresses acting on reinforcing bar; (d) variation of tensile force in steel (*Nilson 1997*)

Generally, strains in the steel reinforcement for the finite element models were higher than those for the experimental beams after cracking of the concrete. Figure 3.7 shows the development of the tensile force in the steel for the finite element models. In the smeared cracking approach, the smeared cracks spread over the region where the principal tensile stresses in the concrete elements exceed the ultimate tensile strength, as shown in Figures 3.7(a) and 3.7(b), rather than having discrete cracks. The stiffness of the cracked concrete elements in the finite element model reduces to zero, so they cannot resist tension. Therefore, the tension in the steel elements for the finite element model does not vary as in the actual beam. The tensile force in a steel element is constant across the element (Figure 3.7(c)). For this reason, strains from the finite element analyses could be higher than measured strains. This could also explain the difference in the steel yielding loads between the finite element model and the experimental results for the Flexure and Shear Beams, as shown in Figures 3.3 and 3.4, respectively.

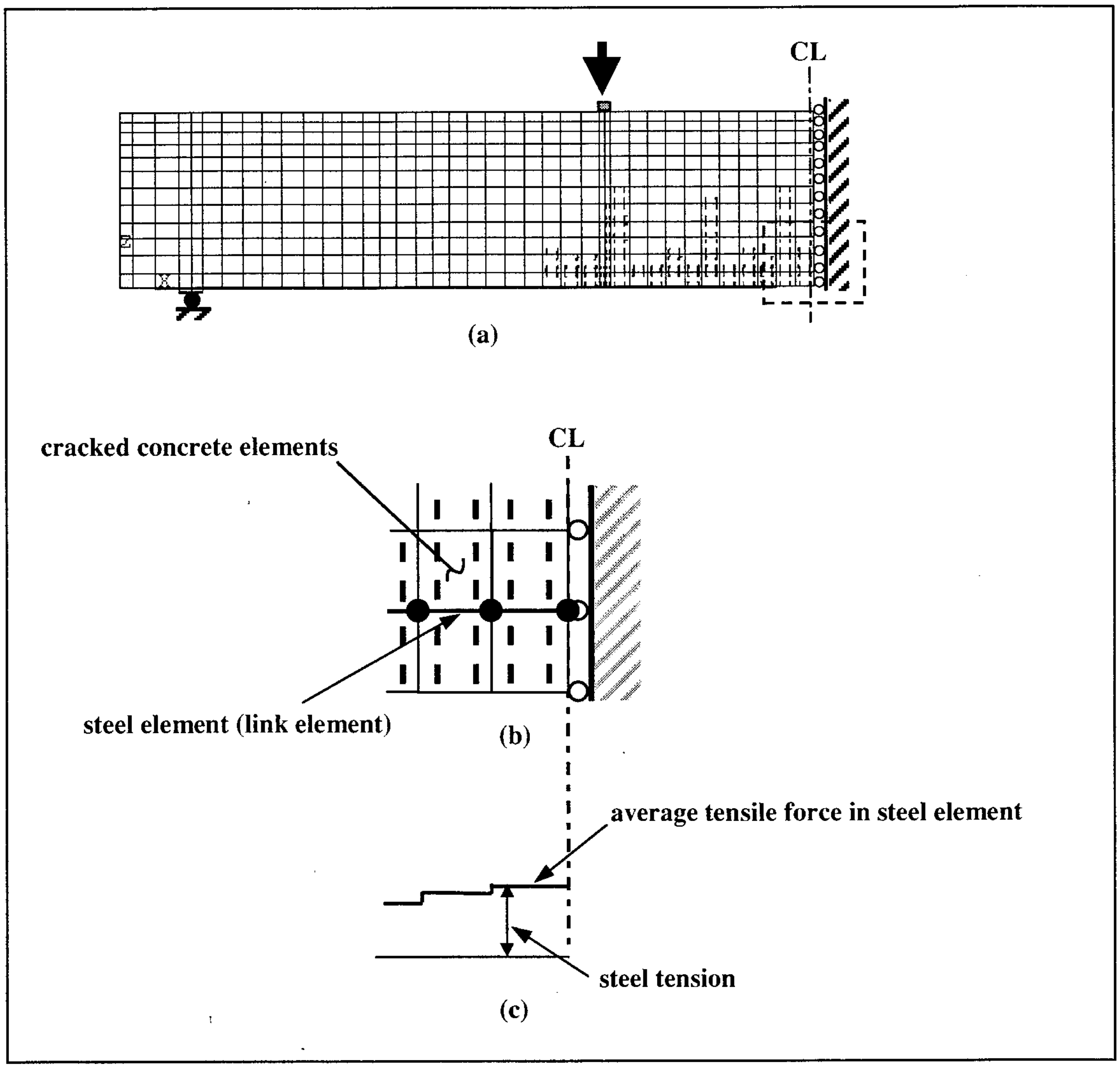

Figure 3.7: Development of tensile force in the steel for finite element models: (a) typical smeared cracking; (b) cracked concrete and steel rebar elements; (c) profile of tensile force in steel elements

The inconsistency in the strain of the Control Beam between the model and the experimental results could be due to cracks in close proximity to the strain gauge. A crack could create additional tensile strains. For the beams with FRP reinforcement, the composite would provide some constraint of the crack and therefore, less strain in the immediate vicinity of the crack.

Finally, improved results for the finite element model predictions could be obtained from a more complete characterization of the material properties of the concrete and the steel. Characterization of the concrete could be achieved by testing core samples from the beams. Characterization of the steel could be achieved by testing tension coupons of the steel reinforcing bars to determine the actual stress-strain behavior and yield strength rather than using design properties and an elastic-plastic model. For example, limited testing of tension coupons by ODOT indicated that the yield stress ranged from 460 to 520 MPa (66 to 75 ksi) compared to the nominal 410 MPa (60 ksi) used in the model.

3.1.2 Tensile Strain in FRP Composites

The locations of the strain gauges on the FRP reinforcing are shown in Figure 3.1. For the flexure and Flexure/Shear Beams, actual strain data were collected at the bottom of the beam at midspan on the surface of the CFRP composite. For the Shear Beam, the strains were measured at the bottom of the beam 1500 mm (59 in) from the end of the beam on the surface of the GFRP composite. Comparisons of the load-tensile strain plots from the finite element analyses with the experimental data for the FRP-strengthened beams are shown in Figures 3.8 - 3.10.

Figure 3.8 shows good agreement for the CFRP strains from the finite element analysis and the experimental results for the Flexure Beam. The model, however, consistently shows somewhat higher strains than the experimental results at the same load. This trend is similar to what was observed for the steel strain in the Flexure Beam.

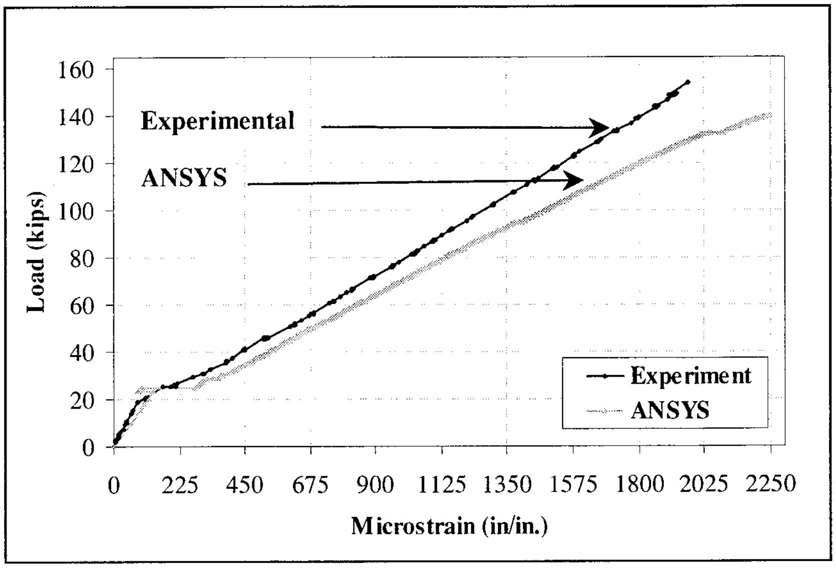

Figure 3.8: Load versus tensile strain in the CFRP for the Flexure Beam

Figure 3.9 shows that the GFRP strain data from the finite element analysis and the experimental data for the Shear Beam have similar trends initially. Similar to the Flexure Beam, the strains calculated by the finite element analysis for the Shear Beam are higher than those for the experimental results at the same load. After 222 kN (50 kips), however, the difference in strains between the finite element model and the experimental results increases more dramatically.

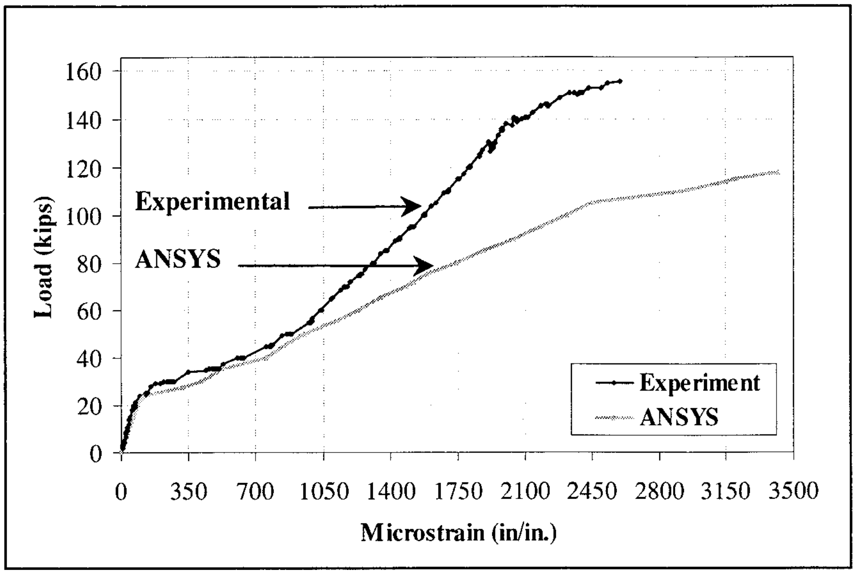

Figure 3.9: Load versus tensile strain in the GFRP for the Shear Beam

Figure 3.10 shows that the CFRP strain data from the finite element analysis and the experimental data for the Flexure/Shear Beam are in good agreement up to 712 kN (160 kips). The strains from the finite element model are again somewhat higher than the strains in the actual beam.

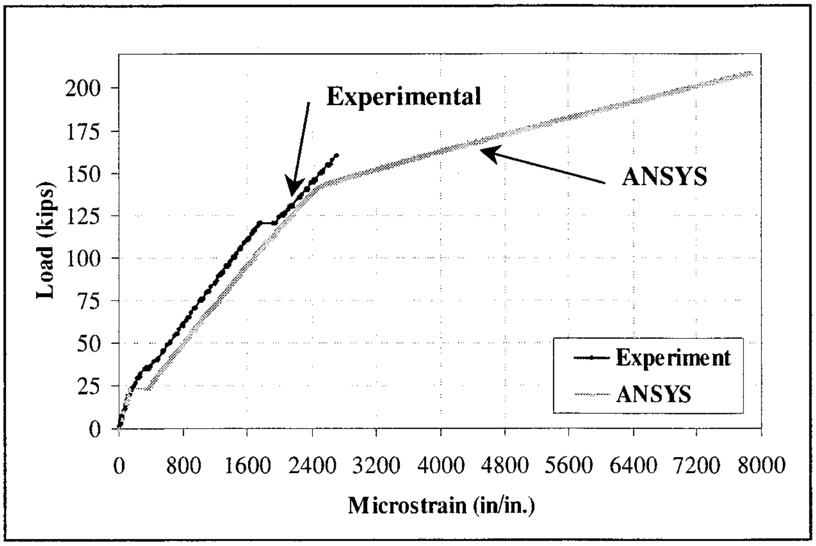

Figure 3.10: Load versus tensile strain in the CFRP for the Flexure/Shear Beam (Actual beam did not fail)

3.1.3 Compressive Strain in Concrete

The compressive strain data for concrete collected from the beam are compared with results from the finite element analysis. A strain gauge was placed at midspan on the top face of all four beams as shown in Figure 3.1. Figures 3.11 - 3.14 are comparisons of the load-compressive strain plots for all four beams.

Figure 3.11 shows that the load-compressive strain plots for the concrete from the finite element analysis and the experimental data have excellent agreement in the Control Beam. Figure 3.12 shows that the load-compressive strain plots for the Flexure Beam have a similar trend; however, strains in the concrete calculated by ANSYS are higher than those from the experimental results at the same load.

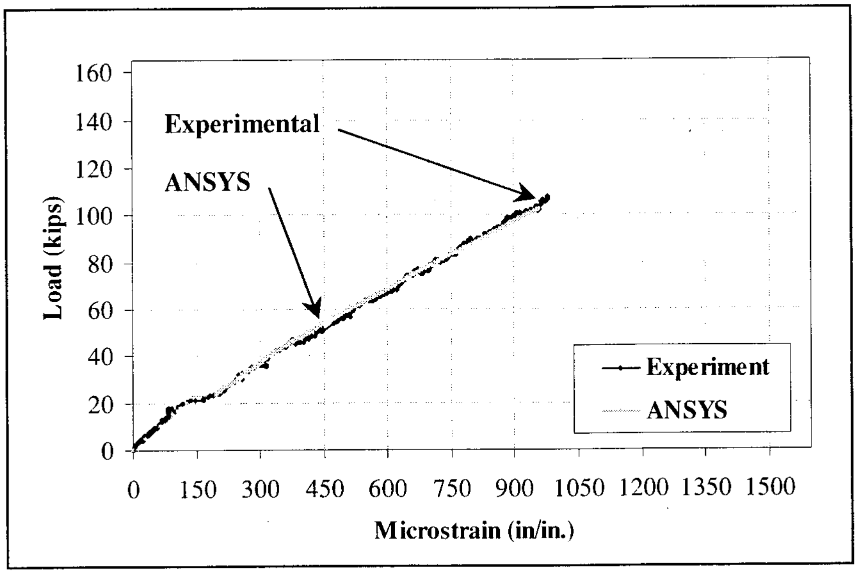

Figure 3.11: Load-compressive strain plot for concrete in Control Beam

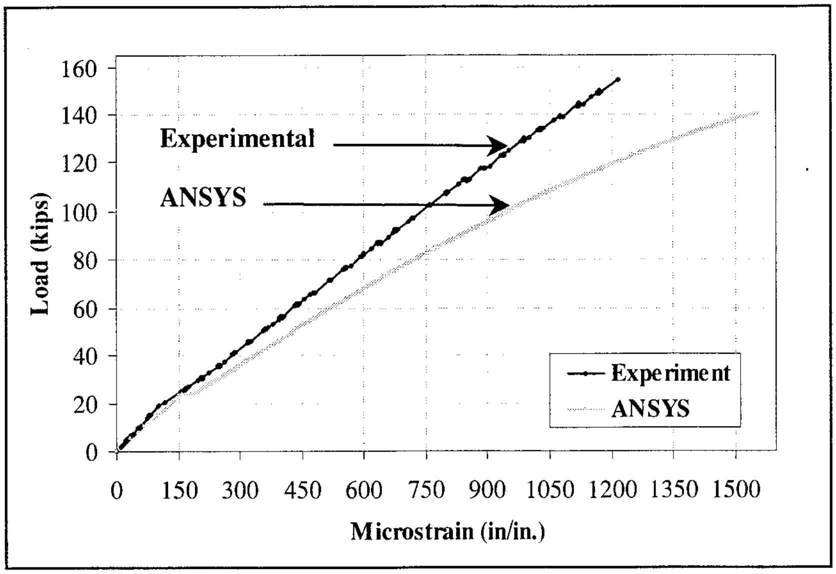

Figure 3.12: Load-compressive strain plot for concrete in Flexure Beam

Figure 3.13 shows the load-compressive strain plots for the Shear Beam. For applied loads from 0 to 467 kN (0 to 105 kips), the load-strain plots from the finite element model and the experimental results do not correlate well. As shown in the Figure, the experimental beam exhibits nonlinear behavior. This behavior should not happen at this load level. Either erroneous test data or local material imperfections may have caused the behavior. For example, cracks may be occurring at the interfaces between the cement and aggregate, due to their differences in elastic modulus, thermal coefficient of expansion, and response to change in moisture content when the concrete is hardened. At about 489 kN (110 kips), large strains occur for the finite element model, whereas at a load of 534 kN (120 kips) similar behavior takes place for the actual beam. These loads are close to the yielding loads of the steel, as shown in Figure 3.4. The yielding of the steel explains the large concrete strains.

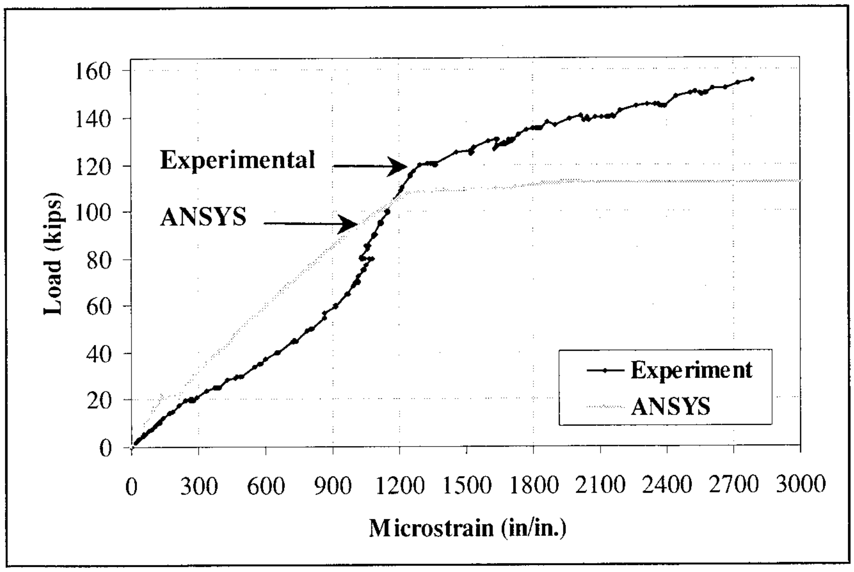

Figure 3.13: Load-compressive strain plot for concrete in Shear Beam

For the Flexure/Shear Beam, Figure 3.14, strains from the finite element model were consistently larger than strains from the actual beam. This behavior, which is also evident in the Flexure Beam, may be due to inaccuracy of the input materials properties for the model, as already discussed.

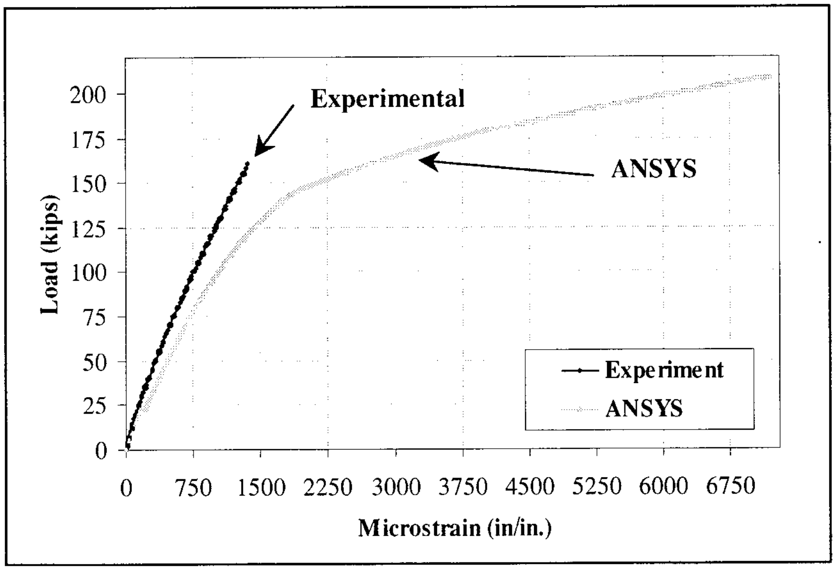

Figure 3.14: Load-compressive strain plot for concrete in Flexure/Shear Beam
(Actual beam did not fail.)

3.2 LOAD-DEFLECTION PLOTS

Direct current displacement transducers (DCDTs) were used to measure deflections for the experimental beams at midspan at the center of the bottom face of the beams. For ANSYS, deflections are measured at the same location as for the experimental beams. Figures 3.15 - 3.18 show the load-deflection plots from the finite element analyses and the experimental results for all four beams.

Figure 3.15 shows that the load-deflection plot from the finite element analysis agrees well with the experimental data for the Control Beam. In the linear range, the load-deflection plot from the finite element analysis is stiffer than that from the experimental results by approximately 66%. The first cracking load for the finite element analysis is 104.5 kN (23.5 kips), which is higher than the load of 78.3 kN (17.6 kips) from the experimental results by 34%. After first cracking, the finite element model is again stiffer than the actual beam by approximately 28%. At 400 kN (90 kips) for the model, yielding of the No.7 steel bar occurs at a location approximately 1800 mm (70 inches) from the end of the beam, resulting in the decreased stiffness. Lastly, the final load of 454 kN (102 kips) from the model is lower than the ultimate load of 476 kN (107 kips) from the experimental data by only 5%.

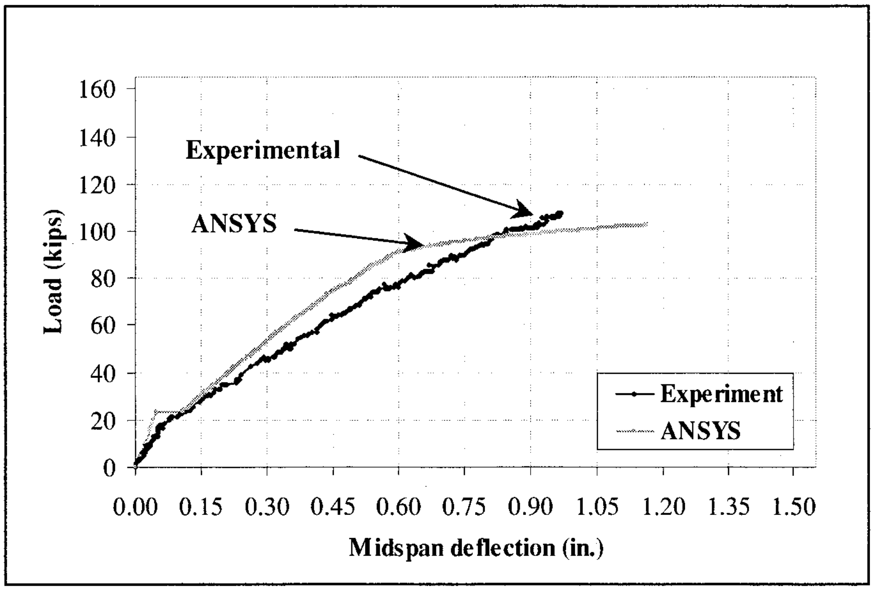

Figure 3.15: Load-deflection plot for Control Beam

Figure 3.16 shows that the load-deflection plots for the Flexure Beam from the experimental data and the finite element analysis are in reasonably good agreement. Similar to the Control Beam, the finite element model is stiffer than the actual beam in the linear range by approximately 55%. The finite element model cracks at 104.1 kN (23.4 kips), which is 8% higher than the actual beam load of 96.5 kN (21.7 kips). After first cracking, the two plots have a similar trend; however, the finite element model is again stiffer than the experimental beam by approximately

27%. The final load for the model is 623 kN (140 kips), which is less than the ultimate load of 689 kN (155 kips) for the actual beam by 10%.

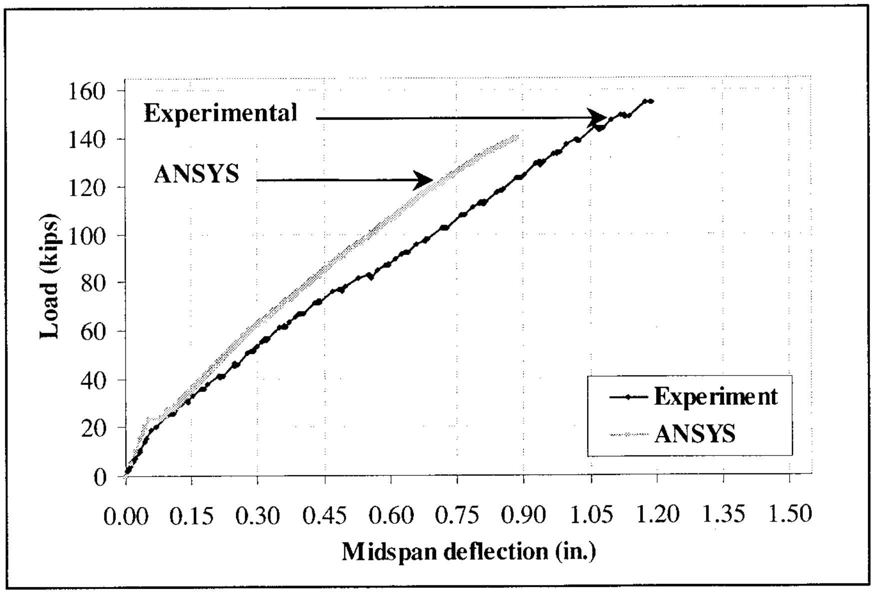

Figure 3.16: Load-deflection plot for Flexure Beam

As shown in Figure 3.17, the two load-deflection plots for the Shear Beam correlate well with each other. The finite element model is stiffer than the actual beam in the linear range by approximately 52%. The first cracking load for the finite element model is 96.1 kN (21.6 kips), which is higher than the load of 87.6 kN (19.7 kips) from the experimental results by 10%. After first cracking, the finite element model and the actual beam have almost the same stiffness. Large deflections begin to occur in the finite element model, however, at a load of 489 kN (110 kips), whereas the same behavior in the actual beam is observed at about 534 kN (120 kips). It is evident that the yielding of the steel reinforcement creates the large deflections. The final load for the finite element model is 525 kN (118 kips), which is less than the ultimate load of 689 kN (155 kips) for the experimental beam by 24%.

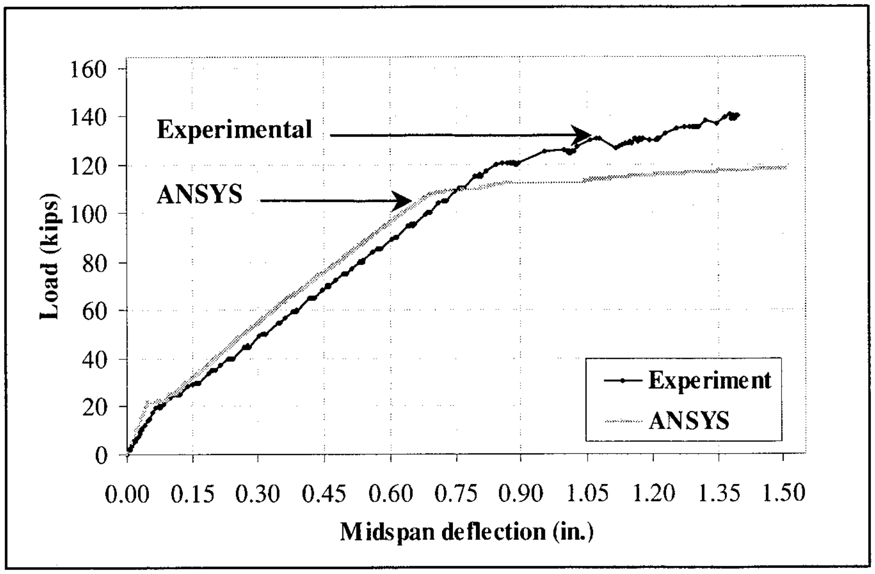

Figure 3.17: Load-deflection plot for Shear Beam

Figure 3.18 compares the two load-deflection plots for the Flexure/Shear Beam up to 712 kN (160 kips). The load-deflection plot from the finite element analysis agrees well with the experimental data. In the linear range, the load-deflection plot from the finite element analysis is slightly stiffer than that from the experimental results by about 12%. The first cracking load levels from the finite element analysis and the experimental results are 101.9 kN (22.9 kips) and 96.1 kN (21.6 kips), respectively, a difference of 6%. After cracking, the stiffness for the finite element model is slightly higher than the experimental data by approximately 14%. Above a load of 645 kN (145 kips), the stiffness of the finite element model decreases due to the yielding of the steel reinforcement in the beam model. The failure load in the model is 930 kN (209 kips).

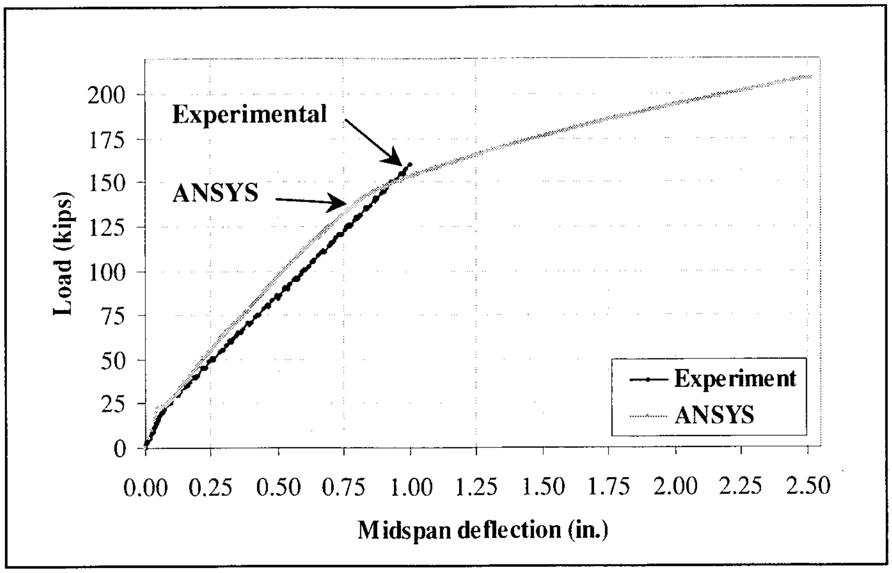

Figure 3.18: Load-deflection plot for Flexure/Shear Beam (Actual beam did not fail)

In general, the load-deflection plots for all four beams from the finite element analyses agree quite well with the experimental data. For the four beams, the finite element load-deflection plots in the linear range are stiffer than the experimental plots by 12% - 66%. The first cracking loads for all four models from the finite element analyses are higher than those from the experimental results by 6% - 34%. After first cracking, the stiffness of the finite element models is again higher than that of the experimental beams by 14% - 28%.

There are several factors that may cause the higher stiffness in the finite element models. Microcracks produced by drying shrinkage and handling are present in the concrete to some degree. These would reduce the stiffness of the actual beams, while the finite element models do not include microcracks. Perfect bond between the concrete and steel reinforcing is assumed in the finite element analyses, but the assumption would not be true for the actual beams. As bond slip occurs, the composite action between the concrete and steel reinforcing is lost. Thus, the overall stiffness of the actual beams could be lower than what the finite element models predict, due to factors that are not incorporated into the models.

Figure 3.19 illustrates the differences in load-deflection behavior for the four beams, and Figure 3.20 compares the four finite element models. Both figures show that the stiffness of the beams before and after applying FRP strengthening is approximately the same in the linear range. After first cracking, the stiffness of the FRP-strengthened beams from the finite element analyses is higher than that for the Control Beam, which is consistent with the experimental results.

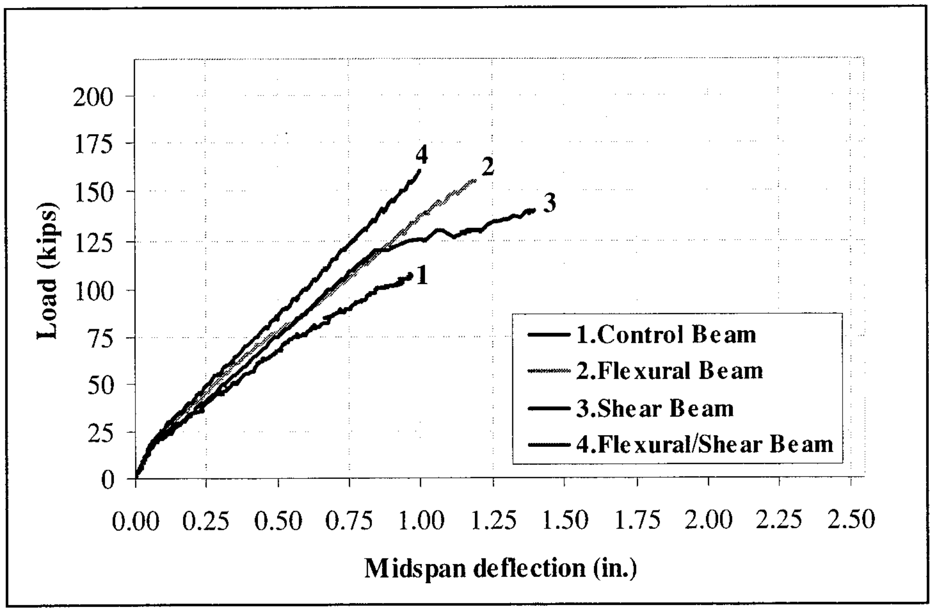

Figure 3.19: Load-deflection plots for the four beams based on measurements (Beam No.4 did not fail) (*Kachlakev and McCurry 2000*)

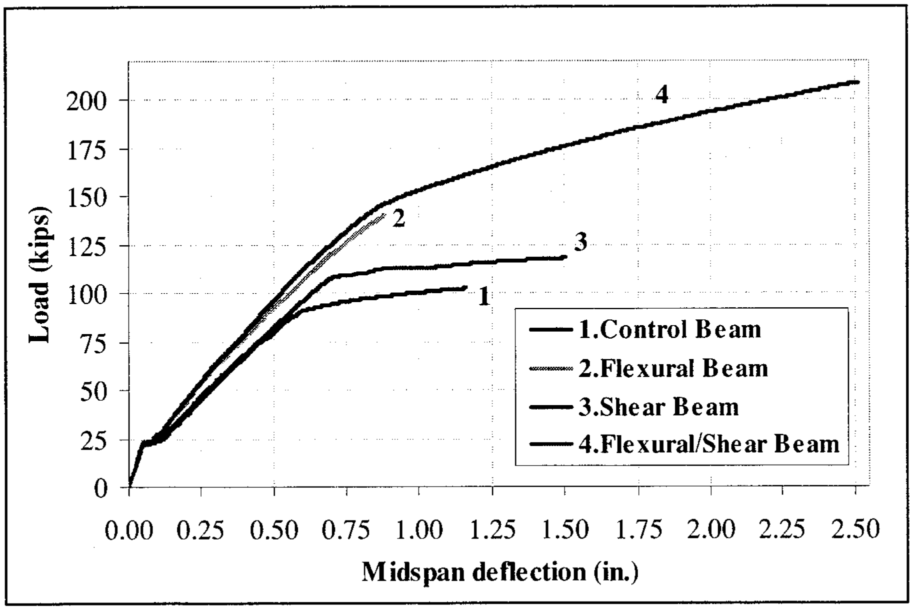

Figure 3.20: Load-deflection plots for the four beams based on ANSYS finite element models

For comparing the load-carrying capacity of the beams, the finite element models have the same sequence as the actual beams. For the finite element models, the Flexure, Shear, and Flexure/Shear strengthened beams have higher load carrying capacities than the Control Beam by 37%, 16%, and 105%, respectively. The experimental FRP-strengthened Flexure, Shear, and

Flexure/Shear Beams have capacities greater than the Control Beam by 45%, 45%, and 104%, respectively. Note that the capacity of the actual Flexure/Shear Beam was estimated from hand calculations (*Kachlakev and McCurry 2000*).

3.3 FIRST CRACKING LOADS

The first cracking load from the finite element analysis is the load step where the first signs of cracking occur for concrete in the model. Loads at first cracking from the model and the experimental results are compared in Table 3.1.

Table 3.1: Comparisons between experimental and ANSYS first cracking loads

Beam	**First cracking load (kips)**		**% Difference**
	Experimental*	**ANSYS**	
Control Beam	17.6	23.5	34
Flexure Beam	21.7	23.4	7.8
Shear Beam	19.7	21.6	9.6
Flexure/Shear Beam	21.6	22.9	6.0

*(*McCurry and Kachlakev 2000*)

The first cracking loads from the finite element analyses and the experimental data are within 10% for three of the conditions. In all cases, the first cracking load from ANSYS is higher than that from the experimental data. This is possibly due to the relative homogeneity of the finite element models when compared to the relative heterogeneity of the actual beams that contain a number of microcracks. The finite element results also support the experimental observation that after applying the FRP composites, the FRP reinforcing scheme for the Shear Beam results in the lowest first cracking load when compared to the other two FRP-strengthened beams.

3.4 EVOLUTION OF CRACK PATTERNS

In ANSYS, outputs, i.e., stresses and strains, are calculated at integration points of the concrete solid elements. Figure 3.21 shows integration points in a concrete solid element. A cracking sign represented by a circle appears when a principal tensile stress exceeds the ultimate tensile strength of the concrete. The cracking sign appears perpendicular to the direction of the principal stress as illustrated in Figure 3.22.

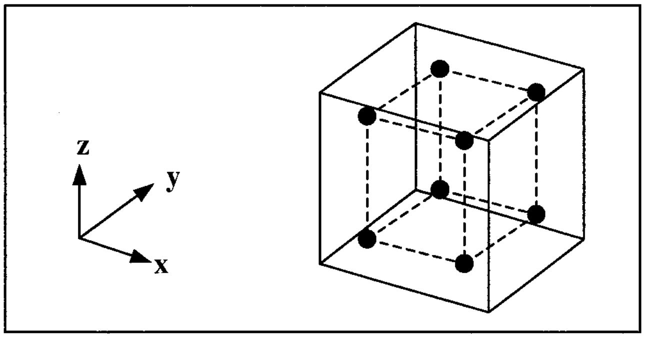

Figure 3.21: Integration points in concrete solid element (*ANSYS 1998*)

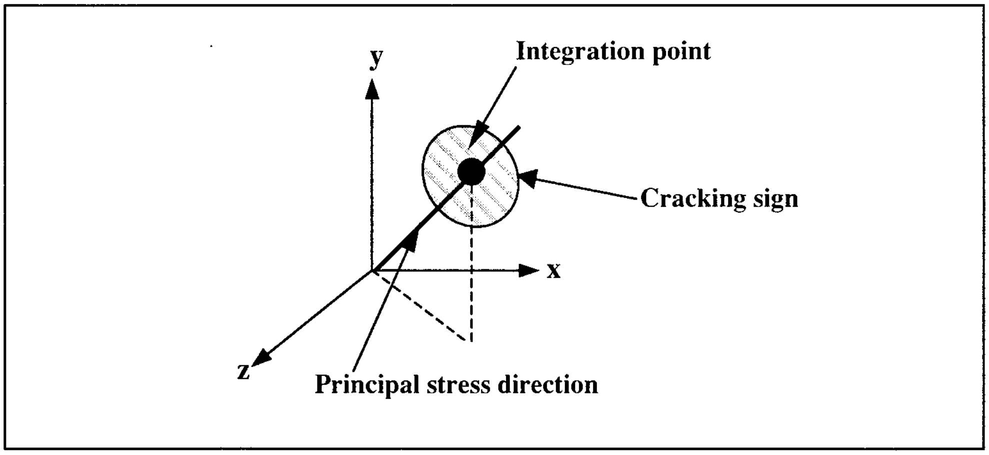

Figure 3.22: Cracking sign (*ANSYS 1998*)

Figure 3.23 shows the coordinate axes used in this finite element modeling study, where *x*, *y*, and *z* correspond to the length, width, and height directions for the beams, respectively.

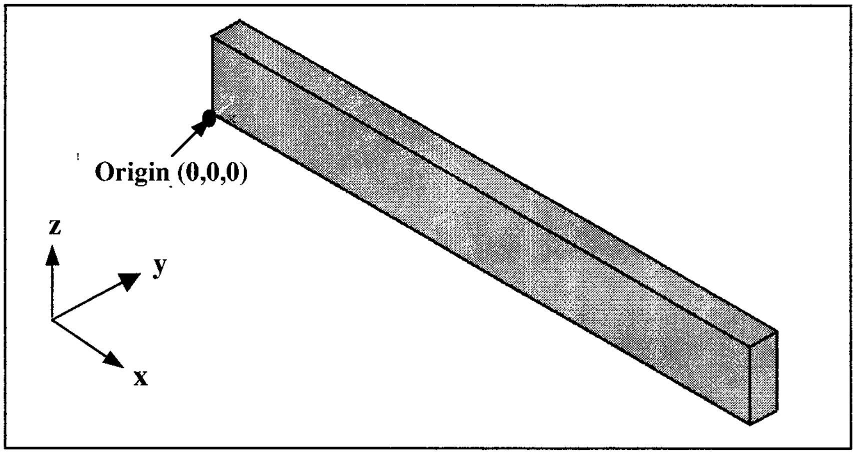

Figure 3.23: Coordinate system for finite element models

Figure 3.24 shows typical cracking signs in an ANSYS model. A side face of a quarter beam model is used to demonstrate. As shown in Figure 3.24(a), at the bottom of the beam at midspan, principal tensile stresses occur mostly in the x direction (longitudinally). When the principal stresses exceed the ultimate tensile strength of the concrete, circles as cracking signs appear perpendicular to the principal stresses in the x direction. Therefore the cracking signs shown in the figure appear as vertical straight lines occurring at the integration points of the concrete solid elements. Hereafter, these will be referred to as flexural cracks.

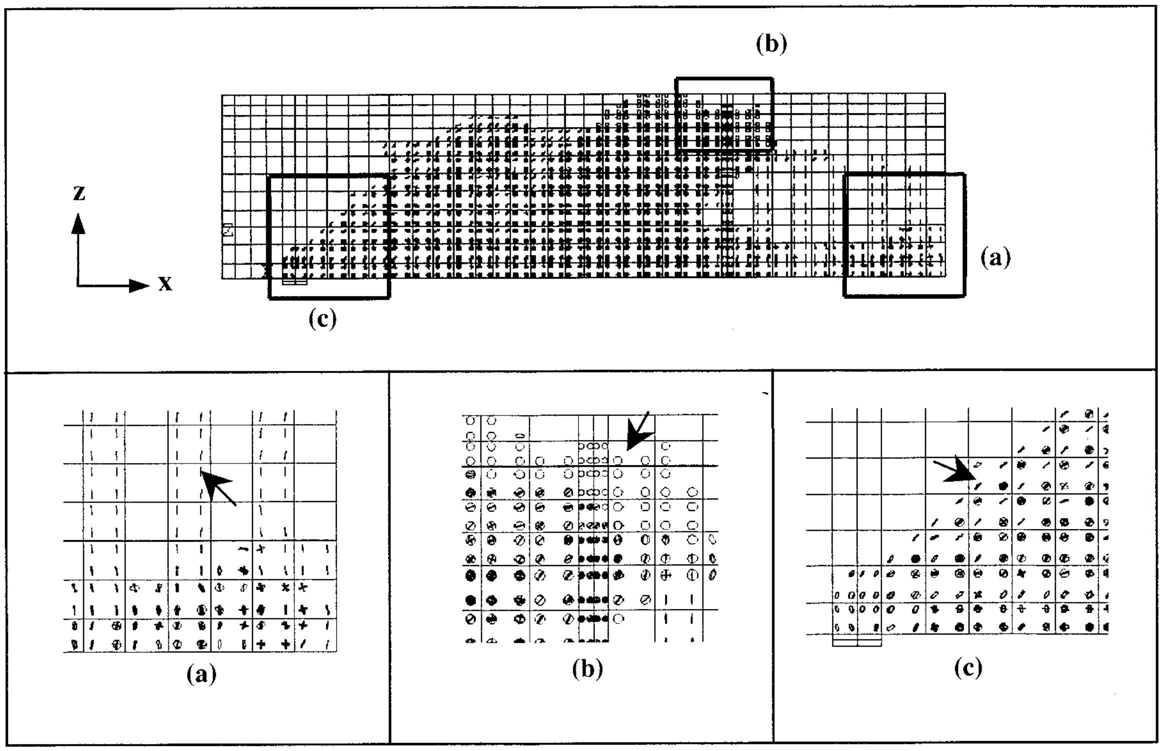

Figure 3.24: Typical cracking signs occurring in finite element models: (a) flexural cracks; (b) compressive cracks; (c) diagonal tensile cracks

Figure 3.24(b) shows the type of cracking signs observed for concrete elements underneath the loading locations. For a concrete structure subjected to uniaxial compression, cracks propagate primarily parallel to the direction of the applied compressive load, since the cracks result from tensile strains developed due to Poisson's effect (*Mindess and Young 1981; Shah, et al. 1995*). Similar behavior is seen in the finite element analysis. Loads in the z direction result in tensile strains in the y direction by Poisson's effect. Thus, circles appear perpendicular to the principal tensile strains in the y direction at integration points in the concrete elements near the loading location. These will be referred to as compressive cracks.

Figure 3.24(c) shows cracking signs where both normal and shear stresses act on concrete elements. By using transformation equations, directions and magnitudes of the principal stresses can be obtained (*Gere and Timoshenko 1997*). At the location shown in the Figure, normal tensile stresses generally develop in the *x* direction and shear stresses occur in the *xz* plane. Consequently, the direction of tensile principal stresses becomes inclined from the horizontal. Once the principal tensile stresses exceed the ultimate tensile strength of the concrete, inclined circles appearing as straight lines perpendicular to the directions of the principal stresses appear at integration points of the concrete elements. Hereafter, these will be referred to as diagonal tensile cracks.

The ANSYS program records a crack pattern at each applied load step. Figures 3.25 and 3.26 show the evolution of crack patterns for each beam. In general, flexural cracks occur early at midspan. When applied loads increase, vertical flexural cracks spread horizontally from the midspan to the support. At a higher applied load, diagonal tensile cracks appear. Increasing applied loads induces additional diagonal and flexural cracks. Finally, compressive cracks appear at nearly the last applied load steps. The cracks appear underneath the loading location on the Control and Flexure Beam models. For the Shear Beam model, there are no compressive cracks appearing underneath the loading location. On the Flexure/Shear Beam model, significant cracks appear at the top part of the beam. The appearance of the cracks defines the failure mode for the beams, which will be discussed in Section 3.6.

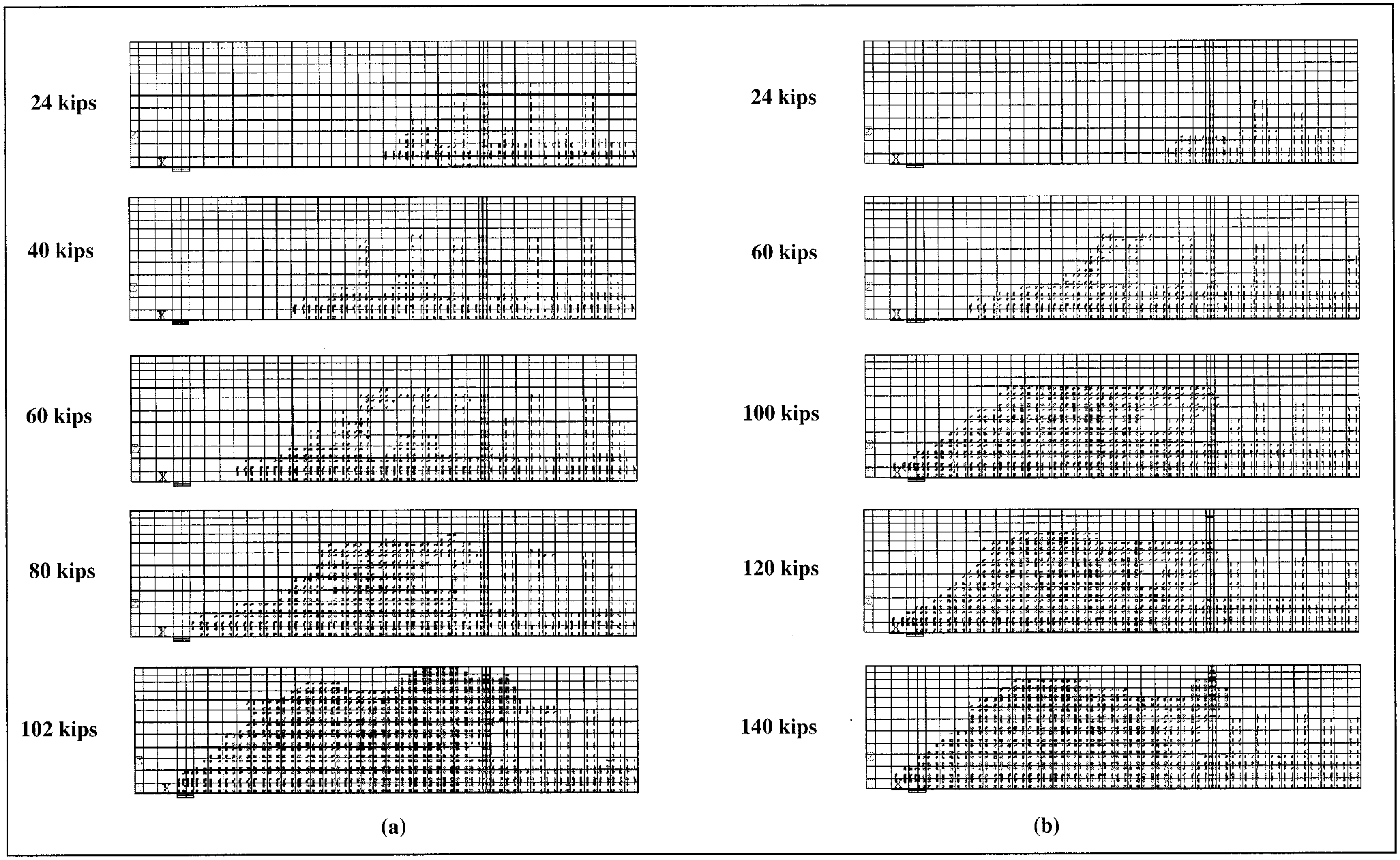

Figure 3.25: Evolution of crack patterns: (a) Control Beam; (b) Flexure Beam

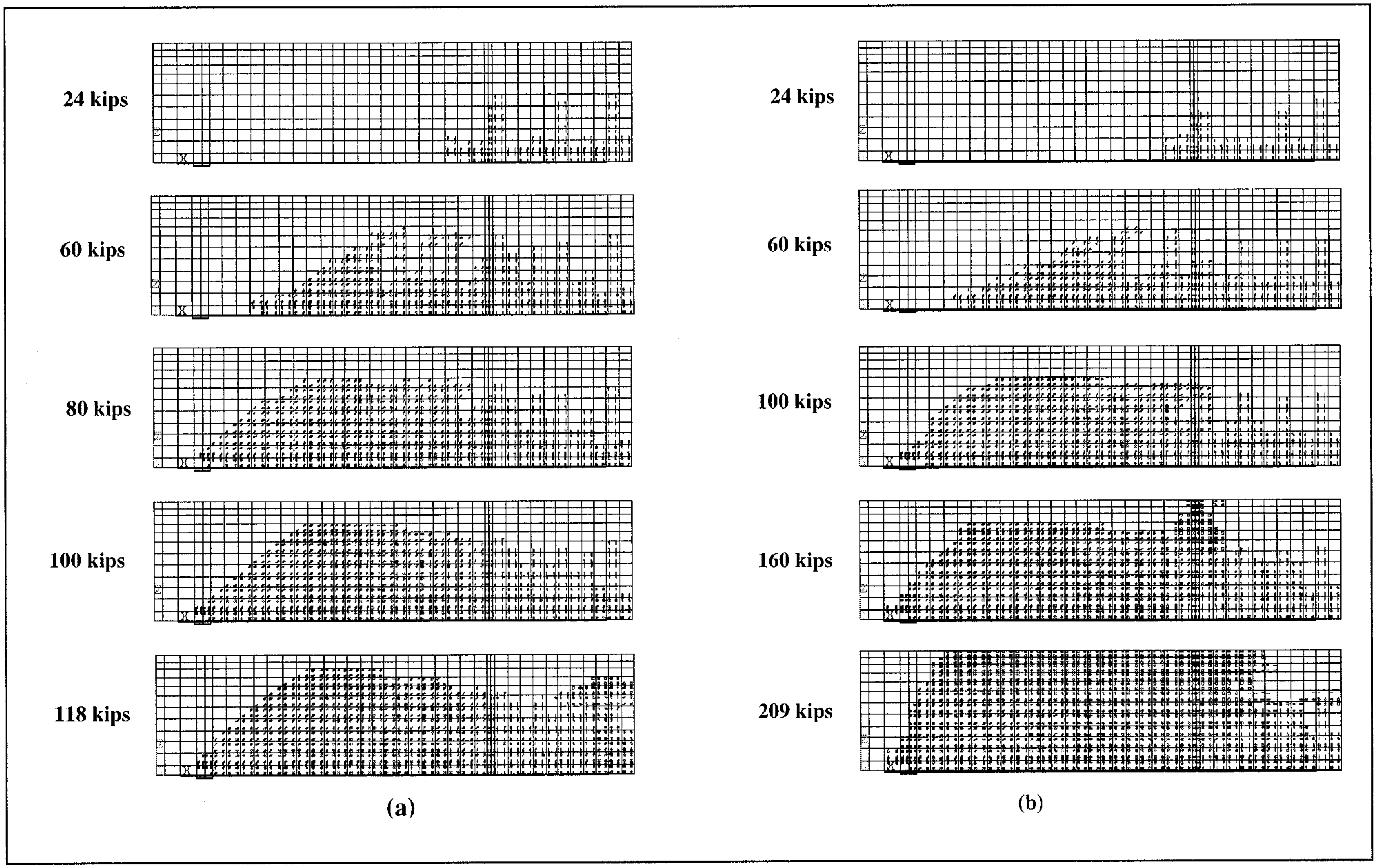

(a)

(b)

Figure 3.26: Evolution of crack patterns (Continued): (a) Shear Beam; (b) Flexure/Shear Beam

3.5 LOADS AT FAILURE

Table 3.2 compares the ultimate loads for the full-size beams and the final loads from the finite element simulations. ANSYS underestimates the strength of the beams by 5%-24%. One reason for the discrepancy is that the inclined portions of the steel reinforcement are excluded from the finite element models. Toughening mechanisms at the crack faces may also slightly extend the failures of the experimental beams before complete collapse. The finite element models do not have such mechanisms.

Table 3.2: Comparisons between experimental ultimate loads and ANSYS final loads

Beam	Ultimate load (kips) from Experimental results*	Final load (kips) from ANSYS	% Difference
Control beam	107	102	-5
Flexure Beam	155	140	-10
Shear beam	155	118	-24
Flexure/Shear beam	160**	209	N/A

*(*McCurry and Kachlakev 2000*)

**This is not an ultimate load. The testing was limited by the testing machine capacity.

Toughening mechanisms are illustrated in Figure 3.27 (*Shah, et al. 1995*). The grain bridging process, shown in Figure 3.27(a), occurs when the crack has advanced beyond an aggregate that continues to transmit stresses across the crack. Interlock between cracked faces, shown in Figure 3.27(b), can cause energy dissipation and load transfer through friction across the crack. A blunt crack tip, shown in Figure 3.27(c), requires additional energy for crack propagation than a sharp crack. Finally, Figure 3.27(d) shows crack branching due to concrete heterogeneities. Energy is consumed in creating the crack branches.

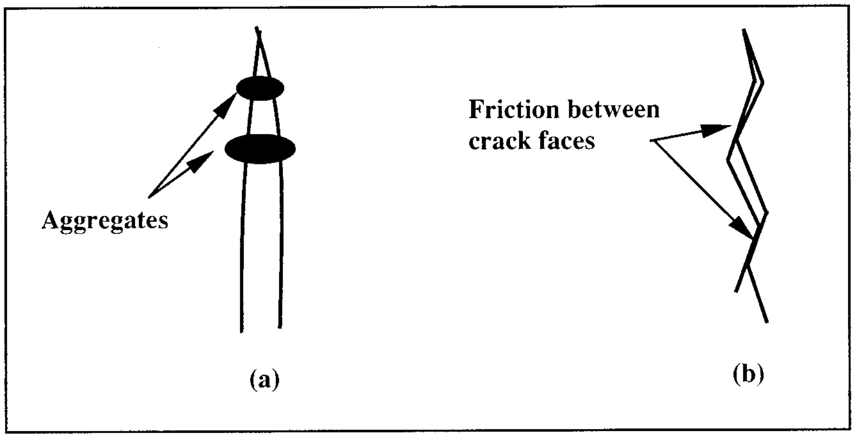

Figure 3.27: Toughening mechanisms: (a) aggregate bridging; (b) crack-face friction (*Shah, et al. 1995*)

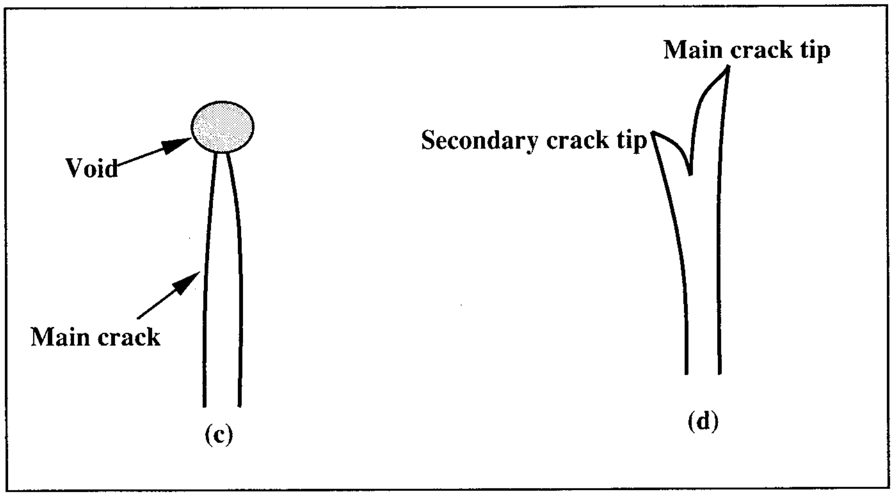

Figure 3.27 (continued): Toughening mechanisms: (c) crack tip blunted by void; (d) crack branching (*Shah, et al. 1995*)

The material properties assumed in this study may be imperfect. The stress-strain curve for the steel used for the finite element beam models should be obtained directly from material testing. The actual reinforcing steel has a different stress-strain curve when compared to the idealized steel used for the finite element modeling, as shown in Figure 3.28. Therefore, this may help to produce the higher ultimate load in the experimental beams. Moreover, the perfectly plastic stress-strain relationship for the concrete after the ultimate compressive stress might also cause the lower failure load in the finite element models.

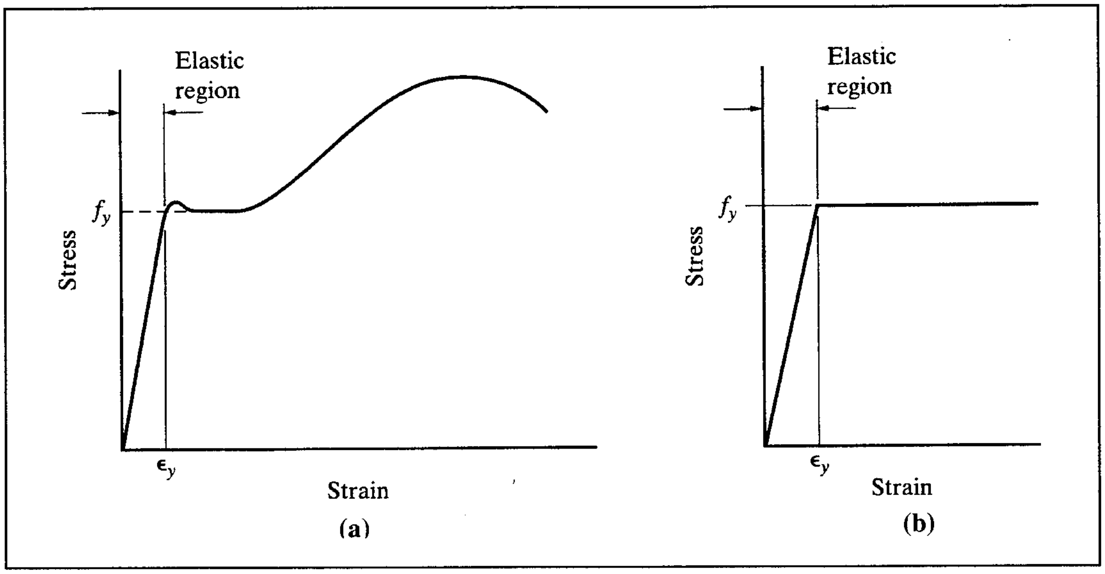

Figure 3.28: Stress-strain curve for reinforcing steel: (a) as determined by tension test; (b) idealized (*Spiegel and Limbrunner 1998*)

3.6 CRACK PATTERNS AT FAILURE

In testing the actual beams, the failure modes for the three beams that failed were as predicted. The Control and Flexure Beams failed in shear. The Shear Beam failed in flexure at the midspan, with yielding of the steel reinforcing followed by a compression failure at the top of the beam.

Crack patterns obtained from the finite element analyses at the last converged load steps are compared to failure photographs from the actual beams (Figures 3.29 and 3.30). For the Control Beam, Figure 3.29(a), the crack pattern from ANSYS and the actual beam agree very well. Diagonal tensile cracks propagate from the support toward the loading area. The cracks occur mostly in the high shear stress region. A similar pattern developed for the Flexure Beam and was simulated by ANSYS, as shown in Figure 3.29(b).

Figure 3.30(a) shows that numerous cracks occur at midspan of the finite element model. The crack pattern and steel yielding at the midspan (Figure 3.4) for the finite element Shear Beam support the experimental results that the beam fails in flexure. Note, however, that the crushing-related cracks observed at the top of the actual beam were not seen in the model because the crushing capability in ANSYS was turned off. Moreover, cracks appearing at the final load step at failure were not observable because of the diverged solution that defined the failure in the model.

Calculations suggested that the actual Flexure/Shear Beam would be limited by the crushing strength of the concrete and fail in flexure (*McCurry and Kachlakev 2000*). Figure 3.30(b) illustrates the final crack pattern for the beam predicted by the ANSYS program. Numerous compressive cracks occur at the top part of the beam, and many flexural cracks are observed at midspan as well. Moreover, the steel at the midspan in the model yields, as shown in Figure 3.5. These observations support the conclusion that the beam would fail in flexure.

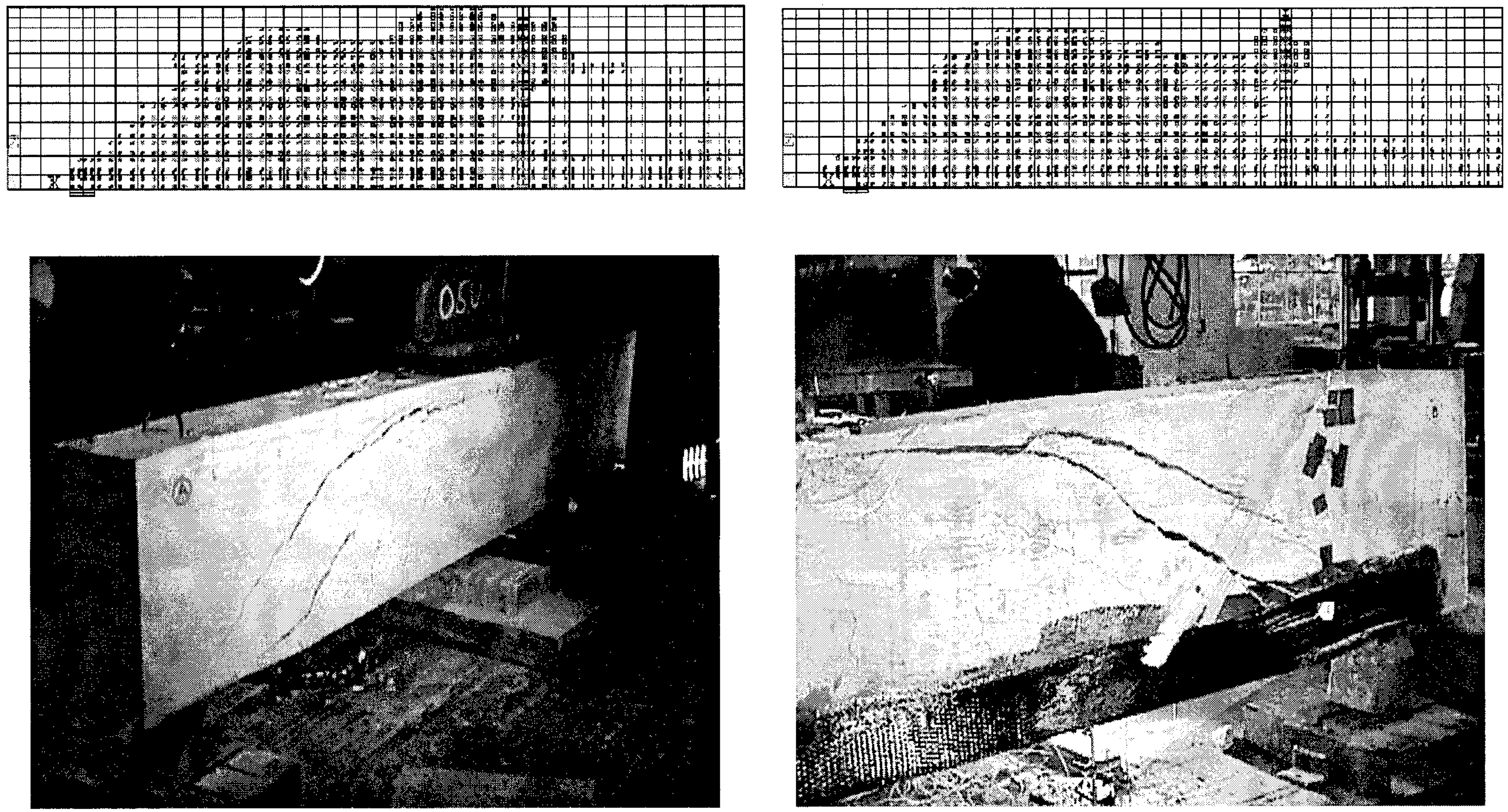

Figure 3.29: Crack patterns at failure: (a) Control Beam; (b) Flexure Beam

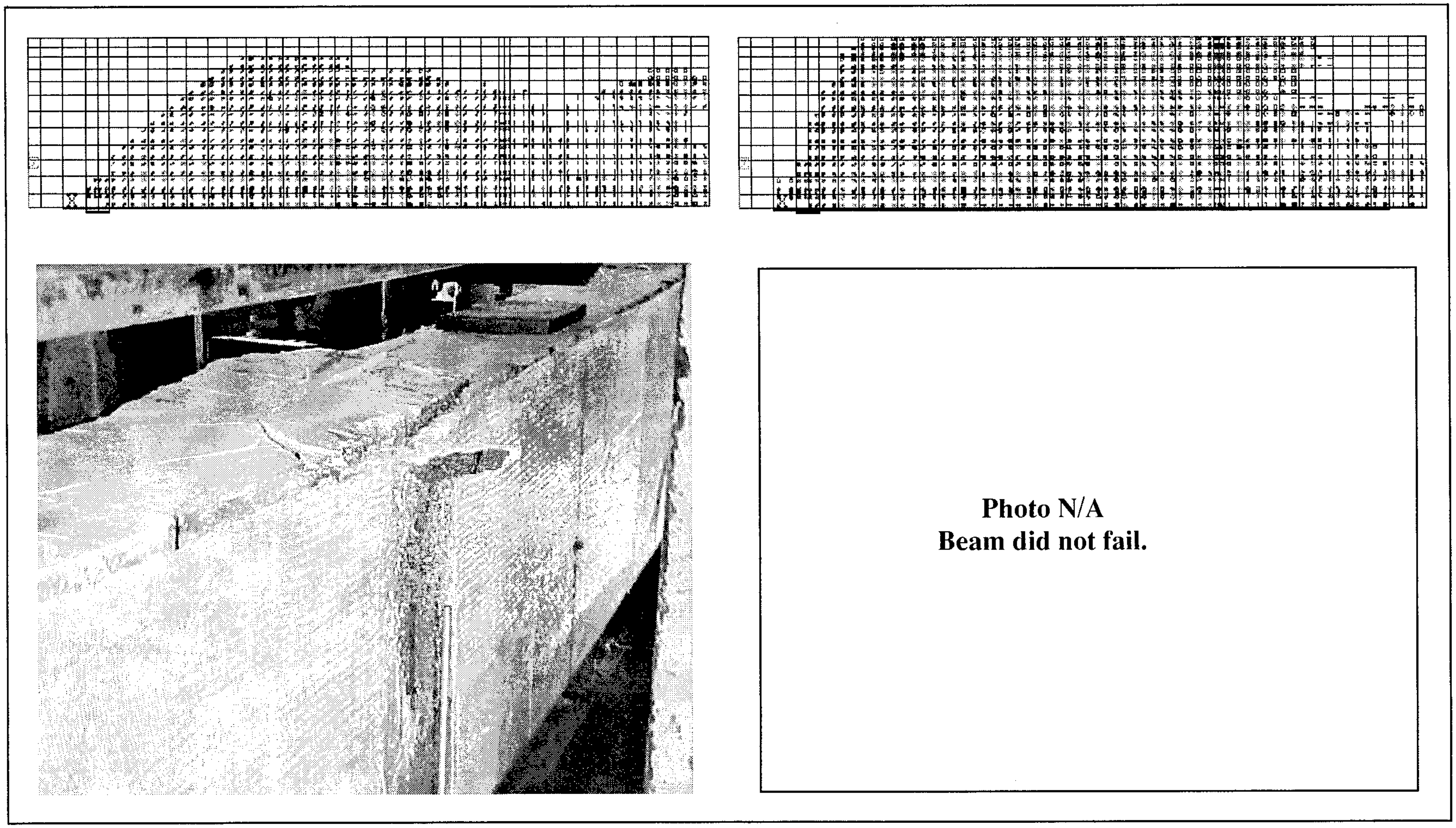

Photo N/A
Beam did not fail.

Figure 3.30: Crack patterns at failure: (a) Shear Beam; (b) Flexure/Shear Beam

3.7 MAXIMUM STRESSES IN FRP COMPOSITES

For the actual flexure and Shear Beams, there was no evidence that the FRP reinforcing failed before overall failure of the beams. This is confirmed by the finite element analyses. In Table 3.3 maximum stresses for the last converged load step are compared to the ultimate tensile strengths for the composites, along with the location of the maximum stress. Figure 3.31 shows the maximum stress locations in the FRP composites.

Table 3.3: Maximum stresses developed in the FRP composites and the corresponding ultimate tensile strengths

Beam	Maximum tensile stress (ksi)	Ultimate tensile strength (ksi)*	Location (*x*, *y*, *z*) (in)**
Flexure beam (CFRP)	28.7	139	(66,6,0)
Shear beam (GFRP)	7.22	87.0	(114,4,0)
Flexure/Shear beam	71.8 (CFRP) 5.91 (GFRP)	139 (CFRP) 87.0 (GFRP)	(120,0,0) (57,4,0)

*(*Kachlakev and McCurry 2000*)
**(*x*, *y*, *z*) corresponds to (length, width, height) directions on the beams. The origin (0, 0, 0) is at the corner of the bottom face of the beams as shown in Figure 3.31(a).

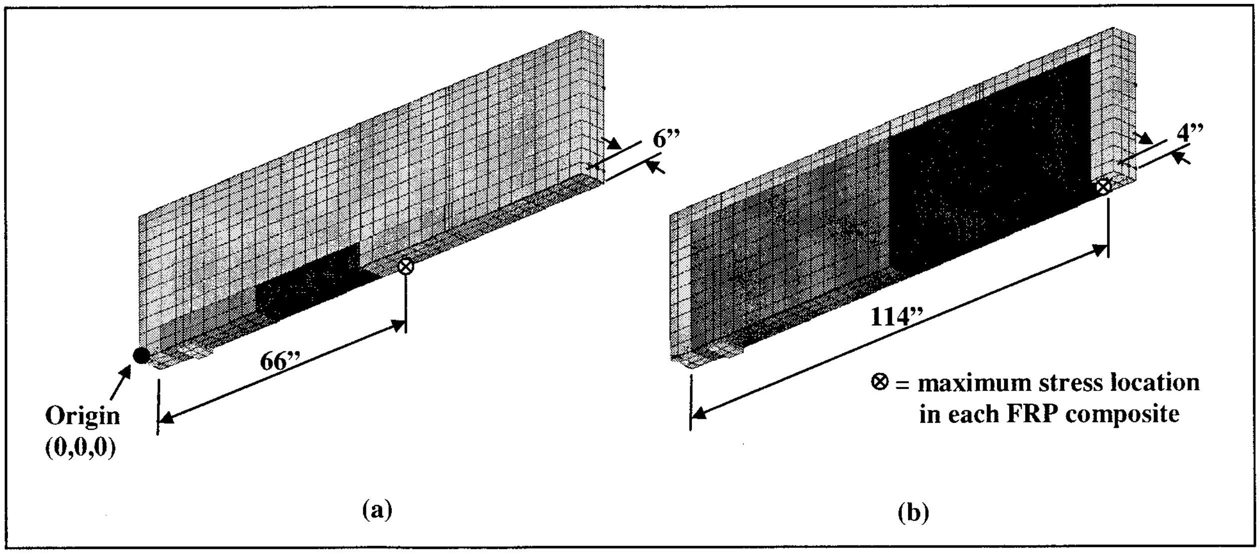

Figure 3.31: Locations of maximum stresses in FRP composites: (a) Flexure Beam; (b) Shear Beam

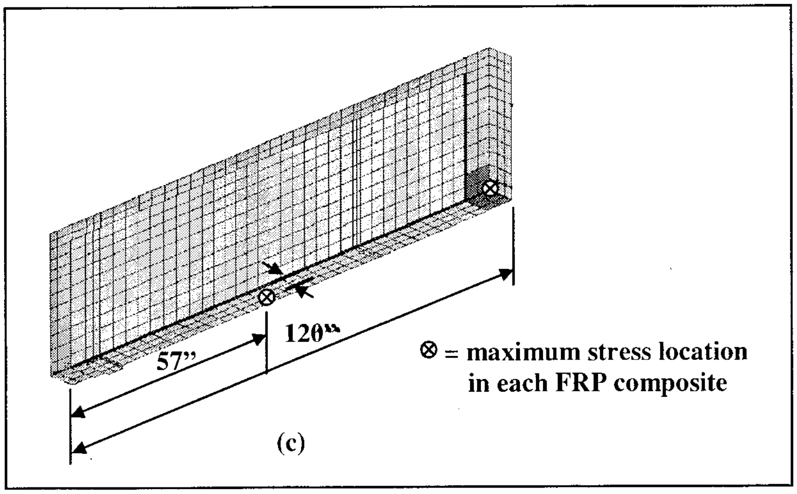

Figure 3.31 (continued): Locations of maximum stresses in FRP composites: (c) Flexure/Shear Beam

3.7.1 Comparisons to Parallel Research

A parallel modeling effort was conducted at Oregon State University by Chansawat for the Control Beam and the Flexure/Shear Beam (*Chansawat 2000*). The Control Beam models from Chansawat's work and this study have nearly the same geometric configurations. One difference, however, between the two Control Beam models was the method of mesh generation. This study uses mesh generation based on a solid modeling method, whereas mesh generation of Chansawat's model was based on a direct generation method. The load stepping defined for the analyses was also different, especially the load step sizes close to failure. Chansawat used 0.045 kg (0.1 lb) as the minimum load step size, while this study used a 0.45 kg (1 lb) load increment.

The Flexure/Shear Beams from the two studies also had nearly the same geometric configurations as the Control Beam, except for the number of elements, due to the different methods used in modeling the FRP composites. For Chansawat's model, CFRP and GFRP composites were modeled as layers in one element, whereas for this study each FRP composite was separately modeled. Mesh generation and load stepping for the two studies were also different.

The computed stiffnesses from the two models are almost identical for both the Control and Flexure/Shear Beams. The crack patterns predicted by the ANSYS program from the two studies are very similar. The load-carrying capacities of the beams from the two studies are slightly different, however. The failure loads of the Control Beam and Flexure/Shear Beam modeled by Chansawat are higher than this study by 0.5% and 4% respectively. The differences in the FRP composite modeling and the load stepping between the two analyses could have caused these differences in the load-carrying capacities.

4.0 ANALYSIS OF HORSETAIL CREEK BRIDGE

4.1 INTRODUCTION

This chapter presents the analysis of the Horsetail Creek Bridge. The FEM techniques developed for the nonlinear analysis of the full-scale beams were extended into this investigation. Field test data for the bridge were provided by the Oregon Department of Transportation (*ODOT 2000, ODOT 2001*). Unfortunately, field test data were available only for the structure after FRP strengthening. There was no control set of data available to represent the bridge's response prior to the retrofit. A finite element model of the Horsetail Creek Bridge after retrofitting was developed, and two levels of truck loading were applied to the bridge model at different locations, as in the actual bridge test. Comparisons between ANSYS predictions and field data are discussed in this chapter. In addition, a finite element model of the bridge before retrofitting was also developed and analyzed.

4.2 BRIDGE DESCRIPTION AND FIELD DATA

4.2.1 Horsetail Creek Bridge

The Horsetail Creek Bridge consists of three spans 6096 mm (20 ft) long and 7315 mm (24 ft) wide with spread footing foundations. For the transverse beams, the FRP strengthening detail is generally the same as that for the Flexure/Shear Beam discussed in Chapter 3. However, due to the bridge deck, the height of GFRP laminates is shorter on the bridge compared to the Flexure/Shear Beam. On the longitudinal bridge beams, only GFRP laminates were used to provide adequate shear resistance. The plan and elevation of the bridge are shown in Appendix A along with the steel reinforcement and FRP strengthening details.

4.2.2 Loading conditions

Two field tests were conducted by ODOT (*ODOT 2000, ODOT 2001*). They will be referred to as "Field Test 1," and "Field Test 2." Field Test 1 was performed in November 2000, and Field Test 2 in February 2001. In each field test, strain data were collected with an empty and a full truck at seven positions on the Bridge, as shown in Figure 4.1. The truck weights used for Field Test 2 were kept as similar as possible to those used for Field Test 1 for verification purposes. Due to the winter season, however, a snowplow was mounted on the truck used in Field Test 2. As a result, the weights for both empty and full truck loads were somewhat different between field tests. The configurations and axle weights for the trucks used in both tests are shown in Appendix B.

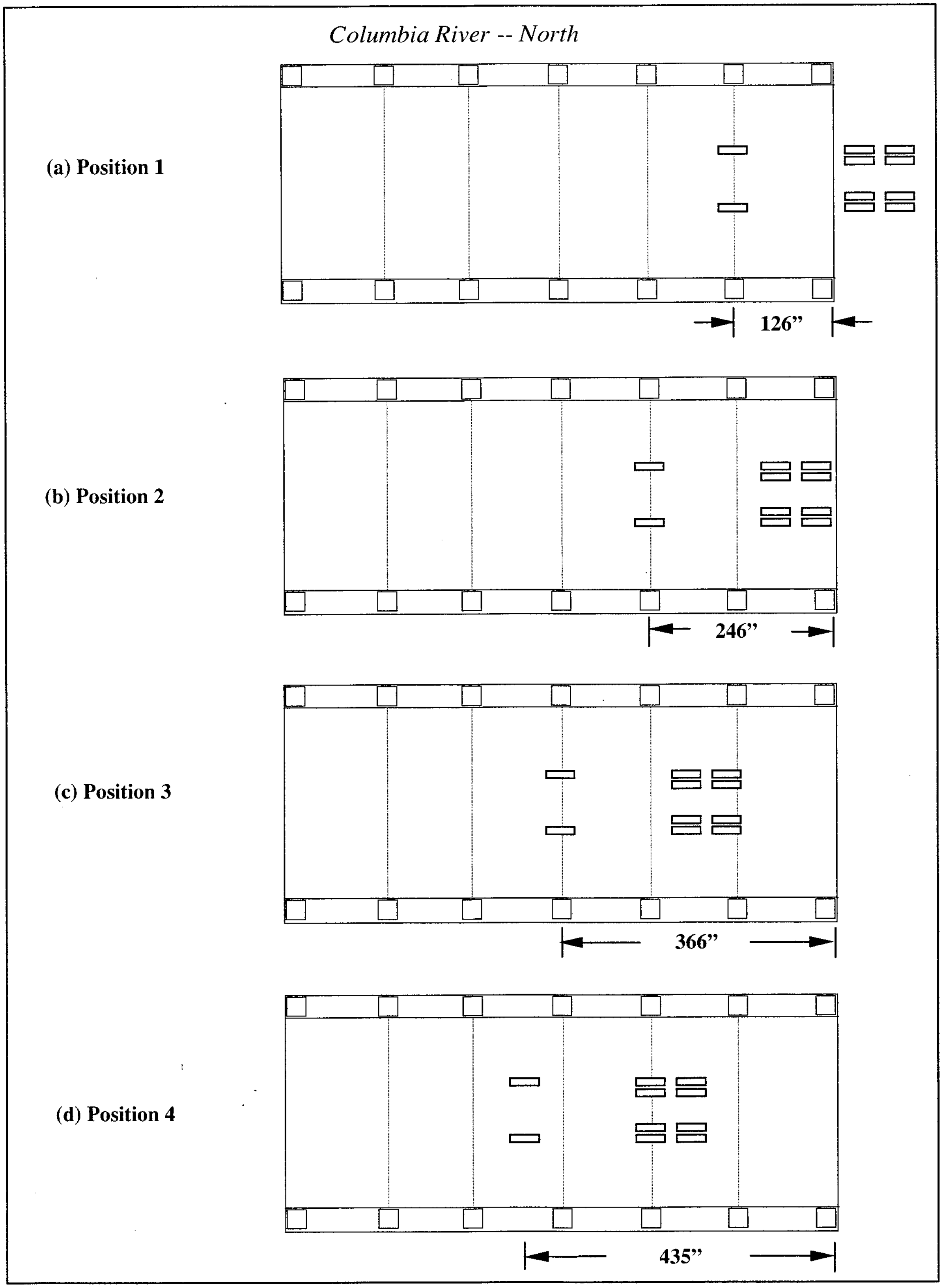

Figure 4.1: Locations of truck on the Horsetail Creek Bridge

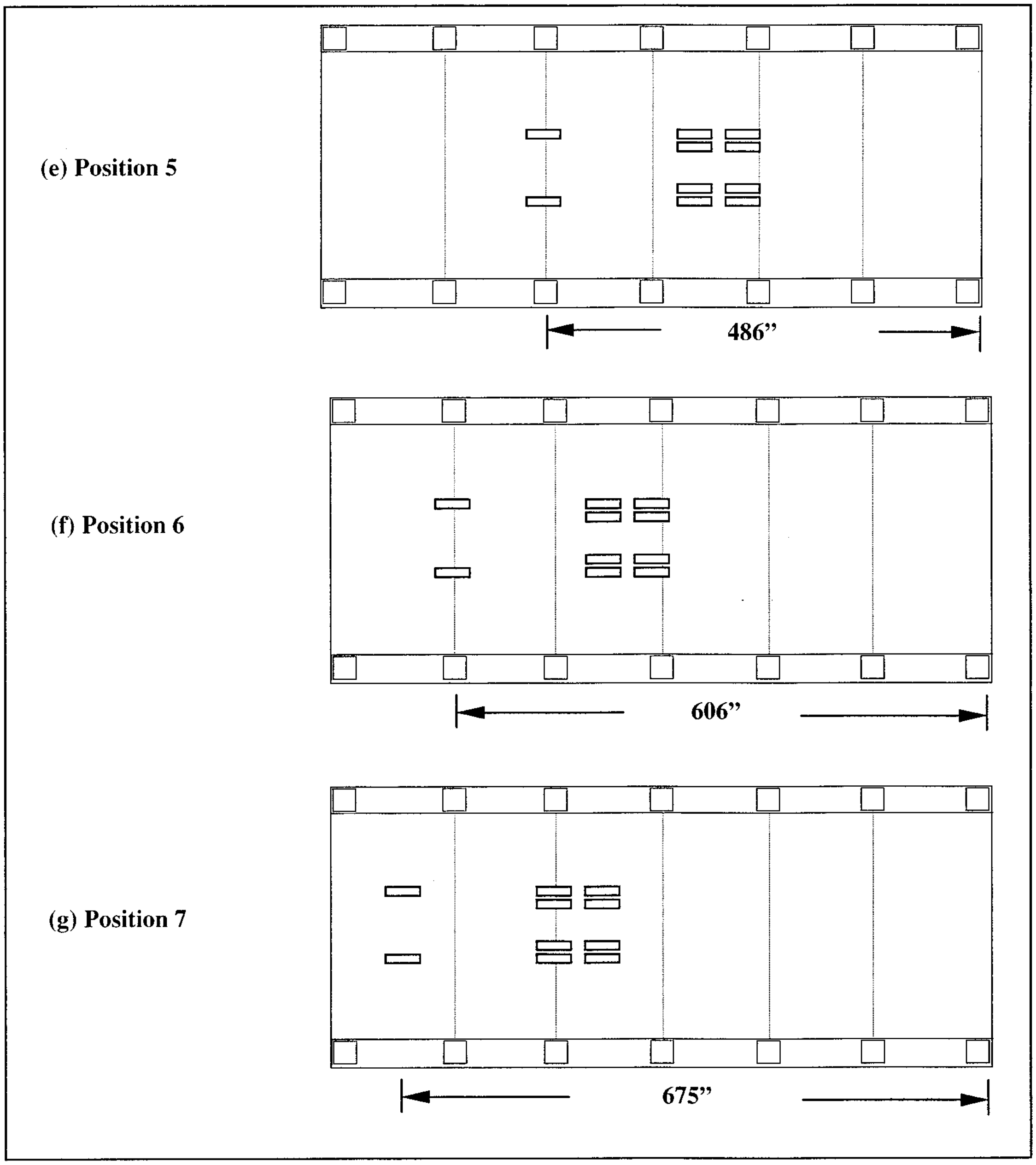
(e) Position 5

(f) Position 6

(g) Position 7

Figure 4.1 (continued): Locations of truck on the Horsetail Creek Bridge

4.2.3 Field data

Fiber optic strain sensors were placed in the concrete and on the surface of the FRP laminates when the composite was applied. They were located on the bottom and side of one transverse beam and one longitudinal beam, as shown in Appendix C. The locations of these transverse and the longitudinal beams are shown in Figure 4.2 (shaded areas).

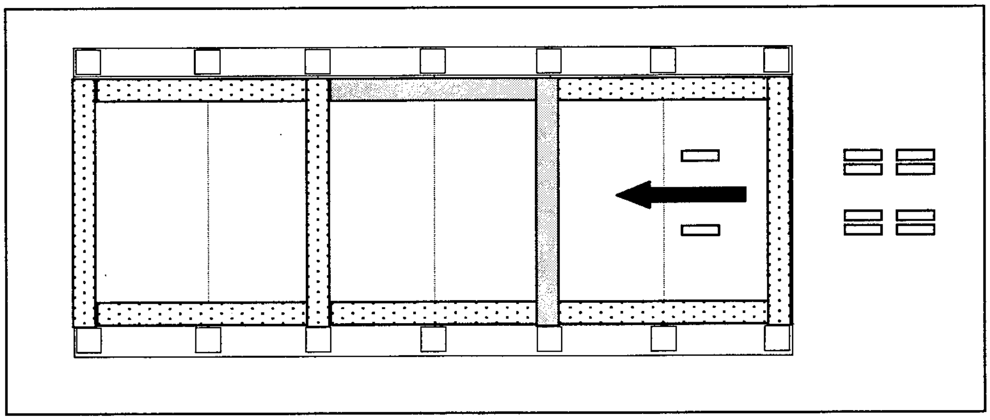

Figure 4.2: Locations of the monitored beams on the Horsetail Creek Bridge

4.3 FEM MODEL

ANSYS was used to model the Horsetail Creek Bridge. Due to the much more complex geometry and reinforcement details compared with the full-size beams, more modeling time and effort were needed, however.

4.3.1 Materials properties

Most of the materials properties used in the nonlinear analysis of the full-scale beams were applicable to the bridge study, as shown in Table 4.1. The two exceptions were the initial modulus of elasticity of concrete and the yield strength of the steel bars, which were assigned 19,650 MPa (2,850,000 psi) and 276 MPa (40,000 psi) (Grade 40 steel), respectively.

Table 4.1: Material properties (*Kachlakev and McCurry 2000; Fyfe Corp. 1998*)

Type of Material	Material Properties				
	ν	E (psi)	G (psi)	Strength (psi)	Thickness (in.)
Concrete	0.2	2850000	-	f'c = 2500** f't = 375	-
Reinforcing steel	0.3	29000000**	-	fy = 40000**	-
CFRP laminate	$\nu_{12} = 0.216$ $\nu_{13} = 0.216$ $\nu_{23} = 0.3$*	$E_{11} = 9000000$ $E_{22} = 700000$* $E_{33} = 700000$*	$G_{12} = 473700$* $G_{13} = 473700$* $G_{23} = 270000$***	$\sigma_{ult(ten.)} = 139000$ $\sigma_{ult(comp.)} = 86880$ $\tau_{ult(12)} = 14500$	0.042
GFRP laminate	$\nu_{12} = 0.216$ $\nu_{13} = 0.216$ $\nu_{23} = 0.3$*	$E_{11} = 3000000$ $E_{22} = 1000000$* $E_{33} = 1000000$*	$G_{12} = 220000$ $G_{13} = 220000$ $G_{23} = 385000$***	$\sigma_{ult(ten.)} = 87000$ $\sigma_{ult(comp.)} = 48330$ $\tau_{ult(12)} = 4400$	0.052

*(*Kachlakev 1998*)
**(*CH2M Hill 1997*)
*** $G_{23} = \frac{E_2}{2(1+\nu_{23})}$

4.3.2 Bridge modeling and analysis assumptions

Modeling and analysis assumptions explained in Chapter 2 were applied in the overall bridge analysis. In addition, another assumption was made in the bridge study. In order to analyze all the load locations on the bridge deck without changing the mesh, the load for each set of dual tires was lumped and assumed to occur at the center of the dual tires, as shown in Figure 4.3. The truck configuration from Field Test 1 was used in all FE analyses.

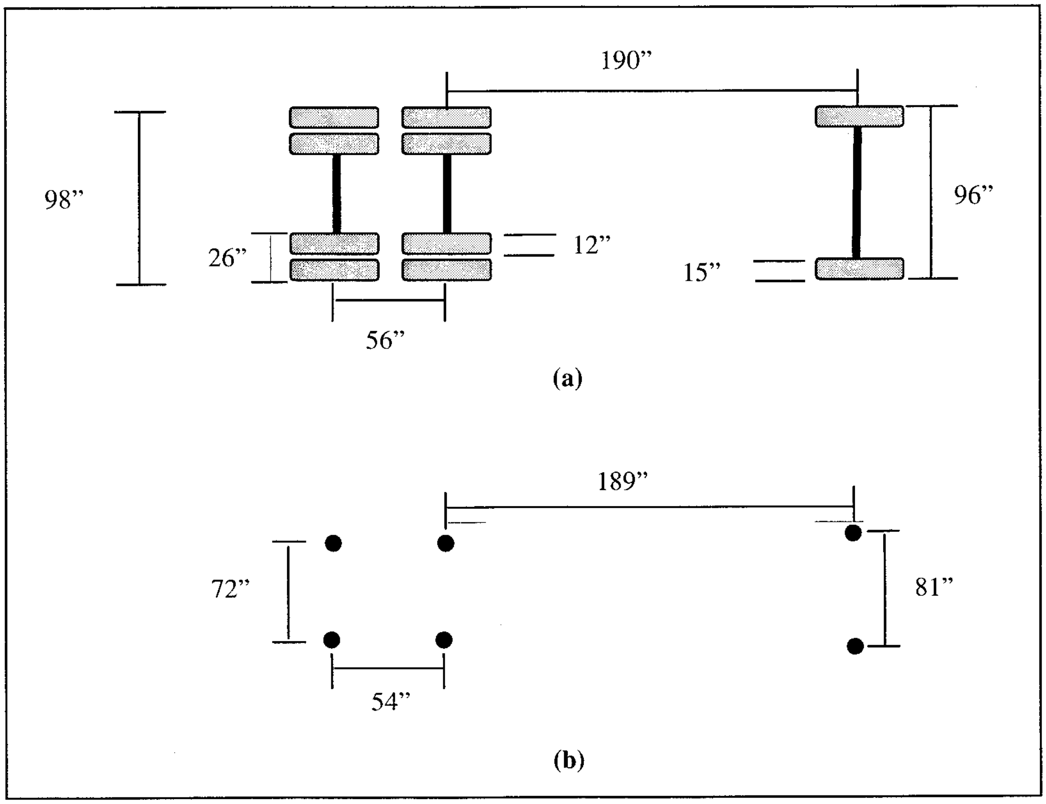

Figure 4.3: Truck load simplification: (a) and (b) show configurations of the dump truck and the simplified truck, respectively

At locations where the lumped load did not coincide with a node in the mesh, the load was linearly distributed to the nearest nodes. An example of this distribution is shown in Figure 4.4. With this approach, truck loads were applied to the bridge deck regardless of the locations of the nodes.

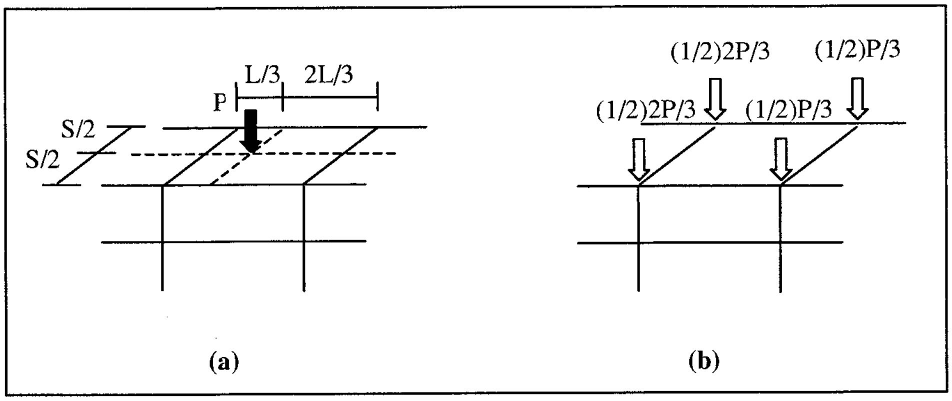

Figure 4.4: Linear truck load distribution

4.3.3 Finite element discretization

The constitutive models, material properties, and assumptions previously discussed were used in the bridge analysis. As with the full-scale beam modeling, SOLID65, LINK8, and SOLID46 elements were used to model the bridge. Taking advantage of symmetry, only a longitudinal half of the bridge was modeled. The columns of the bridge were also modeled and were assumed to be rigidly fixed to the ground. Therefore, all degrees of freedom (DOF) at the bottoms of the columns were restrained. Only vertical translation was restrained, however, where the walls are located (at both ends of the bridge). It was also assumed that the corners of the bridge were rigidly fixed to the ground where the spread footings are located. The effects of the boundary conditions defined in the study will be discussed in the next section. The numbers of elements used in the model are summarized in Table 4.2.

Table 4.2: Summary of the number of elements used in the bridge model

Type of Element	No. of Elements
Concrete (SOLID65)	9520
Steel Bar (LINK8)	4354
FRP (SOLID46)	1168
Total	15042

The bridge model with steel reinforcement details is shown in Figure 4.5. The label “1-0.78 in^2” represents one steel bar with an area of 0.78 in^2, while “2-2 in^2” represents two steel bars with an area of 2 in^2 for each bar, and so on. A standard size bar could not be used because undeformed square bars were used in the actual bridge. “Lumping” of reinforcing steel bar areas was used in the FE bridge modeling, as in the full-size beam modeling. The steel reinforcement details of the actual bridge are shown in Appendix A.

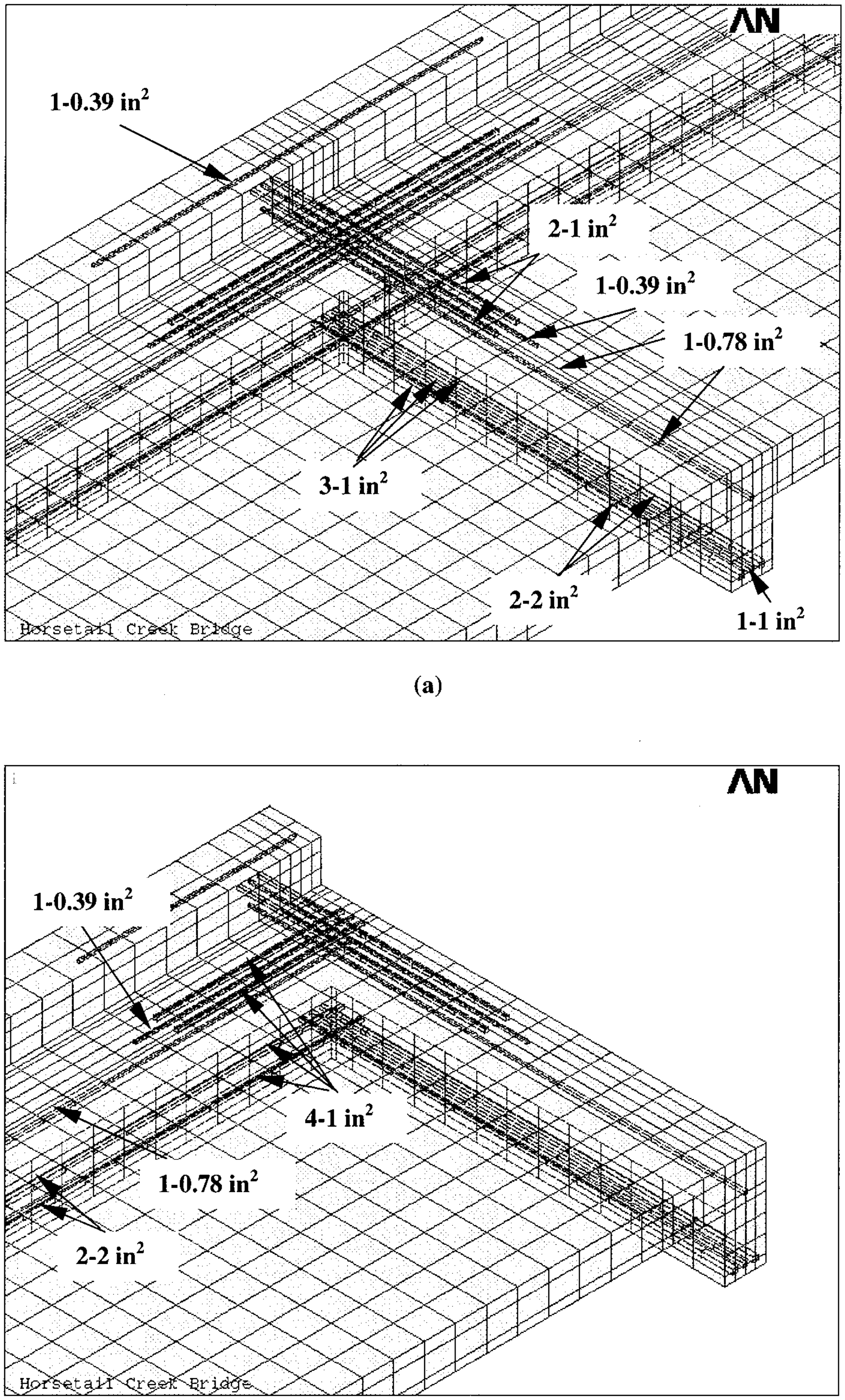

Figure 4.5: Steel reinforcement details: (a) and (b) show typical reinforcement in the transverse and longitudinal beams at the middle and at the end of the bridge, respectively

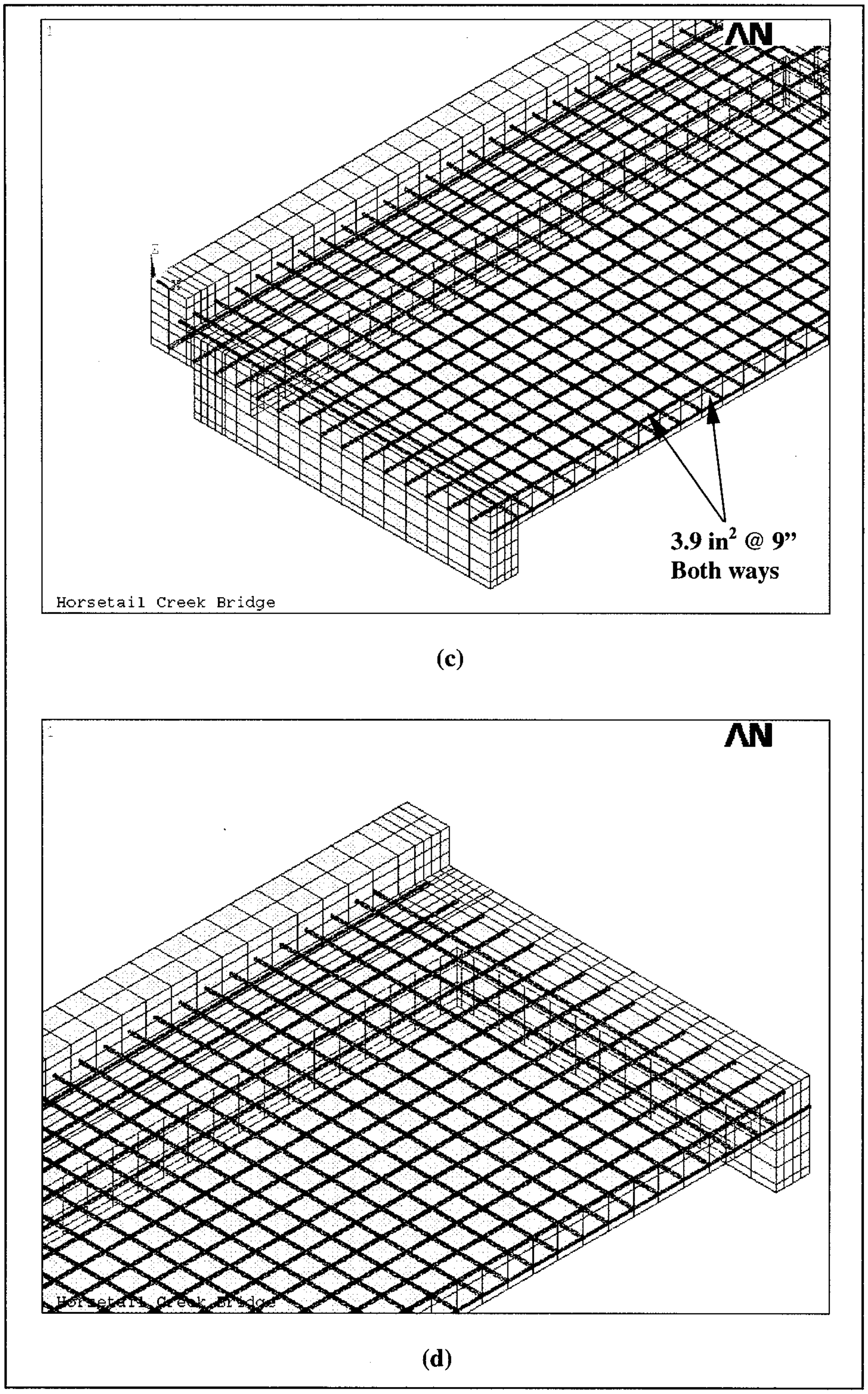

Figure 4.5 (continued): Steel reinforcement details: (c) and (d) show typical reinforcement in the bridge deck at both ends of the bridge

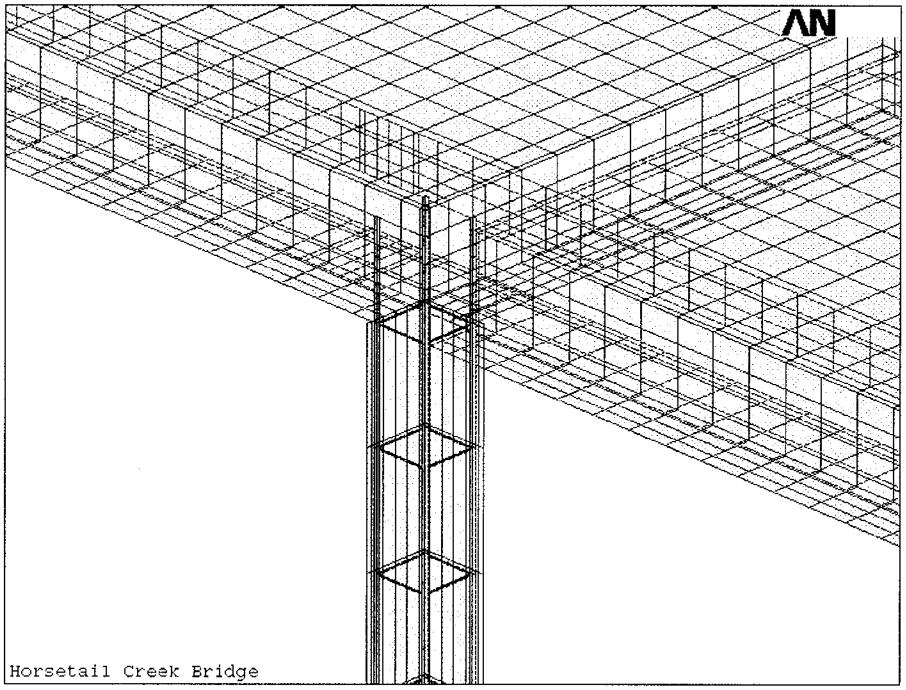

(e)

Figure 4.5 (continued): Steel reinforcement details: (e) shows typical reinforcement in the columns

Figure 4.6 shows the FRP laminates. The sections of the longitudinal beams with 2 layers and 4 layers of GFRP are indicated. Except for the presence of the deck, the composite configuration on the longitudinal and transverse beams was identical to the configuration for the Shear Beam and Flexure/Shear Beam discussed in Chapter 3.

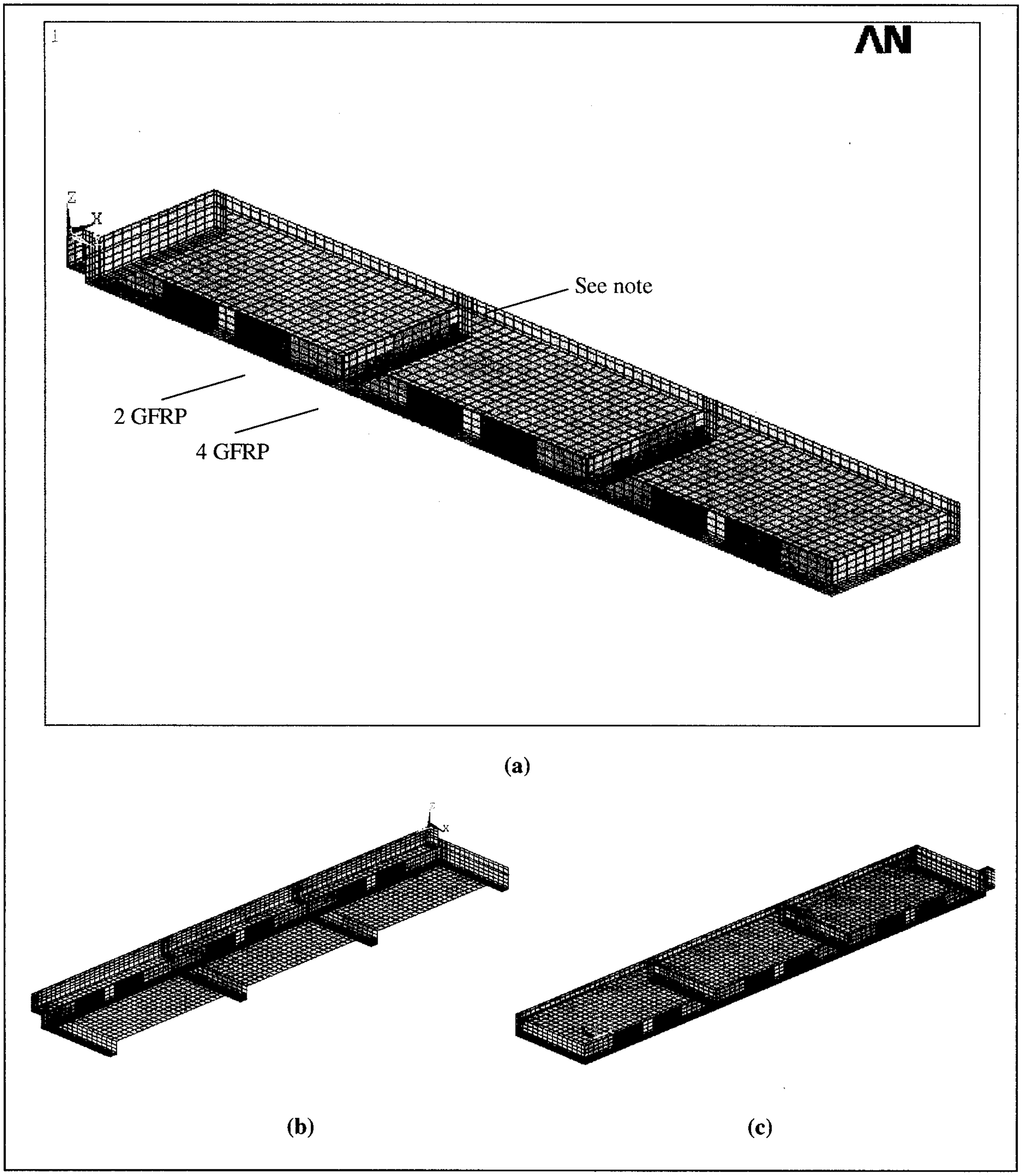

(a)

(b)

(c)

Figure 4.6: FE bridge model with FRP laminates: (a), (b), and (c) show the FRP strengthening in different views.

Figure 4.7 shows the boundary conditions for the model.

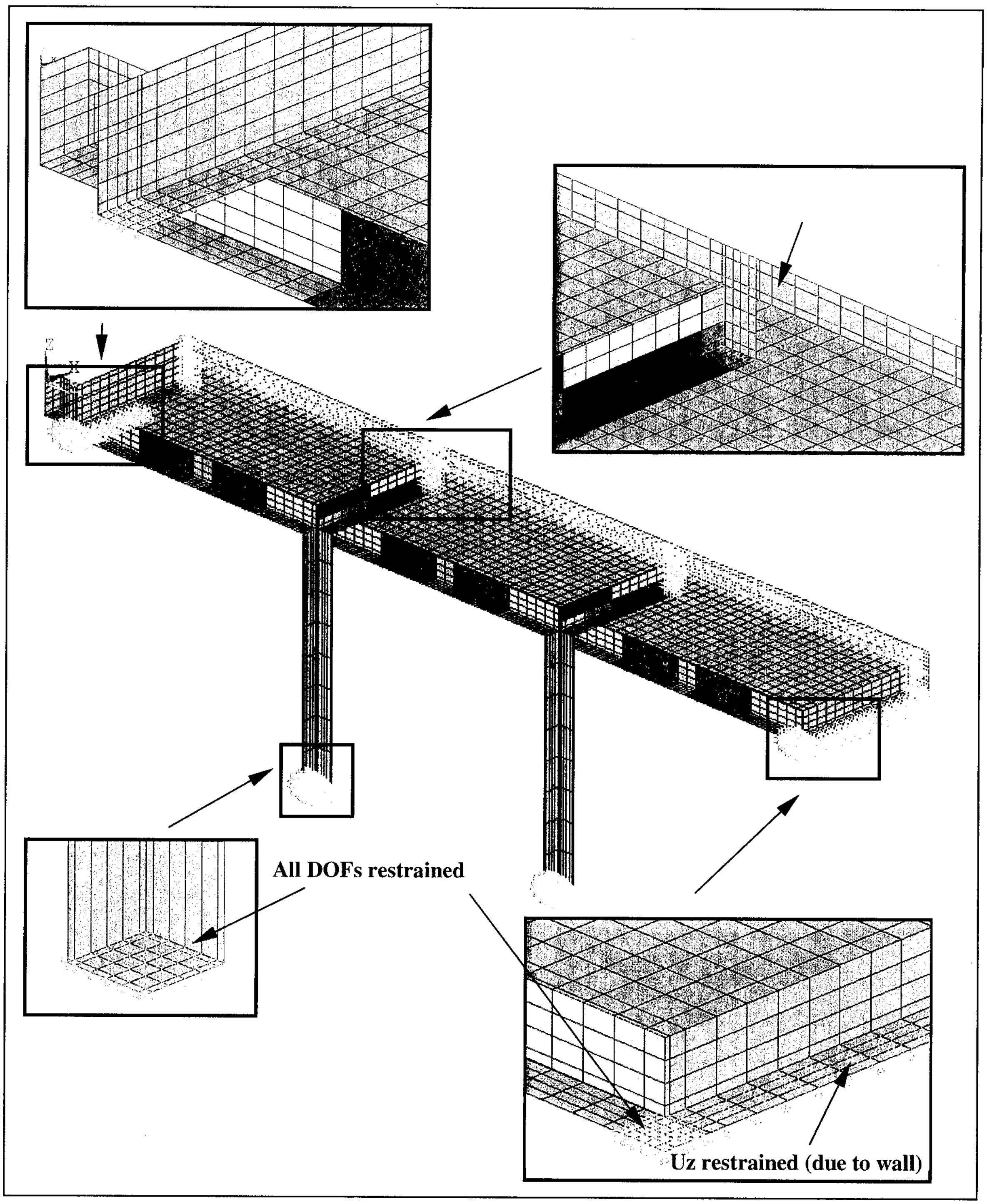

Figure 4.7: Boundary conditions for the bridge

4.4 COMPARISONS OF ANSYS AND SAP 2000 PREDICTIONS WITH FIELD DATA

On examining the ANSYS results for all of the truck positions, it was found that the bridge did not crack for the empty truck. Therefore, the study was a linear analysis, and it was possible to include the linear analysis results obtained from SAP2000 in these comparisons (*OSU 2000*) as a preliminary verification of the ANSYS model. Differences between the ANSYS and SAP2000 bridge models are pointed out in Table 4.3. It should be noted that the strain results obtained for both ANSYS and SAP2000 are based on essentially the truck weights used in Field Test 1.

Table 4.3: Differences between ANSYS and SAP2000 bridge models

Categories	Models	
	ANSYS	SAP2000 [OSU, 2000]
Types of Elements		
Concrete	SOLID65 (Nonlinear)	Conventional solid element (Linear)
Steel	LINK8 (Nonlinear)	Truss element (Linear)
FRP	SOLID65 (Nonlinear)	Truss element (Linear)
Material Properties		
Concrete	See Table 4.1	E = 2850000 psi, ν = 0.2
Steel	See Table 4.1	E = 29000000 psi, ν = 0.3
FRP	See Table 4.1 (Orthotropic)	E(CFRP) = 9000000 psi, ν = 0.23 E(GFRP) = 3000000 psi, ν = 0.21
Model Descriptions		
Modeling Approach	A longitudinal half of the bridge modeled (Symmetry)	Full model
Height of the Columns	192" (16') high	174" (14.5') high
Size of the Columns	14.6" x 14.6"	16" x 16"
Boundary Conditions		
Under Columns	All DOFs restrained	All DOFs restrained
Left End	See Figure 4.6	All DOFs restrained
Right End	See Figure 4.6	Vertical translation restrained
Total No. of Elements		
Concrete	20192	10642
Steel	9428	3862
FRP	2336	1175
Total	31956	15679

The differences between these two models will affect comparisons of the structural response predictions between ANSYS and SAP2000. In the SAP2000 analysis, truss elements with isotropic material properties are used to represent the FRP laminates (*OSU 2000*), which is not as realistic and may reduce the overall structural stiffness compared to the SOLID46 elements with orthotropic material properties that are used to model the FRP laminates in ANSYS. The differences in the boundary conditions at both ends of the bridge deck also affect the solutions. At the right end of the SAP2000 bridge model, horizontal translations are permitted, but not for the ANSYS bridge model. This may also reduce the stiffness in the SAP2000 bridge structure relative to the ANSYS model. On the other hand, one factor will make the ANSYS bridge model somewhat less stiff than the SAP2000 model: i.e., the differences in height and size of the columns. As shown in Table 4.3, larger and shorter columns were used in the SAP2000 analysis and made the SAP2000 model stiffer. (The size and height of the columns used in the ANSYS model were those directly measured from the actual bridge.)

Additionally, the differences in the number of elements used in the ANSYS and SAP2000 models will also affect the solutions. After the symmetry condition is taken into account, the ANSYS model has more than twice as many elements as the SAP2000 model, as shown in Table 4.3. Thus, it is expected that due to more realistic modeling of both the element types and the geometric properties, together with the use of more elements, the ANSYS model will provide the best prediction of the behavior of the bridge under truck loadings.

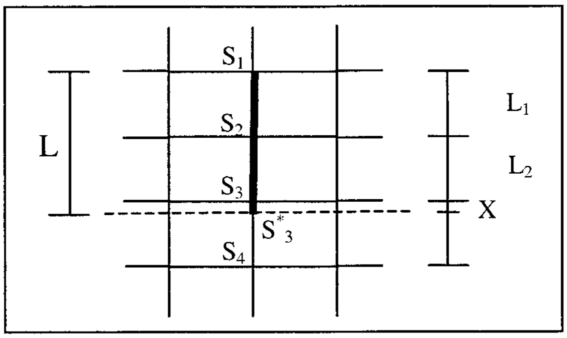

Figure 4.8: Fiber optic sensor (plan view)

The relatively long gauge length of the sensor [1070 mm (42")] on the bridge made comparisons challenging where the strains varied considerably over those lengths. Due to the length of the fiber optic sensors, it would not be appropriate to use the result from only one node from the FE model to represent the strain value. The strains from several nodes need to be examined to obtain a strain comparable to the field data. The strain calculation is based on a weighted average that depends on the "tributary" length for each node. For instance, consider a fiber optic sensor attached to an FE model. Then:

$$S_{avg} = \frac{\frac{S_1 L_1}{2} + \frac{S_2}{2}(L_1 + L_2) + \frac{S_3}{2}(L_2 + X) + \frac{S_3^* X}{2}}{L} \tag{4.1}$$

$$S_4 = S_3 + X\left(\frac{S_4 - S_3}{L_3}\right) \qquad \textbf{(4.2)}$$

where:

S_{avg} = Average strain used to compared with the field strain data
S_1, S_2, S_3, and S_4 = ANSYS nodal strains
L_1, L_2, and L_3 = Length of each element
L = Length of the fiber optic sensor
S^*_3 = Interpolated strain between S_3 and S_4

There were 12 sensors installed on the bridge to measure flexural strains. In Field Test 1, data were obtained from the following eight sensors:

- T0FC: The strain at the center bottom fiber of the concrete for the transverse beam at midspan.
- T1FC: The strain at the center bottom of the transverse beam at midspan on the FRP laminate.
- T0FR: The strain at 1"-off center for the bottom fiber of the concrete for the transverse beam at the north end.
- T1FR: The strain at 1"-off center for the bottom of the transverse beam at the north end on the FRP laminate.
- L0FC: The strain at the center bottom fiber of the concrete for the longitudinal beam at midspan.
- L1FC: The strain at the center bottom of the longitudinal beam at midspan on the FRP laminate.
- L0FL: The strain at 1"-off center for the bottom fiber of the concrete for the longitudinal beam at the east end.
- L0FR: The strain at 1"-off center for the bottom fiber of the concrete for the longitudinal beam at the west end.

In Field Test 2, data were obtained from the same set of sensors except T1FR, which malfunctioned at the time of the test.

Comparisons between ANSYS predictions and Field Tests 1 and 2 for the strains versus the various truck locations are shown in Figures 4.9 and 4.10. To better represent the effects of the moving truck on the structural behavior of the bridge, the strains are also plotted versus the distances of the single front axle of the truck from the end of the bridge (Figure 4.1) and are shown in Figures 4.11 and 4.12. Basically, these plots are similar to "influence lines," but for a truck instead of a unit load. It should be noted that SAP2000 results are available only for the empty truck condition and only at locations T0FC and L1FC.

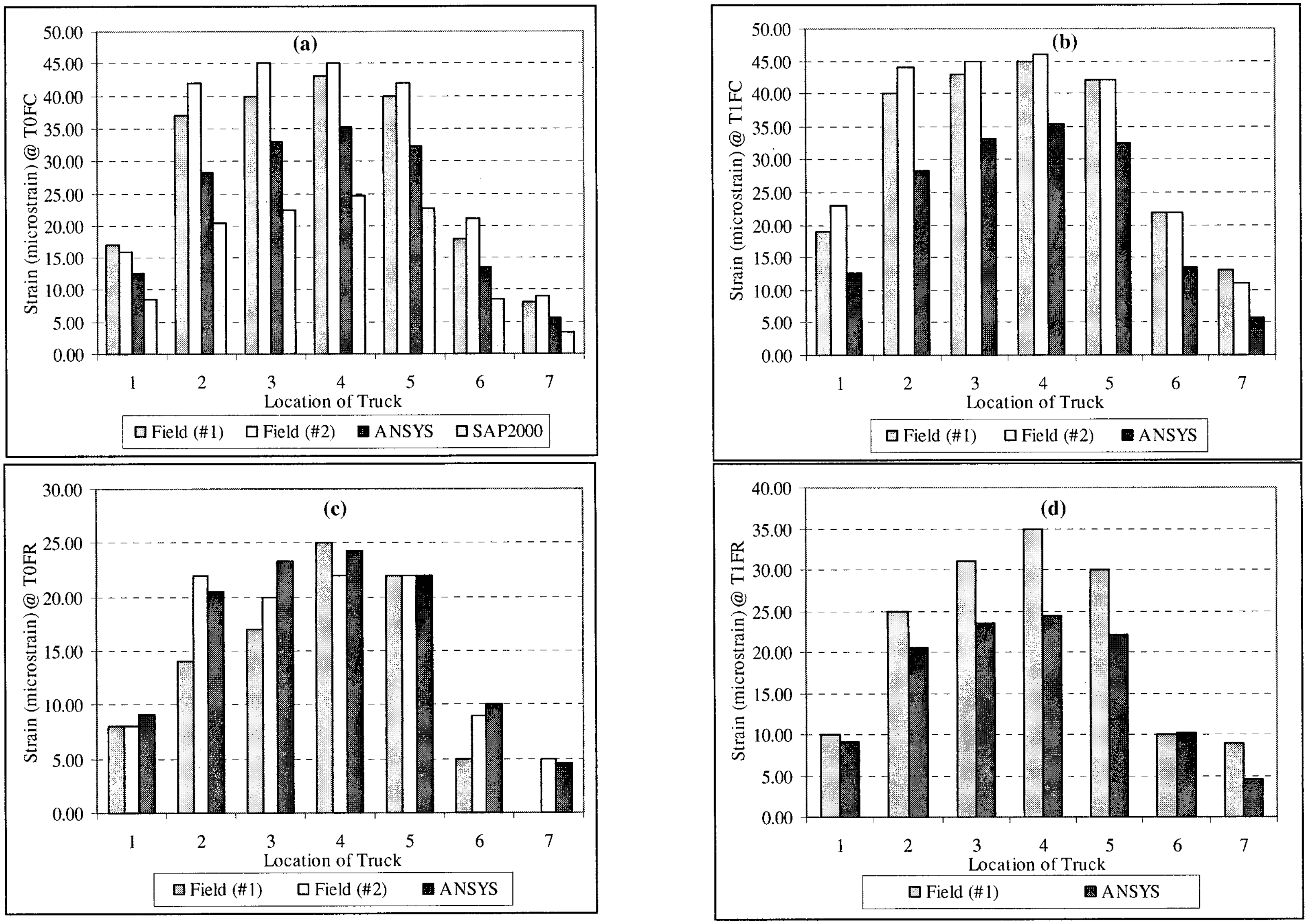

Figure 4.9: Comparison of strains from Field Tests 1 and 2, ANSYS, and SAP2000 for the empty truck at the seven Locations: (a) - (d) show the strains on the transverse beam

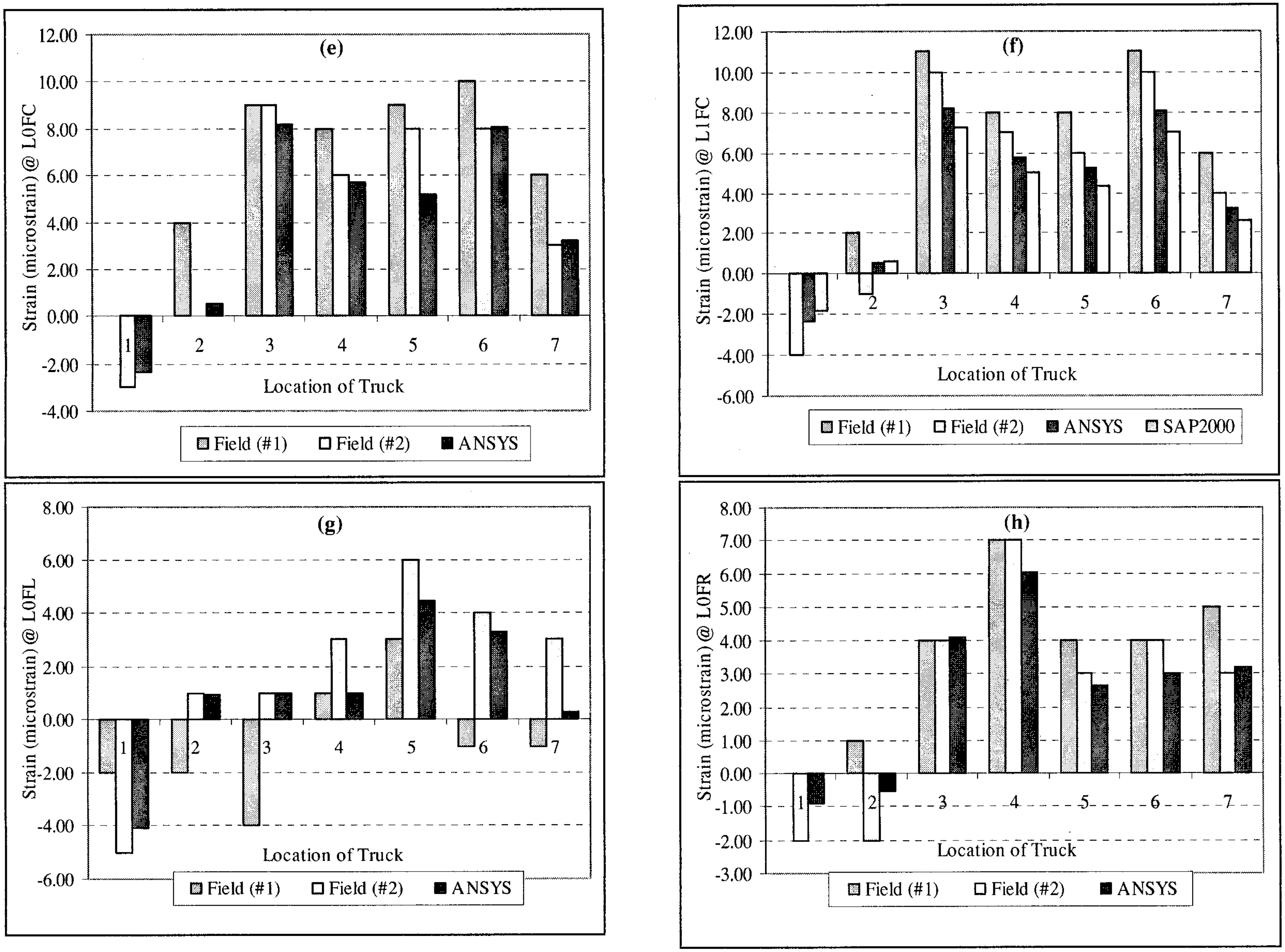

Figure 4.9 (continued): Comparison of strains from Field Tests 1 and 2, ANSYS, and SAP2000 for the empty truck at the seven Locations: (e)-(h) show the strains on the longitudinal beam.

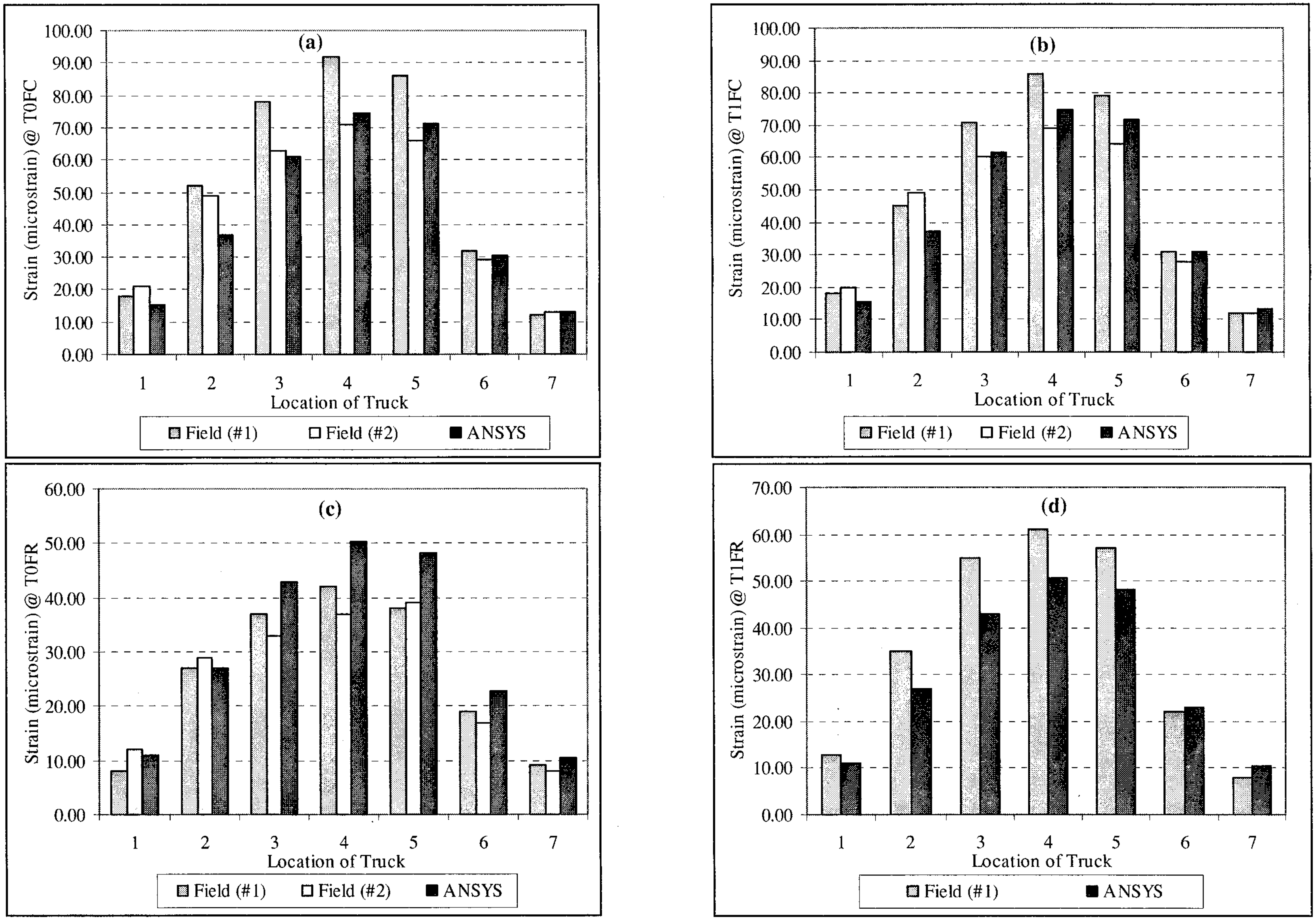

Figure 4.10: Comparison of strains from Field Tests 1 and 2, ANSYS, and SAP2000 for the empty truck at the seven locations: (a) - (d) show the strains on the transverse beam

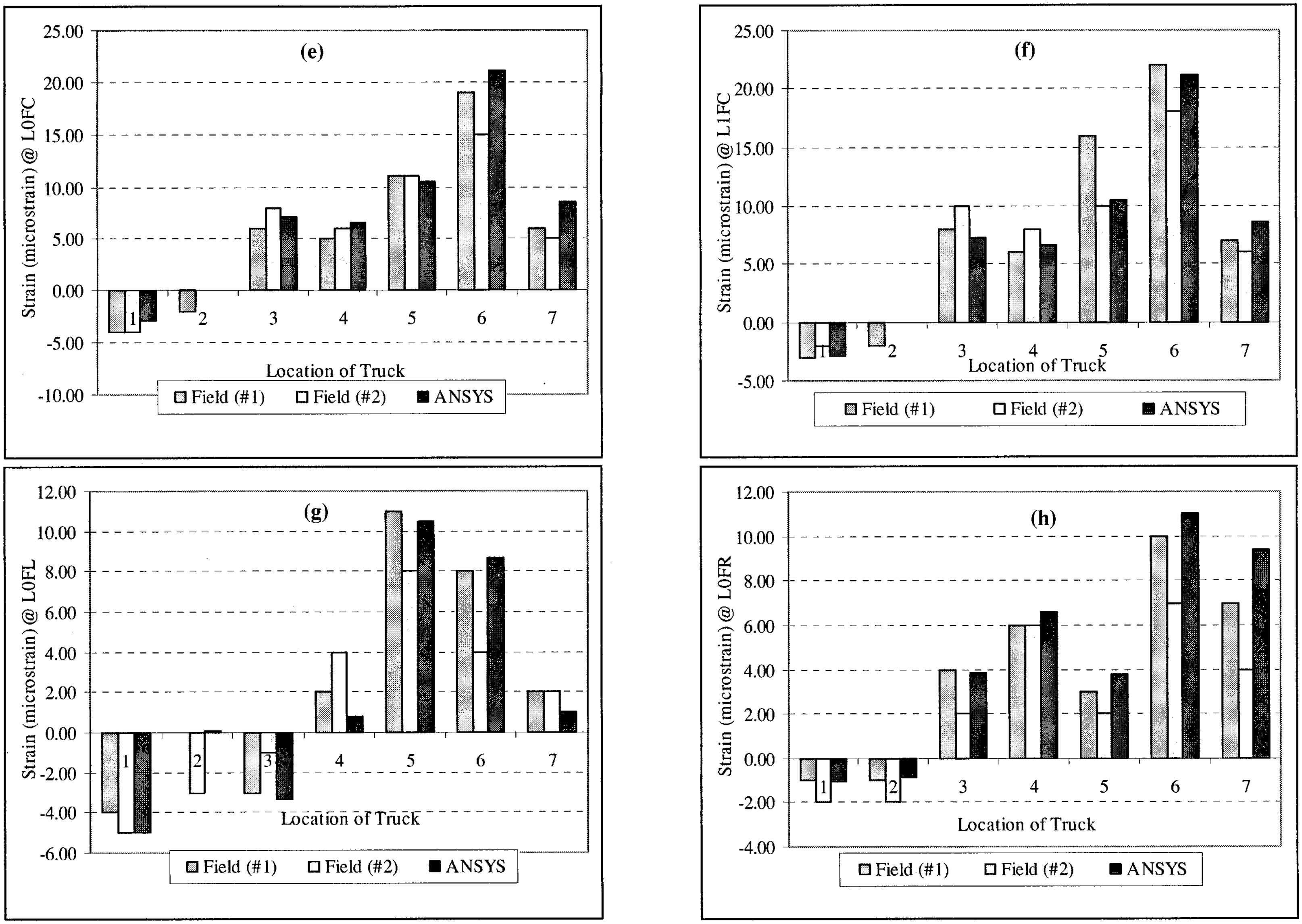

Figure 4.10 (continued): Comparison of strains from Field Tests 1 and 2, ANSYS, and SAP2000 for the empty truck at the seven locations: (e)-(h) show the strains on the longitudinal beam.

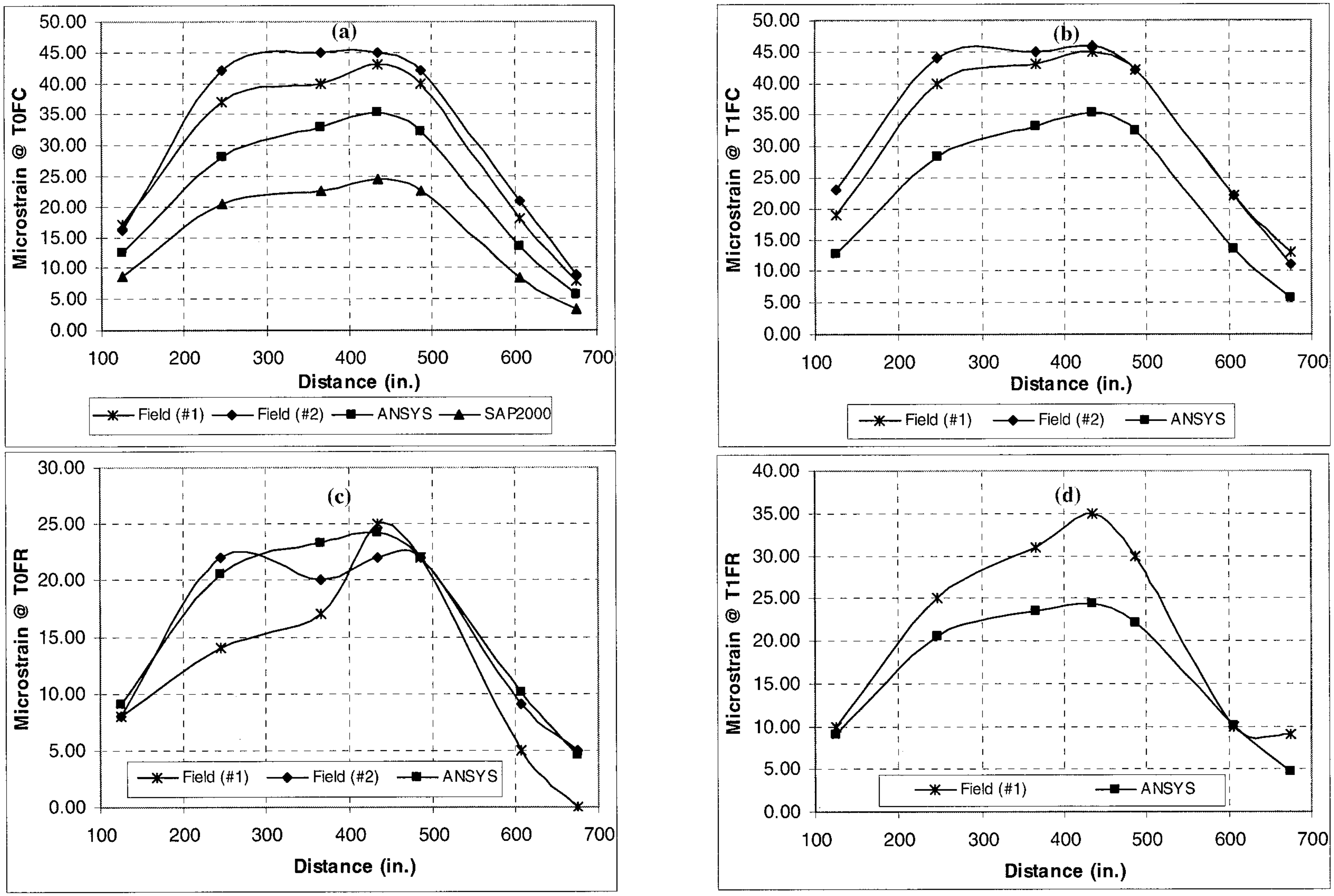

Figure 4.11: Comparison of strain versus distance of the single axle from the end of the bridge deck for Field Tests 1 and 2, ANSYS, and SAP2000 based on an empty truck: (a) - (d) show the strains on the transverse beam

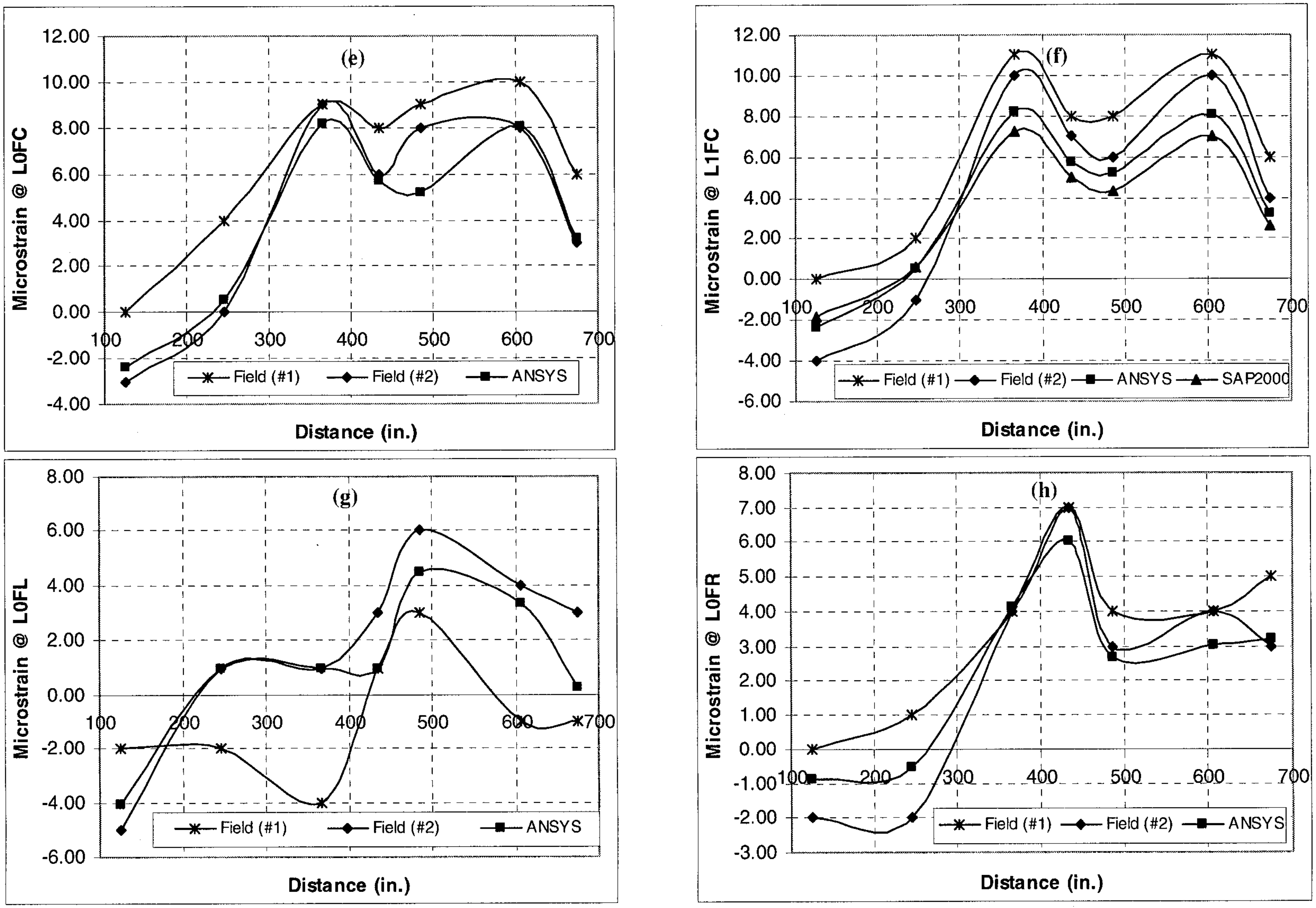

Figure 4.11 (continued): Comparison of strain versus distance of the single axle from the end of the bridge deck for Field Tests 1 and 2, ANSYS, and SAP2000 based on an empty truck: (e)-(h) show the strains on the longitudinal beam

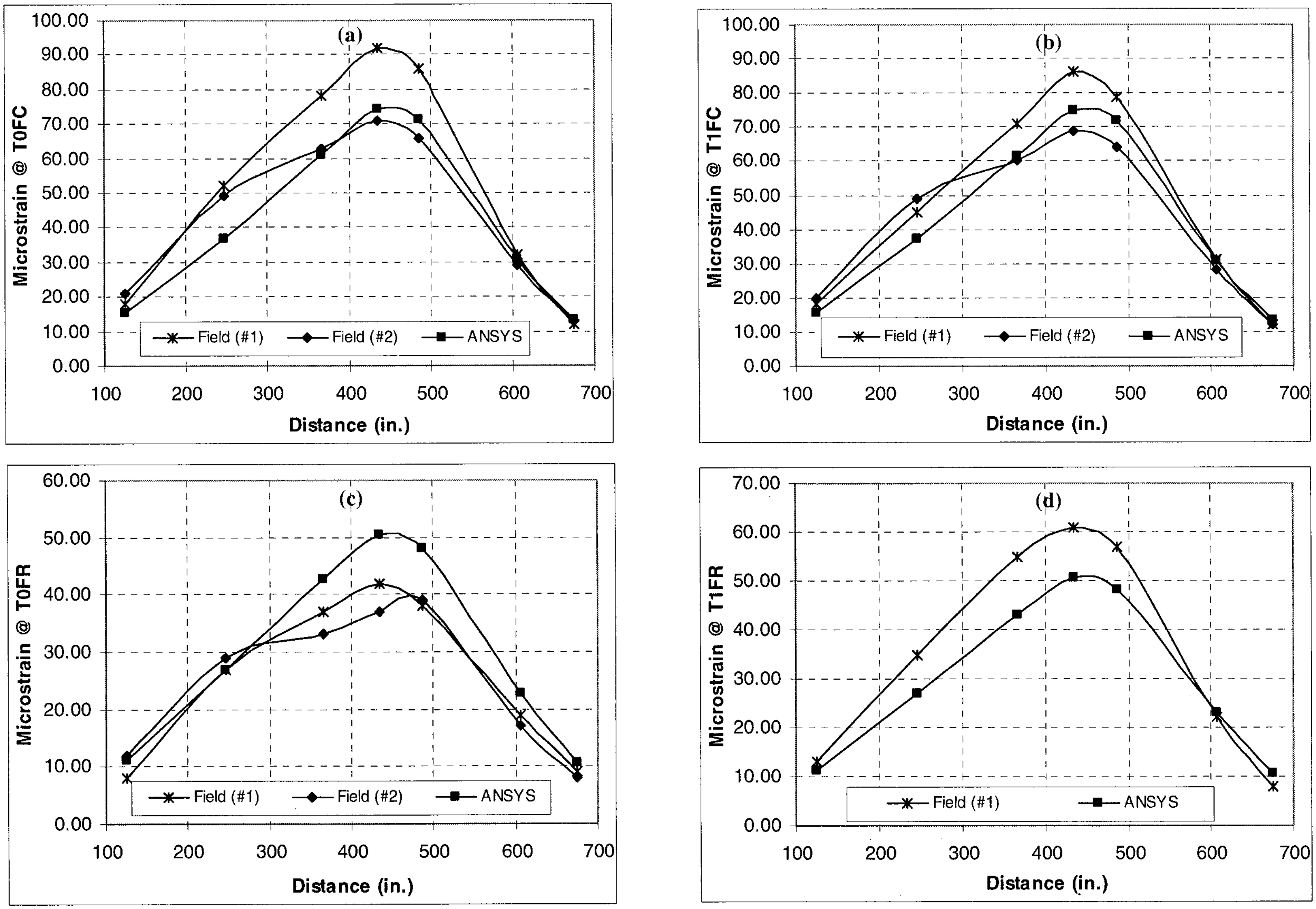

Figure 4.12: Comparison of strain versus distance of the single axle from the end of the bridge deck for Field Tests 1 and 2, ANSYS, and SAP2000 based on a full truck: (a) - (d) show the strains on the transverse beam

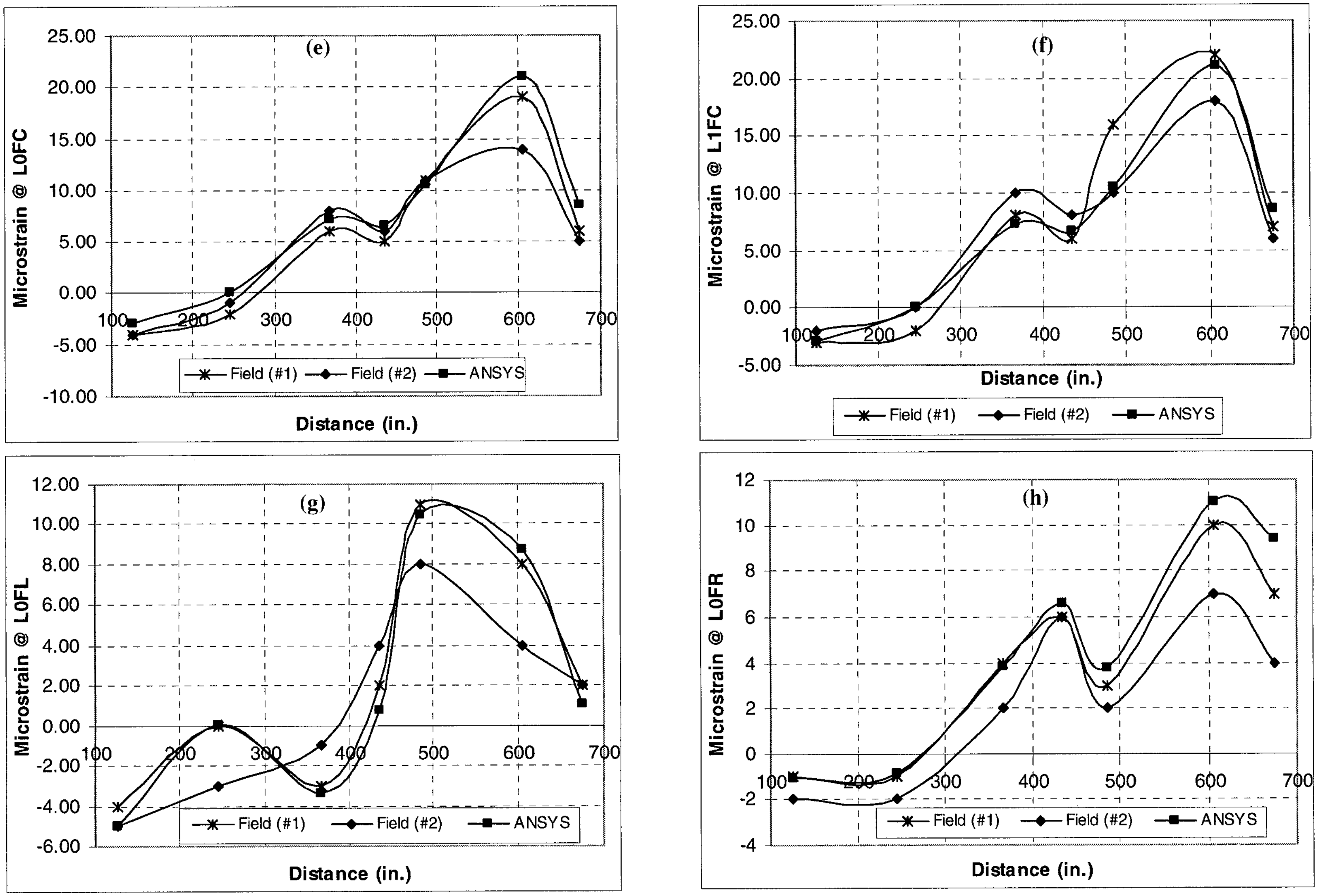

Figure 4.12 (continued): Comparison of strain versus distance of the single axle from the end of the bridge deck for Field Tests 1 and 2, ANSYS, and SAP2000 based on a full truck: (e)-(h) show the strains on the longitudinal beam

Figures 4.9 – 4.12 show that ANSYS in general provides reasonable predictions for both strains and the trends in the strains versus the various truck locations. For the comparisons of ANSYS and SAP2000 with the field data (Figures 4.11 (a) and (f)), both ANSYS and SAP2000 show similar trends to the field data; however, ANSYS predicts the behavior more accurately, as expected. The comparison between ANSYS results and field data are discussed below for the empty truck, full truck, and general conditions.

4.4.1 Analysis of responses to empty truck load

4.4.1.1 Discussion of responses on the transverse beam (Figures 4.11 (a)-(d))

Maximum strains for T0FC and T1FC from Field Test 1 and ANSYS are obtained when the single axle of the truck is at 11,000 mm (435 inches) from the end of the bridge deck (Position 4 from Figure 4.1 (d)). At this location the load from the tandem axle is right above the transverse beam that has the fiber optic sensors attached (Figures 4.1 (d) and 4.2). The same is also true for T0FR and T1FR.

4.4.1.2 Discussion of responses on the longitudinal beam (Figures 4.11 (e)-(h))

Maximum strains for L0FC and L1FC from Field Test 1 and ANSYS occur when the single axle of the truck is about 9700 mm (380 inches) and 15,000 mm (600 inches) from the end of the bridge deck (Positions 3 and 6 from Figures 4.1 (c) and (f), respectively). At Positions 3 and 6, the loads from the single and tandem axles have the greatest effect on the middle span of the instrumented longitudinal beam as one expects by inspecting Figures 4.1 and 4.2.

For the L0FL sensor (Figure 4.11 (g)), field and ANSYS results show that the maximum strain is reached when the truck is 12,300 mm (486 inches) from the end of the bridge (Position 5). At Position 5, the tandem axle is closest to the L0FL sensor. For the L0FR sensor, the maximum strain is achieved when the truck is 11,000 mm (435 inches) from the end (Position 4). At this position, the single axle is closest to the L0FR sensor. It might appear that if the truck is at Position 6, a large strain should also be achieved at L0FR. Although the tandem axle of the truck is closest to the L0FR sensor, however, the single axle has moved across the second transverse beam, which tends to deflect the longitudinal beam up. The effect of producing negative strain is observed at Position 1 in which all the measured strains in the longitudinal beam are negative.

4.4.2 Analysis of responses to full truck load

4.4.2.1 Discussion of responses on the transverse beam (Figures 4.12 (a)-(d))

As discussed above, the maximum strains on the transverse beam can be obtained when the truck is at 11,000 mm (435 inches) from the end of the bridge deck (Position 4). The trends are steeper, however, than those under an empty truck load. The proportion of the load distributed to the tandem axle relative to the load distributed to the single axle under a full truck load is much higher than that in the empty truck load case. In other words, the load from the tandem axle has more influence on the strain at that location than that from the single axle.

4.4.2.2 Discussion of responses on the longitudinal beam (Figures 4.12 (e)-(h))

The maximum strains for L0FC and L1FC are developed when the truck is at 15,400 mm (606 inches) from the end (Position 6). The load from the tandem axle most significantly affects the strain at this location. For L0FL, the maximum strain occurs when the truck is at 12,300 mm (486 inches) from the end of the bridge deck (Position 5), because the tandem axle is closest to the sensor. Large strains for L0FR are obtained when the truck is at 11,000 mm (435 inches) and 15,400 mm (606 inches) from the end (Positions 4 and 6), as the single and tandem axles are closest to the sensor. The maximum occurs for Position 6 because the load from the tandem axle is much higher than that from the single axle. Unlike the empty truck load condition, the effect from the single axle is not sufficient to cancel that from the tandem axle closer to the sensor.

4.4.3 Analysis of responses in general

Figures 4.9 – 4.12 show that ANSYS predicts reasonably well the values and the trends in strains versus truck locations. The two sets of field data were comparable, though the strains for the loaded truck were generally less in Field Test 2 due to the lower weight of the loaded truck in Field Test 2 (see Appendix B). Also, there was occasional anomalous behavior in Field Test 1 data compared to Field Test 2 and ANSYS results. The reason for the discrepancies was not investigated.

Based on the comparisons, the ANSYS bridge FE model is stiffer than the actual bridge, as expected. Generally, an FE model of a reinforced concrete structure predicts that the structure is stiffer than it actually is. One reason for this is because the materials in the FE model are perfectly homogenous, unlike those in the actual structure. Moreover, the boundary conditions strictly defined in the FE model are more rigid than the actual structure, and the discretization itself imposes additional constraints on the displacements. Additionally, micro-cracks in the concrete and bond slip between the concrete and reinforcing steel bars, as well as other imperfections in construction, may lessen the stiffness of the actual structure.

The FEM predictions could potentially be improved by using more accurate material properties for the concrete and providing more realistic boundary conditions. The 17 MPa (2500 psi) compressive strength of concrete used in the model complies with AASHTO bridge rating recommendations for all bridges built prior to 1959 (*McCurry 2000*). The actual compressive strength of the concrete and modulus of elasticity are most likely substantially higher than the values used in the FE model. The concrete material properties are unknown, however, unless the strength of the on-site concrete is tested using core samples. ODOT has not performed these tests on the historic structure. Pulse-velocity tests have recently been conducted by OSU to provide estimates of the material properties of the in-situ concrete. Preliminary findings indicate that the actual concrete is stiffer by approximately 30%.

A more flexible and realistic structure can be obtained if the boundary conditions are modeled by properly considering the soil-structure interface. As discussed earlier, the FE bridge model used in this study is assumed to be rigidly restrained at the spread footing foundations and the walls at both ends of the bridge. That is, all degrees of freedom at each boundary node at the foundations (at the bottoms of the columns and at the corners of the bridge where the end transverse beams meet the longitudinal beams) are fully restrained. Vertical translation is restrained along the bottom of the transverse beams where the walls are located. The boundary conditions can be improved by introducing a boundary or spring element to represent the stiffness of the soil at the supports of the bridge. With these more realistic boundary conditions, some translation and rotation at the foundations would occur, as in the actual bridge.

4.5 ANALYSIS OF THE UNSTRENGTHENED HORSETAIL CREEK BRIDGE

Although strain data for the Horsetail Creek Bridge before the FRP strengthening were not available, it was interesting to examine the response of the bridge before the retrofit using the ANSYS model. An unstrengthened bridge model was developed using the same methodology as for the strengthened bridge. The FE bridge model with steel reinforcement details prior to the retrofit is shown in Figure 4.5. Only the full truck load was applied to the model for each location shown in Figure 4.1. Comparison of the strains from the FE bridge models with and without the FRP strengthening was made for T0FC, T0FR, L0FL, L0FC, and L0FR in Tables 4.4 and 4.5.

Table 4.4: Comparison of strains on the transverse beam between FE bridge models with and without FRP strengthening

Truck Locations (Distances from the end)	Strain (Microstrain)					
	T0FC			T0FR		
	W/ FRP	W/O FRP	Diff. (%)	W/ FRP	W/O FRP	Diff. (%)
1 (126")	15.35	15.96	-3.947	11.05	11.50	-4.014
2 (246")	36.90	38.32	-3.829	26.96	28.06	-4.083
3 (366")	61.01	63.48	-4.059	42.77	44.52	-4.101
4 (435")	74.43	77.45	-4.057	50.39	52.41	-4.012
5 (486")	71.42	74.36	-4.111	48.13	50.15	-4.184
6 (606")	30.71	32.10	-4.533	22.87	23.95	-4.734
7 (675")	13.15	13.87	-5.524	10.53	11.15	-5.850

Table 4.5: Comparison of strains on the longitudinal beam between FE bridge models with and without FRP strengthening

Truck Locations (Distances from the end)	Strain (Microstrain)								
	L0FL			L0FC			L0FR		
	W/ FRP	W/O FRP	Diff. (%)	W/ FRP	W/O FRP	Diff. (%)	W/ FRP	W/O FRP	Diff. (%)
1 (126")	-4.986	-4.999	-0.260	-2.885	-2.881	0.138	-1.093	-1.092	0.071
2 (246")	0.046	0.057	-22.01	0.005	0.026	-377.7	-0.860	-0.854	0.778
3 (366")	-3.360	-3.350	0.290	7.213	7.290	-1.059	3.857	3.893	-0.918
4 (435")	0.786	0.813	-3.488	6.589	6.656	-1.021	6.553	6.601	-0.727
5 (486")	10.47	10.54	-0.588	10.51	10.59	-0.747	3.788	3.845	-1.498
6 (606")	8.685	8.740	-0.629	21.07	21.19	-0.566	11.02	11.08	-0.592
7 (675")	1.043	1.068	-2.339	8.577	8.641	-0.746	9.390	9.445	-0.590

Differences in structural performance before and after retrofitting were not dramatic because the bridge did not crack under the applied truck load. The bridge operated within its linear range, and the effect of the retrofit was minimal in the linear region. Similar findings were shown in Chapter 3 for the individual beams. However, after cracking, the individual beams strengthened with the FRP laminates showed noticeable improvements in structural performance by delaying the propagation of cracks and reducing the deflection of the beams. Thus, more significant improvements in overall bridge performance due to the FRP would be expected when the non-linear, post-cracking behavior is examined in a planned future study.

5.0 CONCLUSIONS AND RECOMMENDATIONS

5.1 SUMMARY AND CONCLUSIONS

5.1.1 Conclusions for finite element models of the full-scale beams

1. The general behavior of the finite element models represented by the load-deflection plots at midspan show good agreement with the test data from the full-scale beam tests. However, the finite element models show slightly more stiffness than the test data in both the linear and nonlinear ranges. The effects of bond slip (between the concrete and steel reinforcing) and microcracks occurring in the actual beams were excluded in the finite element models, contributing to the higher stiffness of the finite element models.

2. The load-strain plots for selected locations from the finite element analysis show fair agreement with the test data. For the load-tensile strain plots for the main steel reinforcing at midspan, the strains from the finite element analysis and the experimental data correlate well in the linear range, and the trends in the nonlinear range are generally comparable. The load-compressive strain plots (at midspan at the center of the top face) from the full-size beams have good agreement with those from the finite element analysis, especially for the Control Beam.

3. The final loads from the finite element analyses are lower than the ultimate loads from the experimental results by 5% - 24%. This is probably due in part to neglecting the inclined portions of the steel reinforcement; ignoring the effects of concrete toughening mechanisms; and using assumed materials properties values instead of measured values.

4. The load carrying capacity of the Flexure/Shear strengthened beam predicted by the finite element analysis is higher than that of the Control Beam by 105%, which agrees very well with hand calculations showing that the FRP-strengthened beam has a higher ultimate load than the Control Beam by 104%.

5. The crack patterns at the final loads from the finite element models correspond well with the observed failure modes of the experimental beams, and the crack pattern predicted by the finite element analysis for the Flexural strengthened beam agrees with hand calculations showing that the beam fails in flexure.

5.1.2 Conclusions for finite element models of the Horsetail Creek Bridge

For the Horsetail Creek Bridge after the FRP retrofit, the model structure is uncracked for both the empty and full trucks. ANSYS reasonably predicts both strains and trends in the strains versus the truck locations. For the two truck loads, the response of the bridge on the monitored transverse and longitudinal beams can be summarized as follows:

1. The maximum strains at the center bottom (on concrete and on FRP laminates) of the transverse beam at midspan are produced when the load from the tandem axle (which is larger than that from the single axle) is directly above the beam.

2. The maximum strains at the center bottom (on concrete and on FRP laminates) of the longitudinal beam at midspan are obtained when the load from the tandem axle of the truck is at midspan of the beam. A large strain also occurs under an empty truck when the load from the single axle, which weighs approximately the same as the tandem axle, is at midspan of the beam.

3. As the analysis of the ANSYS bridge model is essentially linear for the uncracked structure, responses from a preliminary linear elastic model using SAP2000 were used to compare with those from ANSYS. It was shown that the trends in the strain results for the various locations of the truck obtained from the ANSYS and SAP2000 models were similar. However, ANSYS predicts the experimental behavior more accurately.

Although there are no field data available for the bridge's response prior to the FRP strengthening, an FEM model of the unstrengthened bridge was also developed to compare structural behavior with that of the FRP-strengthened bridge. Analyses were performed for the loaded truck as it moved across the bridge. The results were as follows:

1. As in the analysis of the bridge after the retrofit, the behavior prior to retrofit is essentially linear because the bridge model does not crack under the truck load.

2. The comparisons between both bridge models show that the differences in structural responses before and after the retrofit are not significant. The bridge is only slightly stiffer from the FRP. Similar results were also found in the study of the full-scale beams when the beams were still uncracked.

5.2 RECOMMENDATIONS

5.2.1 Recommended FE modeling and analysis procedure

Nonlinear analysis after cracking is essential to model beams up to their failure. Nonlinear reinforced concrete FE models, either with or without FRP laminates, however, are susceptible to numerical instability. For the development of the FE bridge model, the structural details of the actual bridge are quite complex. Simplification is possible, and the most important details can be modeled, producing sufficiently accurate predictions with less CPU time and disk-space consumed. Recommendations for both linear and nonlinear analyses of reinforced concrete models are as follows:

1. Simplification should be made in modeling both full-scale beams and bridges to reduce modeling difficulties and computing resources. Reinforcing steel bars can be "lumped" in locations associated with the FE mesh for the model. In addition, a consistent overall thickness of FRP composites can be used to avoid discontinuities.

2. At the beginning of FE model development, a reasonable mesh and a convergence study are needed to obtain a reliable model. Convergence of the solution is achieved when an adequate number of elements is used in a model. For reinforced concrete models in a nonlinear analysis, however, too fine of a mesh may cause numerical instability. On the other hand, if the mesh is too coarse, the analysis will not be sufficiently accurate. Generally, when an actual crack or groups of cracks occur in concrete, the width of the crack band is many times larger than the maximum aggregate size (*Shah, et al. 1995*). As a result, the concrete element size should be two to three times greater than the maximum aggregate size to correctly and realistically model the actual cracks using the smeared cracking approach (*Barzegar, et al. 1997; Isenberg 1993; Shah, et al. 1995*). In this study, the maximum nominal aggregate size used in the experimental beams was 30 mm (1 in), and the minimum FE element size for the full-scale beams was 50.8 mm x 50.8 mm x 44.45 mm (2 in x 2 in x 1.75 in) and 33.02 mm x 33.02 mm x 63.5 mm (1.3 in x 1.3 in x 2.5 in) for the Horsetail Creek Bridge.

3. Tolerances in convergence criteria should carefully be defined in a nonlinear analysis. With load adjustment, tolerances for both force and displacement criteria may need to be relaxed to avoid a diverged solution. After the load range that produces a diverged solution is revealed from a previous ANSYS trial run, either tolerance or load adjustments or both have to be made to prevail over the divergence problem at that loading level.

4. In a nonlinear reinforced concrete analysis, the shear transfer coefficient must be assumed. For closed cracks, the coefficient is assumed to be 1.0, while for open cracks it should be in the suggested range of 0.05 to 0.5, rather than 0.0, to prevent numerical difficulties (*Barzegar, et al. 1997; Huyse, et al. 1994; Isenberg 1993; Najjar, et al. 1997*). In this report, a value of 0.2 was used, which resulted in accurate predictions. Values less than 0.2 were tried, but they caused divergence problems at very low loading levels.

5.2.2 Recommended FE modeling procedure for reinforced concrete beams

1. The symmetry of the beams should be used to reduce computational time and computer disk space requirements. In this project, a quarter of the full-size beam, with proper boundary conditions, was used for modeling.

2. A steel plate needs to be included in the models at the support locations to represent the actual support condition in the full-size beams. The steel plate also provides a more even stress distribution over the support area to avoid problems of stress concentration.

3. For nonlinear analysis of a reinforced concrete beam, the total load applied to a model must be divided into a number of load steps. Sufficiently small load step sizes are required, particularly at changes in behavior of the reinforced concrete beam, i.e., major cracking of concrete, yielding of steel, and approaching failure of the reinforced concrete beam. Properly defining minimum and maximum sizes for each load step, depending upon the behavior of the reinforced concrete beam, assists in convergence of the solutions and reduces computer computational time.

5.2.3 Recommended FE modeling procedure for the reinforced concrete bridge

1. Symmetry should be used in bridge modeling. In this project, only a longitudinal half of the bridge was modeled.

2. For simplification of load configurations, the load from each set of tires for both single and tandem axles can be lumped to the center of each set. Furthermore, the lumped load at locations where it does not coincide with a node in the FEM mesh needs to be linearly distributed to the nearest nodes in order to analyze a variety of truck locations on the bridge deck.

3. Model accuracy can be improved by using realistic materials property values and by properly defining boundary conditions. For the Horsetail Creek Bridge, the actual compressive strength of the concrete and modulus of elasticity were most likely substantially higher than the assumed values used in the FE model. For the boundary conditions, the soil-structure interface should be considered to better represent the actual behavior of the structure. This may be done by using boundary springs and assigning them reasonable stiffness values from properties of the on-site soil.

4. In order to assess the ultimate capacity of the FRP-strengthened Horsetail Creek Bridge, a nonlinear analysis to failure needs to be performed.

6.0 REFERENCES

ACI 318-99, American Concrete Institute, "Building Code Requirements for Reinforced Concrete," American Concrete Institute, Farmington Hills, Michigan, 1999.

ACI 440, American Concrete Institute, "Guide for the Design and Construction of Externally Bonded FRP Systems for Strengthening Concrete Structures," American Concrete Institute, Farmington Hills, Michigan, 2000.

Adams, V. and A. Askenazi, *Building Better Products with Finite Element Analysis*, OnWord Press, Santa Fe, New Mexico, 1998.

American Society for Testing and Materials (ASTM) Subcommittee C09.64, *Standard Test Method for Pulse Velocity Through Concrete,* Designation C 597-83, ASTM, West Conshohocken, Pennsylvania, 1983.

American Society for Testing and Materials (ASTM) Subcommittee C09.70, *Standard Test Method for Static Modulus of Elasticity and Poisson's Ratio of Concrete in Compression*, Designation C 469-94, ASTM, West Conshohocken, Pennsylvania, 1994.

ANSYS, *ANSYS User's Manual Revision 5.5*, ANSYS, Inc., Canonsburg, Pennsylvania, 1998.

Arduini, M., A. Di Tommaso and A. Nanni, "Brittle Failure in FRP Plate and Sheet Bonded Beams," *ACI Structural Journal*, 94(4), pp. 363-370, 1997.

Bangash, M. Y. H., *Concrete and Concrete Structures: Numerical Modeling and Applications*, Elsevier Science Publishers Ltd., London, England, 1989.

Barzegar, Maddipudi, and Srinivas, "Three-Dimensional Modeling of Concrete Structures. I: Plain Concrete." *Journal of Structural Engineering*, 123(10), 1339-1346, 1997.

Bathe, K. J., *Finite Element Procedures*, Prentice-Hall, Inc., Upper Saddle River, New Jersey, 1996.

Chansawat, K., "Nonlinear Finite Element Analysis of Reinforced Concrete Structure Strengthened With FRP Laminates," personal communications, Corvallis, Oregon, 2000.

Chen, A. C. T. and W. F. Chen, "Constitutive Relations for Concrete," *Journal of the Engineering Mechanics Division*, ASCE, Vol. 101, No. EM4, pp. 465-481, August 1975.

CH2M HILL, Inc., Consulting Engineers-in conjunction with TAMS Consultants, "Evaluation and Resolution of Under Capacity State Bridges: Bridge #04543, Horsetail Creek Bridge, Corvallis, Oregon, June 1997.

Desayi, P. and S. Krishnan, "Equation for the Stress-Strain Curve of Concrete," *Journal of the American Concrete Institute*, 61, pp. 345-350, March 1964.

Fyfe Corporation, Material Data Properties. (1998) *Tyfo Systems for Beams and Slabs*, Fyfe Corporation LLC, San Diego, CA, 1998.

Gere, J. M. and S. P. Timoshenko, *Mechanics of Materials*, PWS Publishing Company, Boston, Massachusetts, 1997.

Gibson, R. F., *Principles of Composite Material Mechanics*, McGraw-Hill, Inc., New York, New York, 1994.

Hemmaty, Y., "Modeling of the Shear Force Transferred Between Cracks in Reinforced and Fibre Reinforced Concrete Structures," *Proceedings of the ANSYS Conference, Vol. 1*, Pittsburgh, Pennsylvania, August 1998.

Hemmaty, Y., G. DeRoeck and L. Vandewalle, "Parametric Study of RC Corner Joints Subjected to Positive Bending Moment by Nonlinear FE Model," *Proceedings of the ANSYS Conference, Vol. 2*, Pittsburgh, Pennsylvania, June 1992.

Huyse, L., Y. Hemmaty and L. Vandewalle, "Finite Element Modeling of Fiber Reinforced Concrete Beams," *Proceedings of the ANSYS Conference, Vol. 2*, Pittsburgh, Pennsylvania, May 1994.

Hyer, M.W., *Stress Analysis of Fiber-Reinforced Composite Materials*, WCB/McGraw-Hill, Inc., Boston, Massachusetts, 1998.

Isenberg, J., *Finite Element Analysis of Reinforced Concrete Structures II*. ASCE, New York, NY, 1993.

Kachlakev, D.I., "Finite Element Method (FEM) Modeling for Composite Strengthening/Retrofit of Bridges." Research Project Work Plan, Civil, Construction and Environmental Engineering Department, Oregon State University, Corvallis, Oregon, 1998.

Kachlakev, D.I., *Strengthening Bridges Using Composite Materials*. FHWA-OR-RD-98-08, Oregon Department of Transportation, Salem, Oregon, 1998.

Kachlakev, D.I., "Retrofit of Historic Structures Using FRP Composites." ICCE/6 Sixth Annual International Conference on Composites Engineering, Orlando, FL, 387-388, 1999.

Kachlakev, D.I. and D. McCurry, Jr., *Simulated Full Scale Testing of Reinforced Concrete Beams Strengthened with FRP Composites: Experimental Results and Design Model Verification*, Oregon Department of Transportation, Salem, Oregon, June 2000.

Kant, T., *Finite Elements in Computational Mechanics*, Pergamon Press, Inc., Elmsford, NY., 1985.

Kaw, A. K., *Mechanics of Composite Materials*, CRC Press LLC, Boca Raton, Florida, 1997.

Lin, C. and A. C. Scordelis, "Nonlinear Analysis of RC Shells of General Form," *Journal of the Structural Division*, ASCE, 101(ST3), pp. 523-538, March 1975.

Logan, D. L., *A First Course in the Finite Element Method*, PWS Publishing Company, Boston, Massachusetts, 1992.

Marshall, O. S. and J. P. Busel, "Composite Repair/Upgrade of Concrete Structures," 4th Materials Conference, "Materials for the New Millennium", editor K. Chong, American Society of Civil Engineers, Washington, D. C., November 1996.

McCurry, D., Jr. and D. L. Kachlakev, "Strengthening of Full Sized Reinforced Concrete Beam Using FRP Laminates and Monitoring with Fiber Optic Strain Gauges," in *Innovative Systems for Seismic Repair and Rehabilitation of Structures, Design and Applications*, Technomic Publishing Co., Inc., Philadelphia, Pennsylvania, March 2000.

Mindess, S. and J. F. Young, *Concrete*, Prentice-Hall, Inc., Englewood Cliffs, New Jersey, 1981.

Najjar, S., K. Pilakoutas and P. Waldran, "Finite Element Analysis of GFRP Reinforced Concrete Beams." *Proceedings of the Third International Symposium*, Sapporo, Japan, 2, 519-526, 1997.

Oregon Department of Transportation (ODOT) Field Test Data, Private Correspondence, Salem, Oregon, 2000.

Oregon Department of Transportation (ODOT) Field Test Data, Private Correspondence, Salem, Oregon, 2001.

Oregon State University Internal Research "Three Dimensional Finite Element Analysis of Fiber-Reinforced Polymer-Strengthened Reinforced Concrete Bridge," Oregon State University, Corvallis, Oregon, 2000.

Potisuk, T., "Finite Element Modeling of Reinforced Concrete Beams Externally Strengthened by FRP Composites." Masters Thesis, Oregon State University, Corvallis, Oregon, 2000.

Neville, A. M., *Properties of Concrete*, John Wiley & Sons, Inc., New York, New York, 1996.

Ngo, D. and A. C. Scordelis, "Finite Element Analysis of Reinforced Concrete Beams," *Journal of the American Concrete Institute*, 64(3), pp. 152-163, 1967.

Nilson, A. H., "Nonlinear Analysis of Reinforced Concrete by the Finite Element Method," *Journal of the American Concrete Institute*, 65(9), pp. 757-766, 1968.

Nilson, A. H., *Design of Concrete Structures*, McGraw-Hill, Inc., New York, New York, 1997.

Patnaik, A. K., "Horizontal Shear Strength of Composite Concrete Beams With a Rough Interface," Ph.D. Dissertation, Department of Civil Engineering, University of Calgary, Calgary, Alberta, Canada, December 1992.

Rashid, Y. R., "Ultimate Strength Analysis of Prestressed Concrete Pressure Vessels," *Nuclear Engineering and Design*, 7(4), pp. 334-344, Amsterdam, Netherlands, April 1968.

Seible, F., G. Hegemier and V. Karbhari, "Advanced Composite for Bridge Infrastructure Renewal," *4th International Bridge Engineering Conference, Proceedings, Vol. 1*, San Francisco, California, August 29-30 1995.

Shah, S. P., S. E. Swartz and C. Ouyang, *Fracture Mechanics of Concrete*, John Wiley & Sons, Inc., New York, New York, 1995.

Spiegel, L., and G. F. Limbrunner, *Reinforced Concrete Design.* 4th ed. Prentice-Hall, Inc., Upper Saddle River, NJ, 1998

Steiner, W., "Strengthening of Structures with CFRP Strips," *Advanced Composite Materials for Bridges and Structures, 2nd International Conference, Proceedings*, editor M. El-Bardry, Montreal, Canada, August 1996.

Suidan, M. and W. C. Schnobrich, "Finite Element Analysis of Reinforced Concrete," *Journal of the Structural Division*, ASCE, ST10, pp. 2109-2122, October 1973.

Tedesco, J. W., J. M. Stallings and M. El-Mihilmy, "Finite Element Method Analysis of a Concrete Bridge Repaired with Fiber Reinforced Plastic Laminates," *Computers and Structures*, 72, 379-407, 1999.

Tedesco, J. W., J. M. Stallings, M. El-Mihilmy and M. McCauley, "Rehabilitation of Concrete Bridges Using FRP Laminates," 4th Materials Conference, "Materials for the New Millennium", editor K. Chong, American Society of Civil Engineers, Washington, D. C., November 1996.

Transportation Research Board. High Value State ODOT Research, "Keeping Oregon's Bridges Strong and Handsome," (http://www4.nationalacademies.org/trb/scor/states.nsf/all/oregon) 1999.

Ugural, A. C. and S. K. Fenster, *Advanced Strength and Applied Elasticity*, Prentice-Hall Inc., Upper Saddle River, New Jersey, 1995.

Vecchio, F. J. and F. Bucci, "Analysis of Repaired Reinforced Concrete Structures," *Journal of the Structural Division*, ASCE, 125(6), 644-652, June 1999.

William, K. J. and E. P. Warnke, "Constitutive Model for the Triaxial Behavior of Concrete," *Proceedings, International Association for Bridge and Structural Engineering*, Vol. 19, ISMES, Bergamo, Italy, pp. 174, 1975.

APPENDICES

APPENDIX A:

STRUCTURAL DETAILS OF THE HORSETAIL CREEK BRIDGE

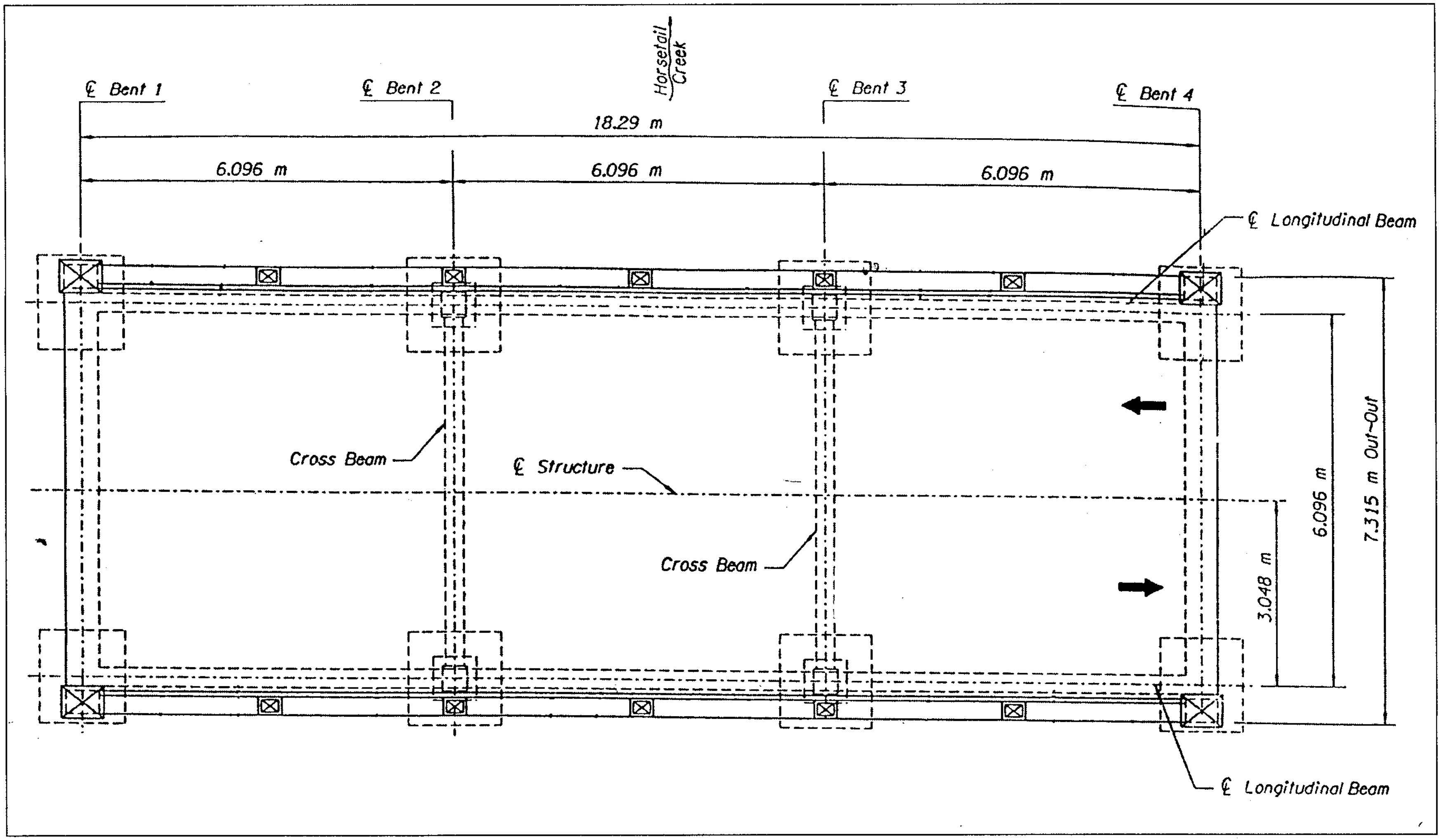

Bridge Plan (Not to Scale)

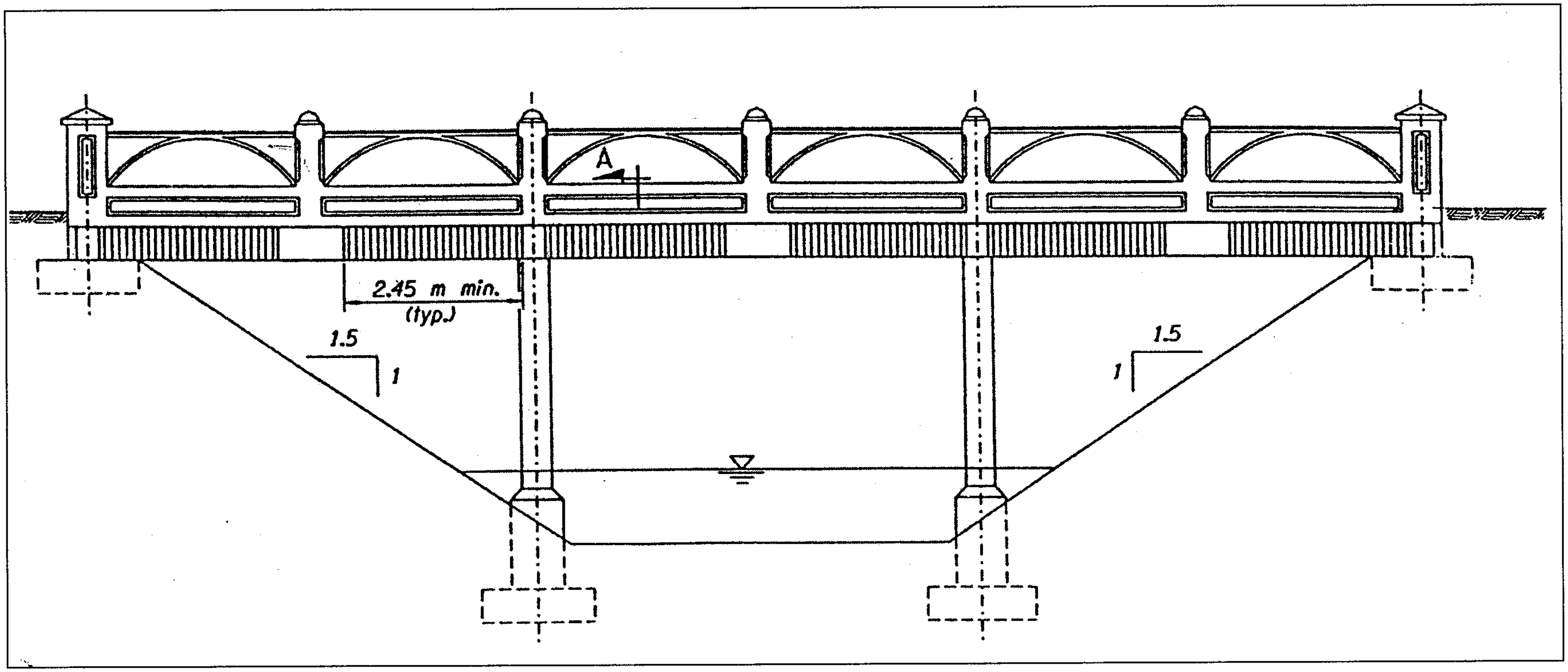

Bridge Elevation (Not to scale)

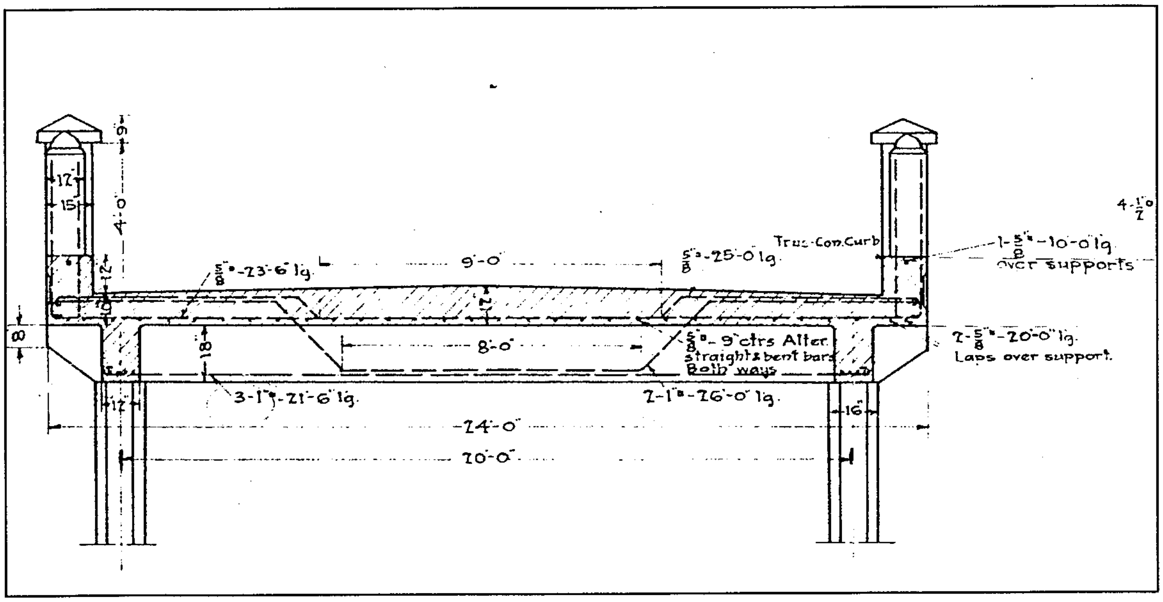

Steel Reinforcement Detail in Transverse Beam

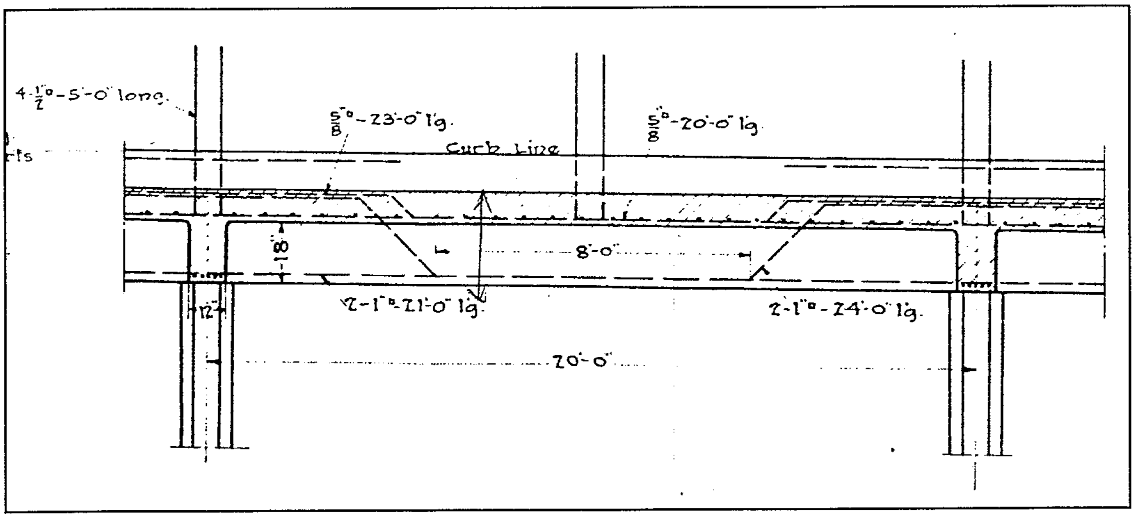

Steel Reinforcement Detail in Longitudinal Beam

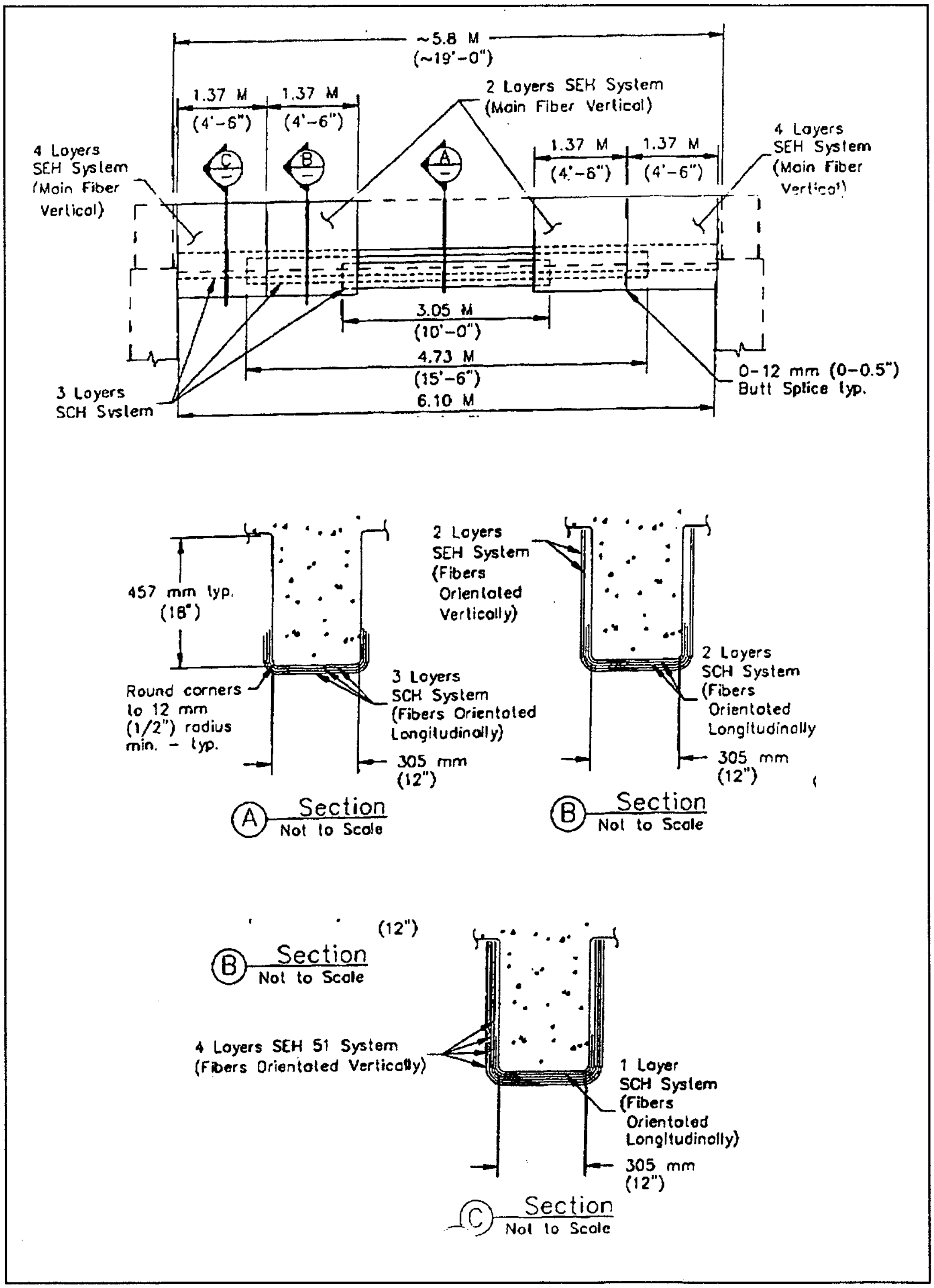

FRP Reinforcement Detail on Transverse Beam

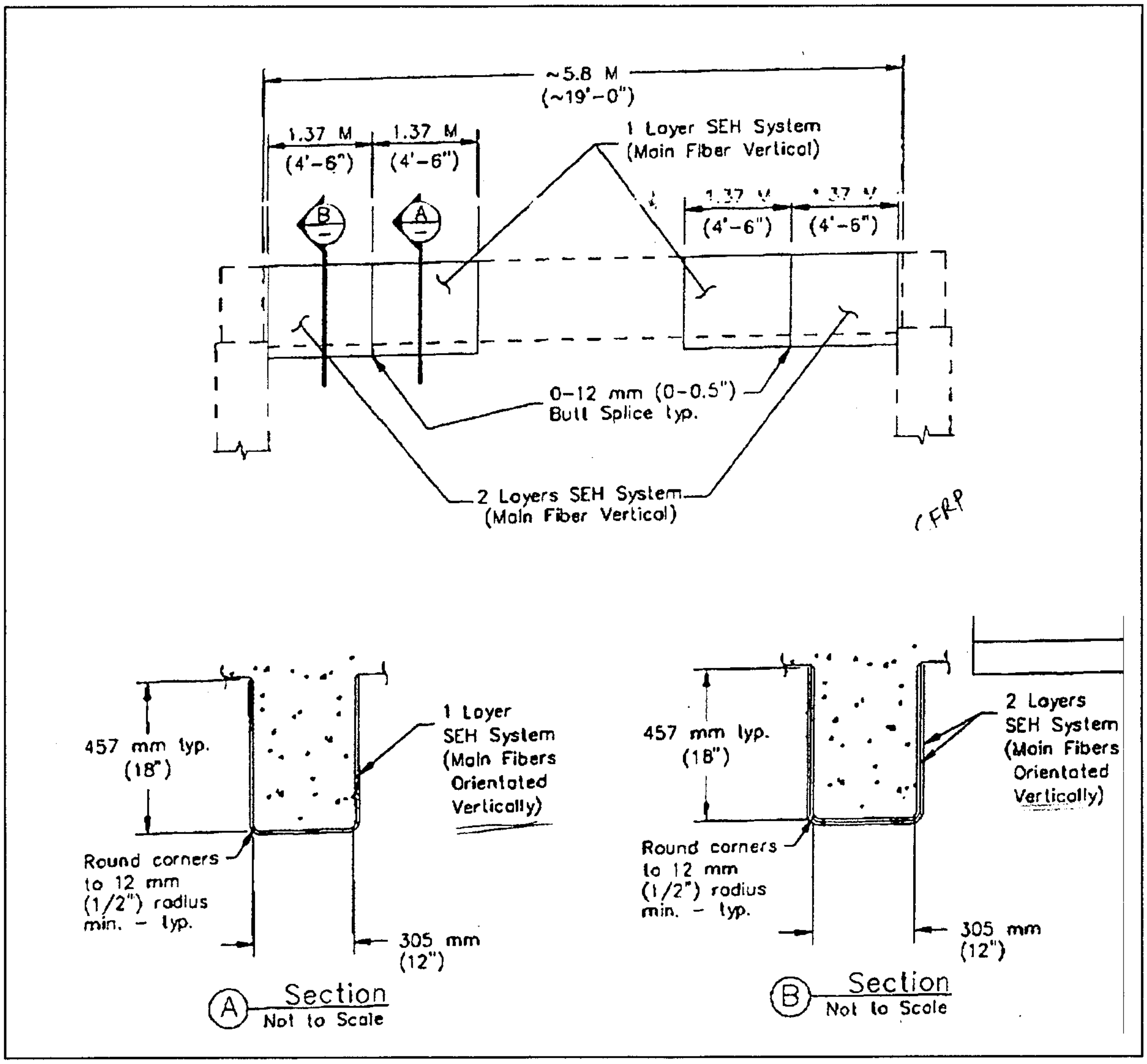

FRP Reinforcement Detail on Longitudinal Beam

APPENDIX B:

CONFIGURATION OF DUMP TRUCKS FOR STATIC TESTS ON HORSETAIL CREEK BRIDGE

Truck Information

Field Test 1 (License #: 187485)
Dimensions:

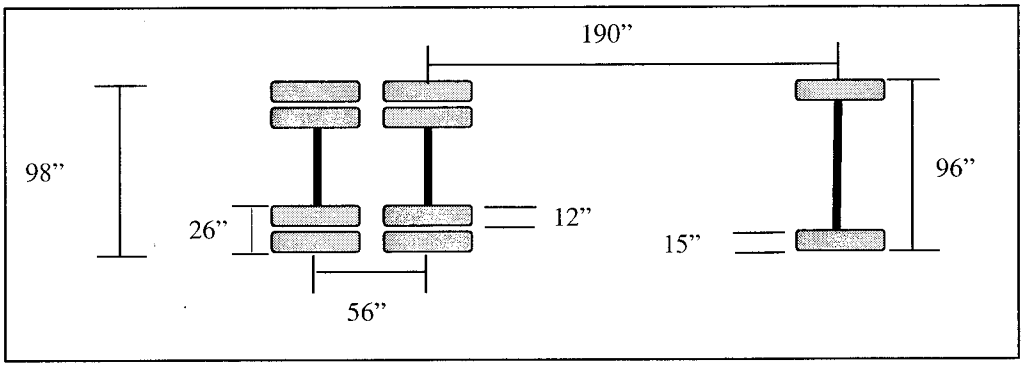

Axle Weights

Position	Empty (lbs.)	Full (lbs)
Front	12800	15600
Center	7500	16900
Back	7000	16600
Center + Back	14500	33500

Field Test 2 (License #: E172688)
Dimensions:

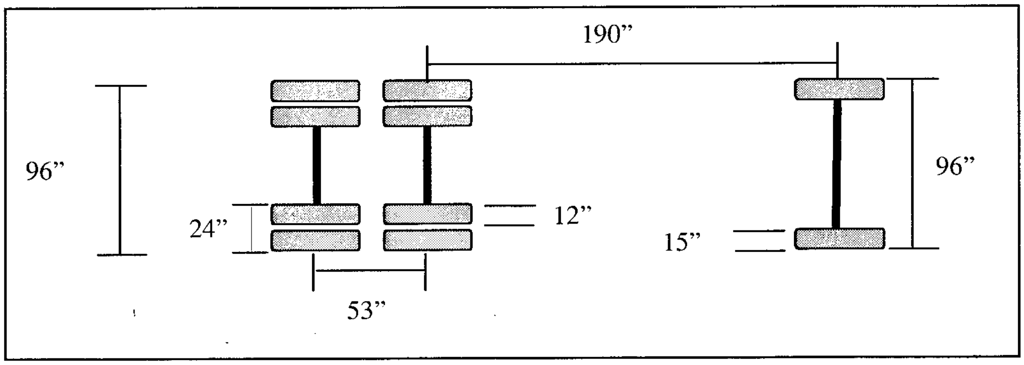

Axle Weights

Position	Empty (lbs.)	Full (lbs)
Front	16200	17700
Center	7300	13000
Back	7100	12600
Center + Back	14400	25600

Tire Contact (empty, **full**)

Nominal tire pressure: Back = 110-120 psi; Front = 120 psi

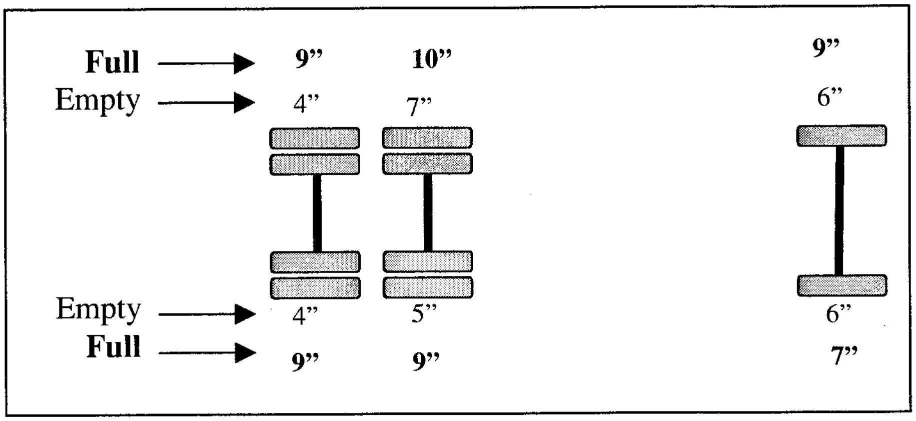

APPENDIX C:

LOCATIONS OF FIBER OPTIC SENSORS ON THE HORSETAIL CREEK BRIDGE

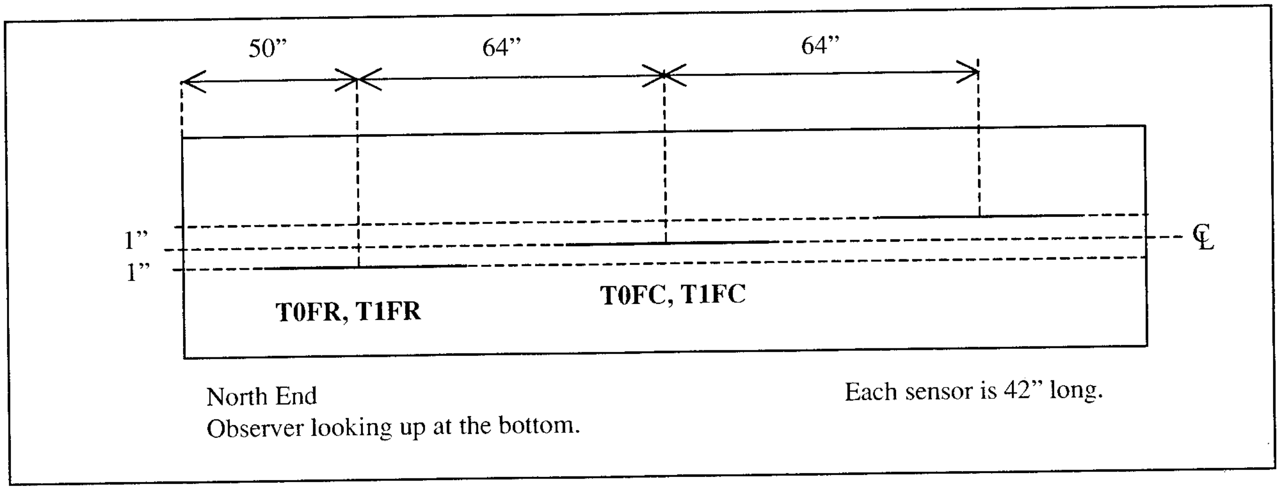

North End
Observer looking up at the bottom.

Each sensor is 42” long.

Bottom of the Transverse Beam

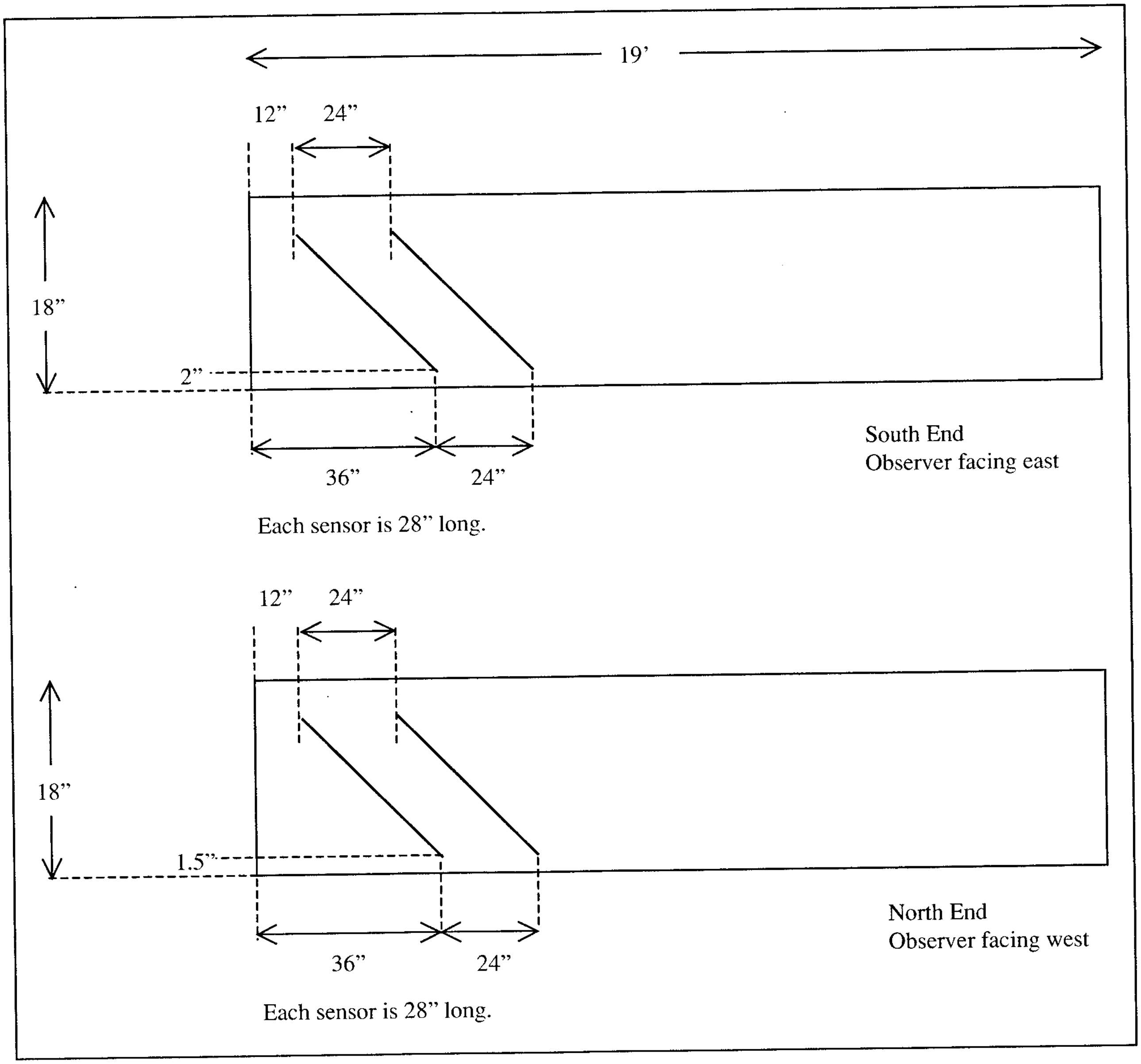

South End
Observer facing east

Each sensor is 28” long.

North End
Observer facing west

Each sensor is 28” long.

Sides of the Transverse Beam

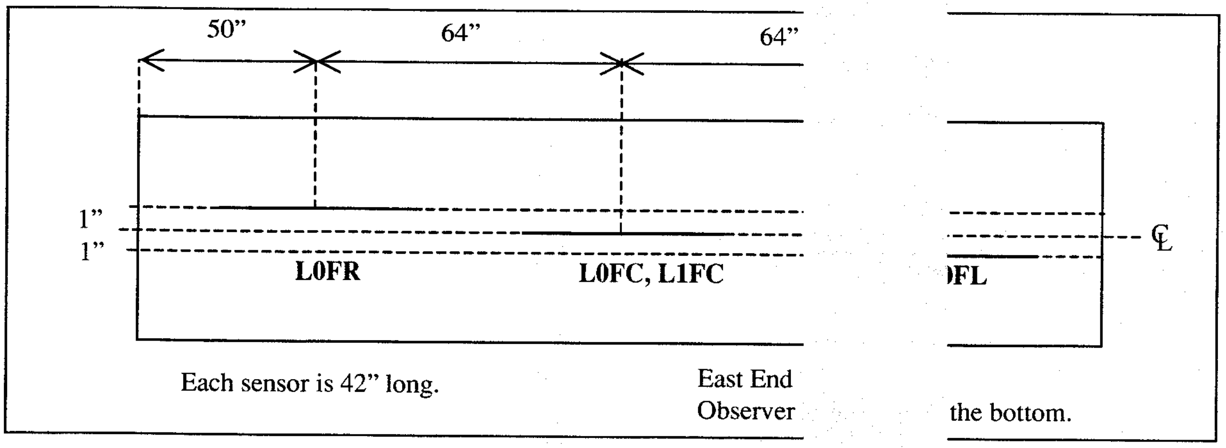

Bottom of the Longitudinal Be

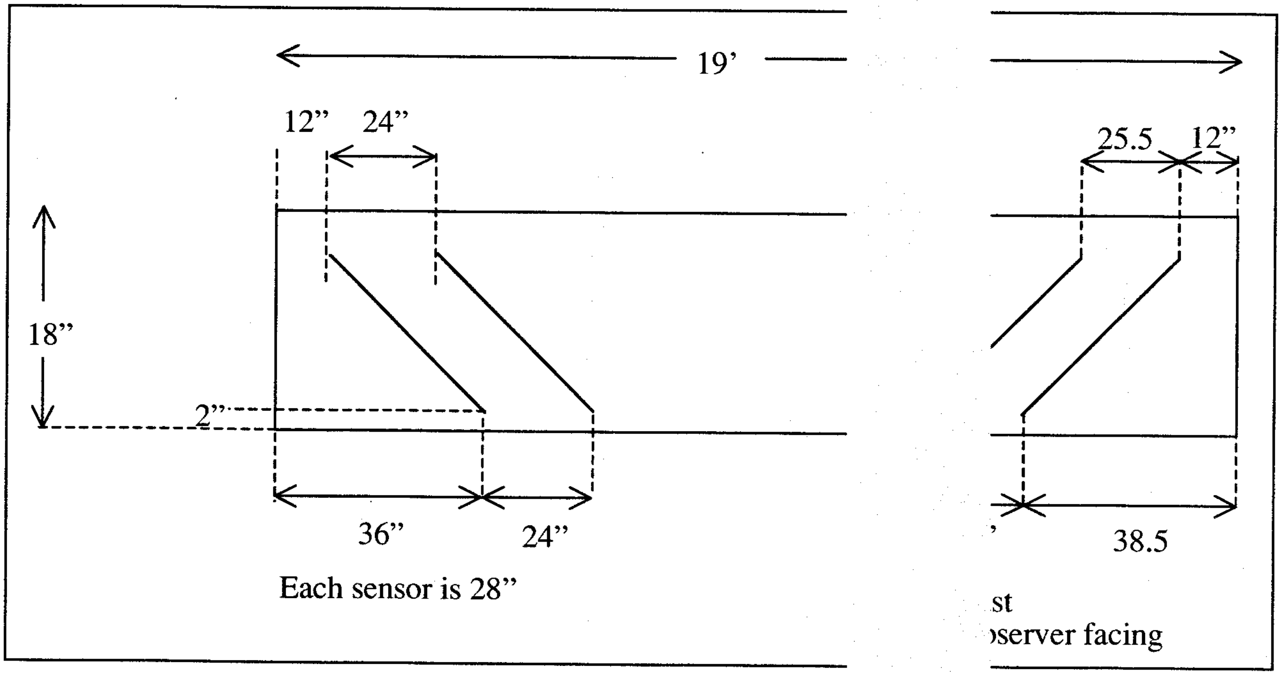

Side of the Longitudinal Bean